


Università degli Studi di Padova
Universidad Carlos III de Madrid
Técnico Lisboa

Three Dimensional Physics in Reversed Field Pinch and Stellarator

Promoters:
Prof. Dr. Paolo Bettini
Prof. Dr. Raul Sanchez

Supervisors:
Dr. David Terranova
Dr. Daniel López-Bruna

Doctoral Student: Yangyang Zhang

JOINT EUROPEAN RESEARCH DOCTORATE IN FUSION SCIENCE AND ENGINEERING
Cycle XXIX

Summary

Fusion research is motivated by the dilemma between the dramatic increase of energy demands and the limitation of total energy storage on earth. Thermal nuclear fusion has been developed addressing to this issue, along with many other ways of exploring new energy source and it is considered to be one of the most promising new energy sources for sustainable development of human civilization. Toroidal magnetic configurations are the main magnetic fusion research field. There are mainly three different types of toroidal magnetic configurations:

- The first type is tokamaks. Tokamaks are considered to be the most advanced toroidal configurations with most of the magnetic field being in the toroidal direction. The toroidal field is generated by external coils and the poloidal field is generated by both the plasma current induced externally and the bootstrap current generated by plasmas. The safety factor q in tokamaks is typically above 2.

- The second type is stellarators. Stellarators feature complex coil design because the helical magnetic field is generated by external coils only. This makes it free of plasma current so that stellarators are free of current driven instabilities, which makes one of the biggest advantages for stellarators. However, stellarators suffer some drawbacks like low β value and complex design and manufacturing of field coils. The q profile is usually below 1.

- The third type is reversed field pinches (RFPs). It has similar design with tokamaks. The magnetic field, however, is dominated by the poloidal component in the plasma edge. In fact, part of the toroidal field is generated via the so-called dynamo mechanism. Consequently, it could couple higher plasma current than tokamaks. The q profile is below 1 and becomes negative in the plasma edge.

One of the main challenges for toroidal magnetic configurations is to maintain high plasma confinement properties. Particles and energy are constrained on the flux surfaces with losses via radial transport process across the nested flux surfaces. Transport study has been intensively carried on tokamaks on one dimension with the assumption of toroidal symmetry. Indeed, the design of tokamaks is to achieve toroidal symmetry. However, in real experiments, error fields or MHD activities could distort the magnetic surfaces, leading to the increase of transport properties. Among those factors, magnetic islands, being resistive MHD tearing modes, exist

commonly in all fusion devices. The formation of magnetic islands relates to the reconnection process of magnetic field lines and this makes the system intrinsically three dimensions. This dissertation presents the transport related study on both RFPs and stellarators.

RFX-mod is currently the biggest RFPs in the world. It is capable of coupling up to 2 MA plasma current and the first observation of the so-called Quasi-Single Helicity (QSH) state has been done on RFX-mod. The dynamo mechanism is related to the nonlinear interactions between the helical magnetic field and the velocity $\left\langle \tilde{\boldsymbol{v}} \times \tilde{\boldsymbol{b}} \right\rangle$, which enters into Ohm's law and plays a role of effective electric field. This mechanism, used to be sustained by the overlap of saturated magnetic islands in Multiple Helicity state, has been theoretically predicated that it can be sustained by only one single tearing mode and it is named Single Helicity state (SH). Experimentally, however, SH has never been observed. Nonetheless, an intermediate state, Quasi-Single Helicity state has been observed on all RFP devices under proper plasma discharge conditions. QSH appears periodically in RFP plasma discharges. It features the inner-most mode growing dominantly (dominant mode), with the rest of the modes (secondary modes) staying at low amplitude. Further experiments reveal the existence of three sub-states in one QSH cycle, named Double Axes state (DAx), Single Helical Axis state (SHAx_n) and SHAx_w with n and w indicating narrow and wide thermal structure. The transport study has been carried out on the three sub-states of QSH. Specifically speaking, the work has been carried out on a selected database containing 208 cases of electron temperature profiles obtained from Thomson scattering diagnostic on RFX-mod. An automatic routine called TeGrA has been developed to get the information of the thermal gradient. For the first time, a complete comparison on thermal properties among these three sub-states has been presented. The role of dominant mode and secondary modes has also been studied.

What is more, the transport study on these three sub-states has been preliminary carried out using a transport code named Multiple Axes Solver (MAxS). Transport study benefits the availability of many well-developed 1.5D transport codes. They are capable of dealing with transport issues with only one single axis. In the case of DAx, however, two magnetic axes bring difficulties and for which, the code MAxS has been developed and benchmarked with ASTRA. The good agreement between these two codes in the benchmark results gives us confidence to move to multiple axis situations. The preliminary results confirmed the results of thermal gradients mentioned above.

And the last part of RFX work is to calculate the total energy confinement time. In this part, an improved method, considering the real shape of the helical flux surfaces has been adopted with the help of code SHEq. The result shows that the total energy

confinement time increases up to 40% from DAx to $SHAx_w$. This result indicates that the plasma enters into more ordered state with the evolution of these three substate and this is confirmed by looking into the global dynamo parameter $(1-F)/\Theta$, which slightly decreases within this evolution process.

For the study on stellarators, the work has been carried on TJ-II stellarator, located in Madrid, Spain. Stellarators poses no toroidal symmetry by its nature. Thus, the neoclassical fluxes are much higher than ones in tokamaks. It has been reported by D. Lópz-Bruna that the magnetic islands in TJ-II play a role of transport barrier and they also modify the local electric field in the vicinity of magnetic islands. Thus, the associated $E \times B$ drift plays a role in L-H transition. This modification on radial electric field is considered that it is due to the modification of non-ambipolar fluxes induced by the presence of magnetic islands. K. C. Shaing has demonstrated that in tokamaks, in the vicinity of magnetic islands, the non-ambipolar fluxes are modified due to the increase of toroidal plasma viscosity and this in turn, leads to the modification of local electric field. Here we adopt the theory developed by Shaing despite of the fact that the theory is derived for tokamaks. The reason is that the physics behind is the that the presence of magnetic island increases the toroidal viscosity which valid both in tokamaks and stellarators. Nonetheless, a geometry factor for stellarators is applied because the neoclassical transport is much higher in stellarators due to its geometry than in tokamaks.

The study on Shaing's theory presents some interesting results. First of all, we consider the steady state situation, i.e., $\partial E/\partial t = 0$. Thus the electric field is obtained from ambipolarity condition $\Gamma_i = \Gamma_e$. The results shows that at both high (above 250 eV) and low (below 105 eV) ion temperature, the ambipolar electric field has only one root and in between of these two values, three roots appears. Besides, the fluxes become ambipolar when the ratio between ion and electron temperature $T_i/T_e = 0.3$. What is more, decreasing the ratio T_i/T_e leads to a sign change of ambipolar electric field, from positive to negative. Meanwhile, the amplitude of electric field also increases. Finally, the plasma density also plays a role in the ambipolar electric field. By increasing the plasma current at a certain percentage, the three-root zone disappears.

Next step, we consider the time evolution of electric field. Here we apply Shaing's formula in ASTRA, together with both Kovrizhnykh's model and Beidler's model. The simulations are performed on a ECRH plasmas in TJ-II. The flux is calculated as $\Gamma = \Gamma^{neoclassical} + \Gamma^{island}$. Here $\Gamma^{Neoclassical}$ is the 'background' flux and it is generated by either of the two neoclassical models mentioned above. First of all, we only take Shaing's model and the result shows that local electric field appears only in the vicinity of magnetic islands. This is true because far from magnetic islands,

the fluxes are intrinsically ambipolar in tokamaks and thus no radial electric field appears. Afterwards, both neoclassical models are applied, together with Shaing's model. The results shows some differences between these two neoclassical models, indicating that the choice of background flux could play a role in the modification process. What is more, the simulations on NBI plasmas in TJ-II shows that the modification effect due to the presence of magnetic islands is always positive.

Contents

Part I

Introduction

1 Toroidal Magnetic Confinement

The human civilization tends to grow exponentially within the last decays, at the same pace of energy usage efficiency and information transportation speed. This brings us the dilemma between the dramatically increased energy demand and the limited energy storage. Hence, effects has been made to find new energy sources, among which, the thermal nuclear fusion is considered to be the most promising one. For the past 60 years, fusion plasmas becomes more and more close to be realized commercially. However, the main issue, energy confinement, remains lower than the target due to the fast energy and particle loss. Fusion energy is considered to be the most promising way of producing energy and great effects have been devoted to the research work of magnetic confinement fusion. This chapter describes the current energy issue as well as a brief introduction on the toroidal magnetic configurations. Also both ideal and resistive MHD theory has been presented to describe the equilibrium. The dynamo mechanism in reversed field pinches is discussed and finally, descriptions on both RFX-mod and TJ-II stellarators have been presented.

1.1 Energy Issue and Plasma Fusion

Looking back to the history of human civilization, it is obvious to see that it is the efficiency of energy consumption and the efficiency of information transportation that determines the level of our civilizations. With the development of our society, the usage of energy increases dramatically, as one could see from Figure 1.1, in which the time trace of energy consumption is listed from year 1965 to year 2015. The total consumption increases up to 3.5 times and it is going to increases more in the following decades. The total energy we could use, however, is finite. Nowadays, we are strongly relying on the so-called traditional energy sources like oil, gas and coal, which are, unfortunately nonrenewable meaning that once they are consumed, there will be no more left(or it will takes too long to recover). The increasing needs for energy are conflicting with the fact of finite energy storage and this brings us a very urgent issue: finding a sustainable way for our civilization. Among countless solutions proposed, the most reasonable one is to find new energy sources and this is being put into practice, as one could see in Figure 1.1. There are many new energy source being explored and used currently but the percentage still remains low

compared with the traditional ones.

Among those new energy sources, nuclear fusion is considered to be on of the most promising in long time term. First of all, the fuels for fusion are nearly 'beyond limit' in the foreseen future. There is huge amount of deuterium (D), one of the isotopes of element hydrogen (H), in sea water and tritium (T), another isotope, can be self-sustained during fusion reactions. Secondly, fusion brings no CO_2 emission, which is considered to be the main reason responsible for green house effect. Thirdly, there is hardly any danger compared with nuclear fission.

The main principle of nuclear fusion is to find a way to "fuse" two nucleus into one and during this process, there should be a mass lossΔm and in most cases, $\Delta m > 0$, through which certain amount of energy will be released according to Einstein's equation: $E = \Delta mc^2$. This huge amount of energy per unit of fuel weight, compared with other ways of energy sources, can be afterwards transformed into electricity. In order to achieve fusion, particles must overcome the repelling Coulomb force which raises the requirement of seeking a way to heat particles up to a sufficiently high energy within sufficiently long time to compensate the energy dispassion. With such high energy, particles like hydrogen, deuterium, etc. will stay excited state in which the electrons are no longer bounded by the nucleus. This new matter state is named plasma, the fourth state of matter after solid, liquid and gas.

Fusion is probably the second most efficient "power plant" prototype in our universe. Our energy source, the sun, is working as a nuclear fusion power plant. The nuclei are pulled together by the huge gravitational force due to the huge mass the sun has. This naturally happened fusion reaction, unfortunately cannot be adopted on earth because there is no way to create such huge amount of mass and control its behavior. There are several ways under consideration for the use of fusion. The first one, inertial fusion, is the one adopted by National Ignition Facility (NIF), USA. It is designed to achieves inertial fusion by means of giving particles enough energy within very short time, thanks to the 192 high power lasers. The simultaneous high power lasers arriving at the fuel target, which is a near perfect sphere, can generate high pressure and push the fuel sphere inwards. During this process, the fuel particles reaches fusion condition within a time so short that they can not be repelled from each other and thus fusion reaction takes place.

A more intuitive way, considering that the fuel is charged particles, uses magnetic field to confine the plasmas. The concept of magnetic confinement for fusion research is the first fusion idea proposed by Russian scientists and now it is the most popular way of fusion research worldwide. The condition of achieving fusion, proposed by Lawson, is related to three plasma parameters: plasma density $n(m^{-3})$, plasma

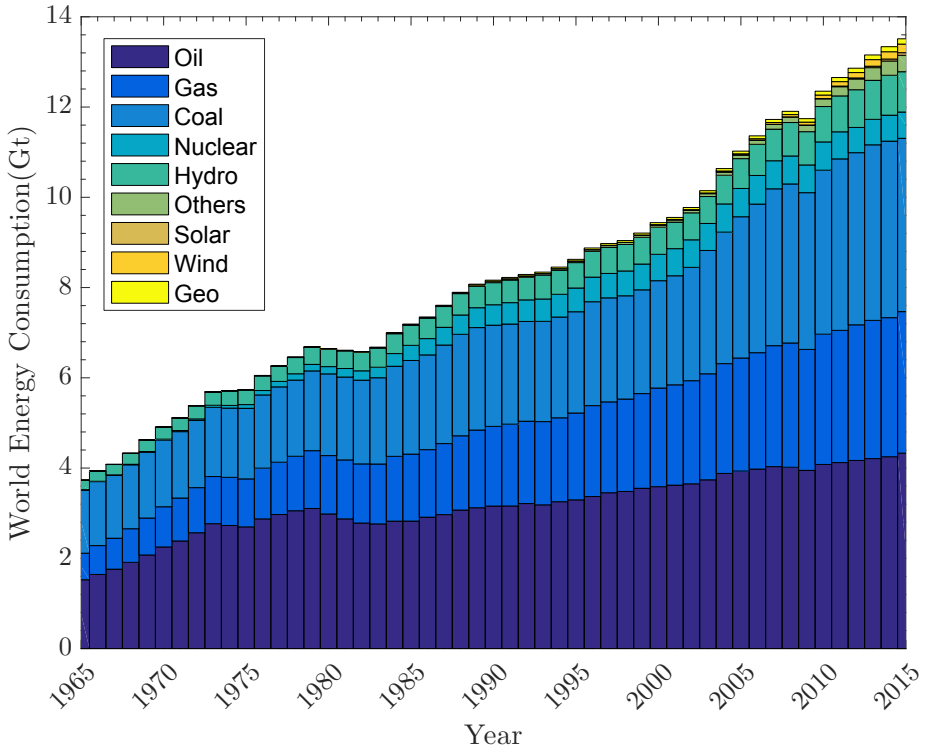

Figure 1.1: World wide energy use between year 1965 and 2015. The data is from British Petroleum.

temperature $T_e(KeV)$ and confinement time $\tau_E(s)$:

$$nT_e\tau_E > 5 \times 10^{21} \quad m^{-3} \cdot KeV \cdot s \tag{1.1}$$

The confinement time is defined as the ratio between internal energy (U) and input power (P):

$$\tau_E = U/P \tag{1.2}$$

From Equation 1.1 it is clear to see that the requirement of fusion is to sustain sufficient large density plasmas at high temperature within sufficient long time. This brings us two main topics: plasma confinement and heating. In principle, any two elements before Fe could have fusion reaction under proper conditions. However, to make story easier, we need to start with the easiest one, i.e. the one with the biggest reaction cross-section. Figure 1.2 shows the cross section of three different fusion

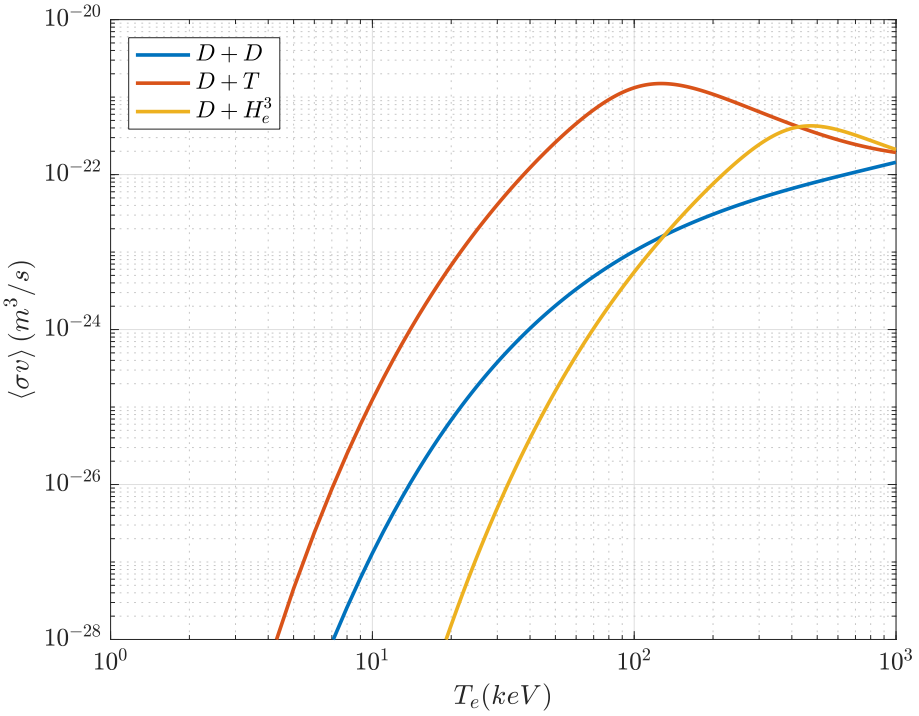

Figure 1.2: Reaction cross section of three typical fusion reactions: D-D, D-T and D-H_e^3. This figure is generated using the formulas presented in Ref [1].

reactions:

$$D + D \rightarrow H_e^3(0.82MeV) + n(2.45MeV)$$
$$D + T \rightarrow H_e^4(3.5MeV) + n(14.1MeV)$$
$$D + H_e^3 \rightarrow H_e^4(3.6MeV) + p(14.7MeV)$$

And it is clear that the $D - T$ reaction has the biggest reaction cross section at a relatively low temperature ($\sim 50keV$). Moreover, one of the products from $D - T$ reaction is helium (H_e) with 3.5 MeV energy, which is considered to be the critical heating source for self-sustained fusion reaction through the so-called α (H_e^4) heating process.

1.2 Toroidal Magnetic Configurations

There have been several configurations proposed and studied for magnetic confinement. They are, depending on the configurations, linear devices and toroidal devices. Linear devices are not suitable for fusion due to end loss issue. By intuition, a toroidal devices without open ends could solve this problem. However, a toroidal device with only toroidal field still suffers bad plasma confinement due to the particle drifts induced by the curvature and gradient of the magnetic field. In order to overcome this issue, a rotational transform ι is introduced to the design of toroidal configurations. The rotational transform measures the winding properties of the field lines.
There are mainly two types of toroidal magnetic configurations categorized by how magnetic field is generated. Tokamaks and Reversed Field Pinches (RFPs), as the magnetic field is generated by both external coils and plasma current, belongs to pinch family. The toroidal field in tokamaks is generated by external coils and the poloidal component is generated by the plasma current, which is induced by the primary transform. In advanced tokamak scenario, however, most of the poloidal field component is generated by the so-called 'bootstrap' current which is induced by the density gradient. Nevertheless, the disadvantage for tokamak configuration is that it suffers a limitation of plasma current due to plasma instability. Consequently, extra heating method besides Ohmic heating is needed for plasma fusion in tokamaks. RFPs, however, can sustain very high plasma current and this makes it to be considered a potential fusion device with only Ohmic heating. On the other hand, the generation of plasma current needs a time variation of magnetic field which is sustained by the primary transform. This time variation makes the devices, on some level, not in steady state. To overcome this problem, a toroidal configuration which all the field components are generated by external coils is introduced. This device is the so-called stellarators. Figure 1.3 shows a sketch of these two families. In the left graph, the red coils aligned toroidally are the toroidal field coils and the green helical ones are helical field coils. In the right graph, the red cylinder in the device center is the primary transformer. The red coils aligned toroidally are the toroidal field coils and the two green ones in the top and bottom of the device is the vertical stabilization coils. The stabilization coils are introduced because due to the existence of Shafranov shift in toroidal devices, the plasma position needs to be optimized in order to avoid touches between magnetic field and the first wall. The stellarator shows a much more complicated magnetic coil design than one in pinch family. Consequently, the manufacture process for magnetic coils are more complex for stellarators than for pinches. On the other hand, due to lack of plasma current in stellarators, it is almost free of disruptions.

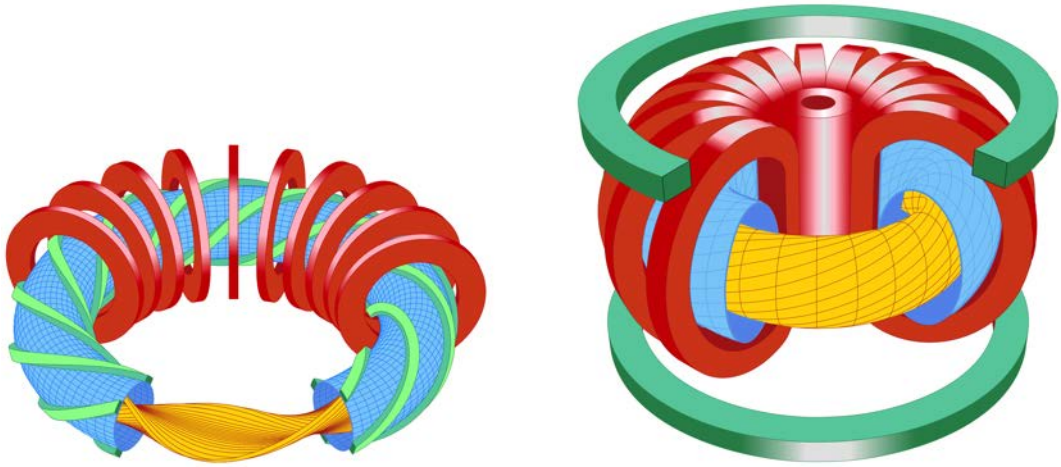

Figure 1.3: Sketch of two types of toroidal magnetic configurations. The left figure represents stellarator family and the right one represents pinch family. The stellarators have complicated coil designs while coils used in pinch family have simpler shape.

The magnetic field designed to confine plasmas in a toroidal configuration contains two component: the poloidal component and the toroidal component. The corresponding coordinate system is the so-called toroidal coordinate system (r,θ,ϕ), defined in Figure 1.4. r is the radial coordinate, θ and ϕ are the poloidal and toroidal angles, respectively. The equilibrium magnetic field has both toroidal and poloidal components and they are linked by the so-called safety factor q. In cylindrical approximation, it is defined as:

$$q(r) = -\frac{r}{R_0}\frac{B_\phi(r)}{B_\theta(r)} \tag{1.3}$$

The safety factor is introduced to describe the winding of magnetic field lines: how many poloidal turns a field line completes before it complete one toroidal circle. Its inverse quantity is the rotational transform $\iota/2\pi = 1/q$.

1.3 Ideal MHD

A large variety of plasma properties, such as the magnetic equilibria or several instabilities can be described by a fluid model called Magnetohydrodynamics (MHD).

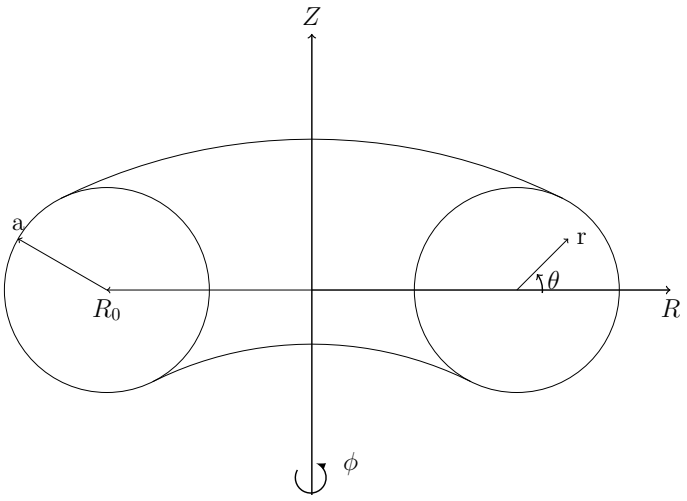

Figure 1.4: A sketch of magnetic coordinate. R_0 is the major radius, a is the minor radius, r is the radial coordinate, θ is the poloidal angle and ϕ is the toroidal angle. The magnetic surfaces share one axis at which $r = 0$.

It contains the fluid equations as well as Maxwell equations. The fluid equations can be derived from Maxwell-Vlasov equation, which is kinetic description of plasmas, by taking different order of velocity moments for distribution functions. The ideal MHD equations, with zero plasma resistivity, are:

$$\textbf{Moment Equations:} \quad \begin{cases} \text{Mass} & \partial\rho/\partial t + \nabla\cdot(\rho\boldsymbol{u}) = 0 \\ \text{Momentum} & \rho(\partial\boldsymbol{u}/\partial t + \boldsymbol{u}\cdot\nabla\boldsymbol{u}) = -\nabla P + \boldsymbol{J}\times\boldsymbol{B} \\ \text{Energy} & \dfrac{d}{dt}\left(p/\rho^{\gamma}\right) = 0 \end{cases}$$

$$\textbf{Maxwell Equations:} \quad \begin{cases} \text{Gauss's Law} & \nabla\cdot\boldsymbol{B} = 0 \\ \text{Gauss's Law} & \nabla\cdot\boldsymbol{E} = q/\epsilon_0 \\ \text{Ampere's Law} & \nabla\times\boldsymbol{B} = \mu_0\boldsymbol{J} \\ \text{Faraday's Law} & \partial\boldsymbol{B}/\partial t = -\nabla\times\boldsymbol{E} \\ \text{Ohm's Law} & \boldsymbol{E} + \boldsymbol{u}\times\boldsymbol{B} = 0 \end{cases}$$

Where ρ is the mass density, $\boldsymbol{u}$ is the flow velocity, P is the pressure, $\boldsymbol{J}$ is the current, $\boldsymbol{B}$ is the magnetic field, $\boldsymbol{E}$ is the electric field, q is the charge, ϵ_0 is the vacuum permittivity and μ_0 is the vacuum permeability. The basic assumptions used to derive ideal MHD equations are:

- Quasineutrality
- Plasma typical length $\gg$ Larmor radius
- Typical frequency $\ll$ Cyclotron frequency
- Zero resistivity and viscosity
- No trapped particles (no neoclassical effects)

Here the Larmor radius is the gyration radius of charged particles along a field line and it is given as $\rho = mv_\perp/q|B|$ with m the particle mass, $v_\perp$ the velocity component perpendicular to the field line, q is the charge of particles and B is the modulus of magnetic field. To study time evolution of perturbations, any physical quantity A could be written as $A = A_0 + A_1$ with $A_0 \gg A_1$. In equilibrium state, which is required by steadily operated fusion devices, we have: $\partial A_0/\partial t = 0$ and $\boldsymbol{u} = 0$. Thus the equilibrium condition could be easily obtained from the 8 equations mentioned above:

$$\boldsymbol{J} \times \boldsymbol{B} = \nabla P \tag{1.4}$$

Equation 1.4 shows that a plasma equilibrium is sustained by the force balance between $\boldsymbol{J} \times \boldsymbol{B}$ and the pressure gradient ∇P. Moreover, it also shows that both plasma current and the magnetic field lies on a surface defined by constant pressure. This can be easily approved by applying dot product of $\boldsymbol{J}$ and $\boldsymbol{B}$ on Equation 1.4 respectively. These surfaces with constant gradient are the so-called flux surfaces. Charged particles which follow the field lines are thus bonded on the surfaces and the radial energy or particle loss are significantly reduced and the only loss is due to the collisions between particles. The field lines are winding on the flux surfaces in the helical direction. A sketch of flus surfaces, helical field line as well as the gyration of a charged particle along one magnetic field line is shown in Figure 1.5. The yellow torus represents the flux surfaces and the black helical lines represents the magnetic field lines which lies on the surfaces. The small winding along the center field line represents the gyration motion of a charged particle. Note that the gyration is not in the correct scale rather than a sketch.

The shape of the magnetic surfaces varies with the magnetic field condition and it always has the Shafranov shift due to the toroidal configuration. The Shafranov shift is induced by the toroidicity in the sense that on one flus surface, the area in high field side S_H is smaller than in low field side S_L and thus a net force towards low field side is generated: $P(S_L - S_H)$. Figure 1.6 shows a sketch of Shafranov shift in circular plasmas. The black circle is the vacuum chamber and the red circle represents the equilibrium plasma cross-section. The shift between the vacuum chamber

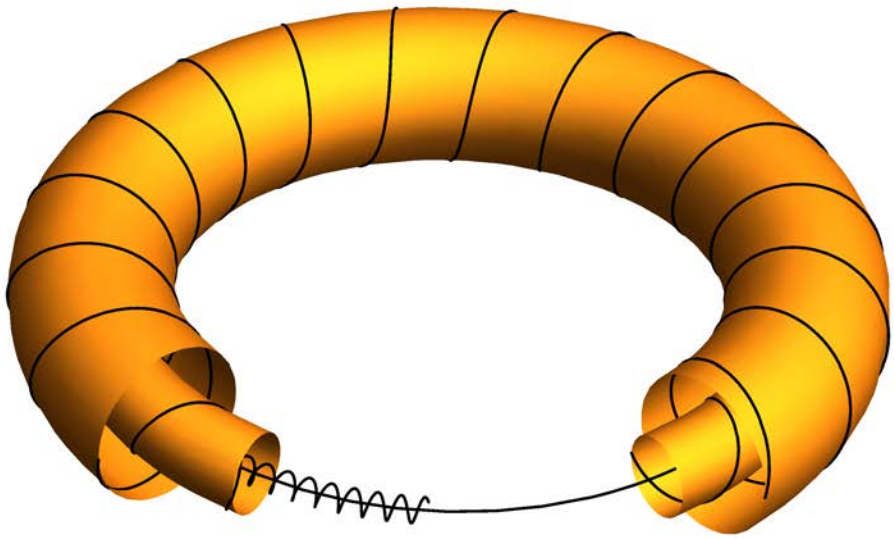

Figure 1.5: A sketch of flus surfaces, field lines (black helical) and the gyration of a charged particle along one magnetic field line (the black half spring in the center, not in scale with the torus) is presented.

center and the plasma equilibrium center $\Delta(r)$ is the Shafranov shift. This simplified model shows that all the flus surfaces are shifted towards low field side and since in general the Shafranov shift depends on r, the value is different for each flux surfaces.

The existence of Shafranov shift leads to a different metric tensor compared to the concentric circle configuration and this brings complicity in transforming between Cartesian coordinate and flux coordinate. For quantities which are function of flux surfaces like the temperature, density, current, etc., the use of flux coordinates allows one write simpler equations to study various phenomena such as stability and transport. Moreover, things could get more complicated if the topology of magnetic field is modified further by other phenomena.

1.4 Resistive MHD

In the framework of ideal MHD, the main assumption is that the plasma resistivity is zero. The consequence is that the plasma topology remains unchanged. However, even a small, non-zero plasma resistivity could change the field topology and this introduces further complexity into the metric. The theory considering a finite plasma

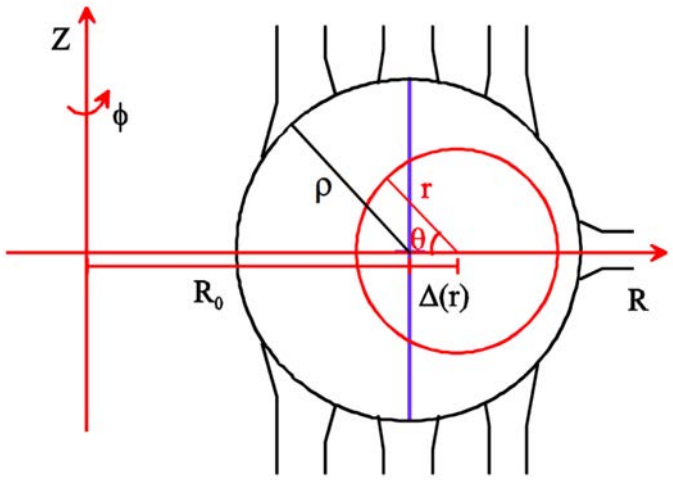

Figure 1.6: A sketch of Shafranov shift in a circular plasma. ϕ is the toroidal direction, Δr is the Shafranov shift.

resistivity is called *resistive MHD*. Here we consider the plasma with a non-zero resistivity η. The corresponding Ohm's law is:

$$\boldsymbol{E} + \boldsymbol{v} \times \boldsymbol{B} = \eta \boldsymbol{J} \tag{1.5}$$

Together with Faraday's Law and $\nabla \times \boldsymbol{B} = \mu_0 \boldsymbol{J}$, using the vector relation $\nabla \times \nabla \times \mathcal{A} = \nabla(\nabla \cdot \mathcal{A}) - \nabla^2 \mathcal{A}$, the induction equation is obtained:

$$\partial \boldsymbol{B}/\partial t = (\eta/\mu_0)\nabla^2 \boldsymbol{B} + \nabla \times (\boldsymbol{v} \times \boldsymbol{B}) \tag{1.6}$$

This The dimensionless form of induction equation is thus:

$$\partial \boldsymbol{B}/\partial \hat{t} = (1/R_m)\hat{\nabla}^2 \boldsymbol{B} + \hat{\nabla} \times (\hat{\boldsymbol{v}} \times \boldsymbol{B}) \tag{1.7}$$

Where $\hat{t} = tV_A/L$, $\hat{\nabla} = L\nabla$, $\hat{\boldsymbol{v}} = \boldsymbol{v}/V_A$ and L is the typical plasma length. $R_m = \mu L V_A/\eta$ is the so-called Reynolds number and it is also referred to as the Lundquist number $S = \tau_R/\tau_A$ where $\tau_R \sim \mu_0 L^2/\eta$ is the characteristics resistive diffusion time and $\tau_A \sim L/V_A$ is the Alfvén time. The Lundquist number is a quantity indicating how far the plasma is from the ideal MHD, i.e., when $S \to \infty$, the plasma is close to ideal MHD. On the right side of induction equation, there are two parts. When the resistivity $\eta \to 0$, the induction equation becomes to the form ideal MHD. The plasma moved with the field lines. When $(1/R_m)\hat{\nabla}^2 \boldsymbol{B} > \hat{\nabla} \times (\hat{\boldsymbol{v}} \times \boldsymbol{B})$, the induction

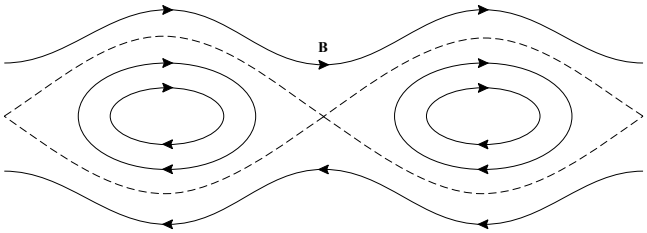

Figure 1.7: A typical magnetic island is presented. The field lines reconnect and the topology of magnetic field changes.

equation becomes a diffusion equation of the field lines.

One of the most important result from resistive MHD is the so-called tearing mode. The magnetic perturbations in general tend to bend the magnetic field lines. This bending effect increases the magnetic field energy. This is true as long as the wave vector of the perturbation $\boldsymbol{k}$ is not perpendicular to the field lines: $\boldsymbol{k} \cdot \boldsymbol{B} \neq 0$. In such conditions, the magnetic perturbations play a positive role in stabilization of magnetic field by increase the magnetic energy. However, this stabilization effect vanishes when $\boldsymbol{k} \cdot \boldsymbol{B} = 0$. In cylindrical approximation, $\boldsymbol{k} \equiv \boldsymbol{k}(r) = (k_r, k_\theta, k_\phi)$. With the wave length in poloidal direction $\lambda_\theta = 2\pi r/m$ and in toroidal direction $\lambda_\phi = 2\pi R/n$, the wave vector in these two directions are $k_\theta = m/r$ and $k_\phi = n/R$. Hence, the unstable condition is:

$$\boldsymbol{k} \cdot \boldsymbol{B} = k_\theta B_\theta + k_\phi B_\phi = 0 \tag{1.8}$$

Recall the defination of safety factor q, the equation 1.8 can be written as:

$$q(r) = -\frac{r}{R}\frac{B_\phi}{B_\theta} = -\frac{m}{n} \tag{1.9}$$

Now we arrives a critical point that the unstable positions are ones where the mode number m and n are rational numbers. The result of tearing mode is that it modifies the magnetic topology through reconnection process of magnetic field lines. Figure 1.7 shows a typical magnetic island after reconnection of field lines. The reconnection of field lines occurs in the resonant position and the topology of magnetic field thus changed. The existence of magnetic islands distorted the nested flux surfaces and gives rise of three dimensional properties of the transport process.

1.5 Equilibrium in RFPs: the Dynamo Mechanism

In a typical RFP discharge, the poloidal component of the magnetic field (B_θ) is comparable with toroidal component (B_ϕ) in amplitude and B_θ dominants in the outer region where B_ϕ reaches zero value and changes sign. This magnetic configuration is quite different from ones in tokamaks where toroidal field B_ϕ is much larger than poloidal field B_θ. Moreover, the safety factor profile in RFPs features $q < 1$ and its sign changes in the edge. A typical magnetic field profiles with poloidal and toroidal components are shown in Figure 1.8(a), plotted as a function of the radius normalized by minor radius a of the poloidal cross-section. The corresponding q profile in RFX-mod is shown in Figure 1.8(b). This unique q profile, different from the one in tokamaks ($q > 1$), leads to the possibility of many MHD tearing modes, as the symbol dots shown in Figure 1.8(b). In the plasma center, tearing modes resonant and overlap with each other, breaking the nested flux surfaces, leading to a degradation of plasma confinement with increased transport properties.

The edge reversal of toroidal magnetic field is a self-organized behavior, by means of so-called dynamo mechanism which is related to the non-linear interactions of MHD tearing modes. To be more specific, the non-linear interactions between resonant modes generate a non-zero part of $\left\langle \tilde{\boldsymbol{v}} \cdot \tilde{\boldsymbol{b}} \right\rangle$ in Ohm's law with symbol $\langle \cdots \rangle$ meaning average value, playing a role of effective electric field. The none zero $\left\langle \tilde{\boldsymbol{v}} \cdot \tilde{\boldsymbol{b}} \right\rangle$ connects between toroidal current and poloidal current and as a consequence, part of the poloidal current is generated by the toroidal current through the dynamo mechanism.

A physical picture of the dynamo mechanism is presented in order to get a better understanding. A RFP discharge is presented in Figure 1.9, with magnetic (upper graph) and current (lower graph) profiles along the normalized minor radius. The vertical dashed line represents the radial location of the reversal point, where the toroidal field B_ϕ reaches zero. It is clear to see that at the the value of poloidal current $\boldsymbol{j}_\theta$ is not zero. By checking the induction equation and Ohm's law in the reversal location: $\partial \boldsymbol{B}/\partial t = -\nabla \times \boldsymbol{E}$ and $\boldsymbol{E} + \boldsymbol{v} \times \boldsymbol{B} = \boldsymbol{\eta J}$, one obtains $\boldsymbol{E}_\theta = 0$ and $\boldsymbol{E}_\theta = \boldsymbol{\eta J}_\theta$. The following result $\boldsymbol{J}_\theta = 0$ disagrees with the discharge profile. In fact, the poloidal current at the reversal location is not generated by $\partial \boldsymbol{B}_\phi/\partial t$. Instead, it is generated through the dynamo mechanism mentioned above.

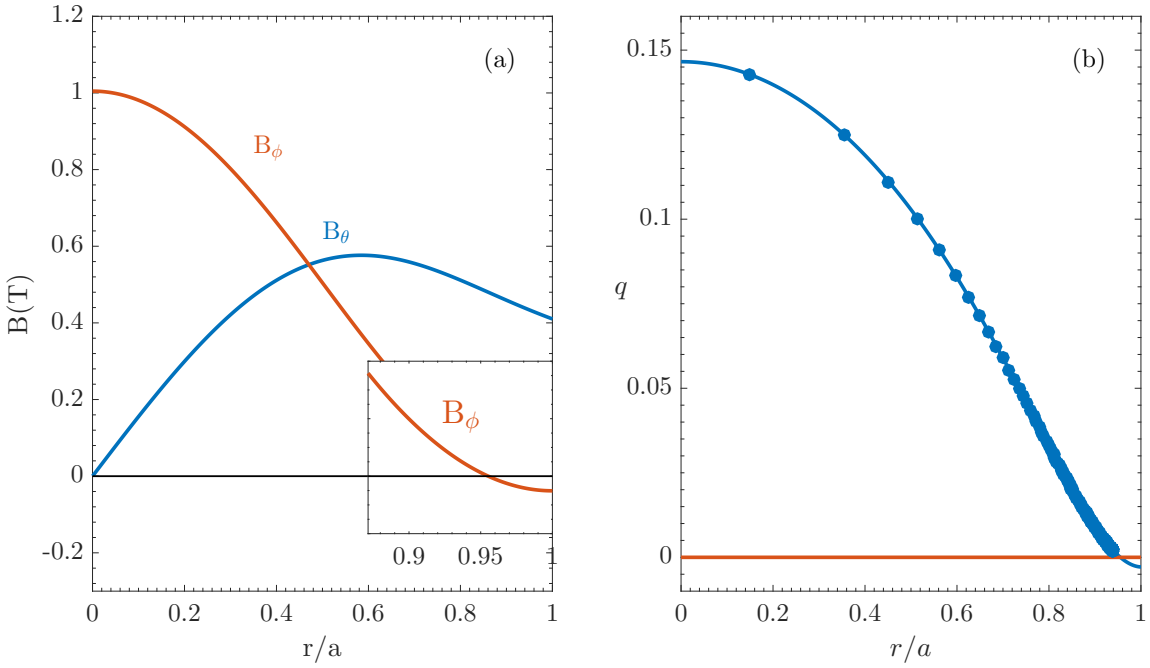

Figure 1.8: (a). A typical magnetic field profile in a RFX disachrge is presented with both poloidal (in blue) and toroidal (in red) components, with the black herizontal line representing $\boldsymbol{B} = 0$. The amplitude of poloidal field dominants in the edge and the toroidal field changes sign near the edge. (b). The corresponding safety factor q profile is presented as a function of the minor radius normalized by the minor radius. The circle markers on the curve are the corresponding resonant MHD modes with the horizontal line indicating $q = 0$.

Taylor Relaxation Theory

The first explanation of the RFP configuration was proposed by J. Brian Taylor [2]. The main principle of his theory is that plasma are seeking the minimum energy by neglecting the pressure and velocity:

$$W = \int_V \frac{B^2}{2\mu_0} dV \tag{1.10}$$

The constrain comes along is that the system has constant magnetic helicity:

$$K = \int_V \boldsymbol{A} \cdot \boldsymbol{B} dV \tag{1.11}$$

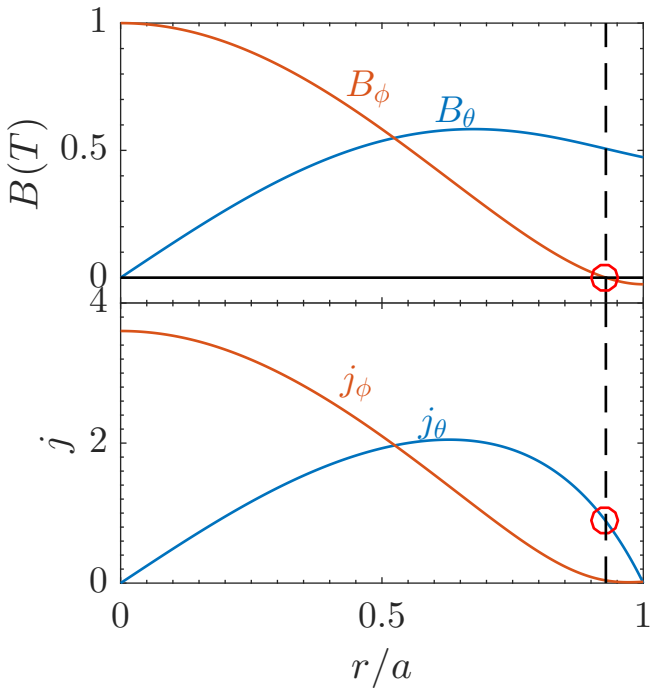

Figure 1.9: A model for one RFP plasma discharge. The profiles of two magnetic field components B_ϕ and B_θ are presented in the upper graph, plotted as a function of the normalized minor radius. The two corresponding current density profiles $\boldsymbol{j}_\phi$ and $\boldsymbol{j}_\theta$ are presented in the lower graph.

where $\boldsymbol{A}$ is the vector potential defined as $\boldsymbol{B} = \nabla \times \boldsymbol{A}$. It is true that the magnetic helicity is conserved in non-resistive plasmas. When it comes to resistive plasmas, K is considered to be approximately constant if the variation of K is much slower than the magnetic energy variation[3].
By checking the force balance equation: $J \times B = \nabla P = 0$, one obtains a force free system with $J = \mu B$, with μ a constant. In cylindrical configuration, the solutions are Bessel functions for J_0 and J_1:

$$\begin{cases} B_r(r) = 0 \\ B_\theta(r) = B_0 J_1(\mu r) \\ B_z(r) = B_0 J_0(\mu r) \end{cases}$$

The above mentioned theory developed by Taylor shows that the plasma behavior seems only to be affected by the global parameters. Hence, before further discussion,

we define two global plasma parameters: reversal parameter $F = B_\phi(a)/\langle B_\phi \rangle$ and pinch parameter $\Theta = B_\theta(a)/\langle B_\phi \rangle$ with $B_\theta(a)$ and $B_\phi(a)$ the poloidal and toroidal magnetic field in the edge, respectively. The symbol $\langle \cdots \rangle$ indicates the volume average. The comparison between Taylor's theory and the experimental data shows a disagreement, especially in the plasma edge. A modified theory, adopting a non-constant μ along the normalized minor radius r/a as well as considering a non-zero pressure, shows a good agreement with experimental data.
The dynamo effect has been shown that it is a global RFP plasma behavior. This self-organized plasma behavior allows the plasma current which flows in toroidal direction, flows in the poloidal direction and part of the toroidal field is thus generated by the toroidal plasma current through this mechanism. The contribution of the toroidal magnetic field via dynamo mechanism can be expressed as:

$$\langle B_\phi \rangle = \langle B_{\phi,dynamo} \rangle + B_\phi(a) \tag{1.12}$$

$\langle B_{\phi,dynamo} \rangle$ is the average paramagnetic toroidal field self-generated through dynamo mechanism. Hence, this quantity is an indicator for the dynamo mechanism. One can easily get:

$$(1 - F)/\Theta = \langle B_{\phi,dynamo} \rangle / B_\phi(a) \tag{1.13}$$

So the quantity $(1 - F)/\Theta$ is the dynamo parameter for RFP plasmas.

1.6 Experimental Devices

The thesis work has been carried on two machines: the RFX-mod and the TJ-II stellarator. Here brief descriptions together with main diagnostics of these two toroidal configurations are presented.

Revered Field eXperiment

The Reversed Field eXperiment modified (RFX-mod) is currently the largest RFP in the world, located in Padova, Italy. It has a major radius of $R = 1.99m$ and a minor radius of $a = 0.459m$. It is capable to reach plasma current up to 2 MA. Figure 1.10 shows the bird view of the device. One of the most innovations in RFX-mod is the new feedback control system based on 192 active saddle coils covering the whole plasma volume (4 poloidally and 48 toroidally). This new feedback system functions to suppress the radial magnetic perturbations. Here a brief description of diagnostics on RFX-mod is present.

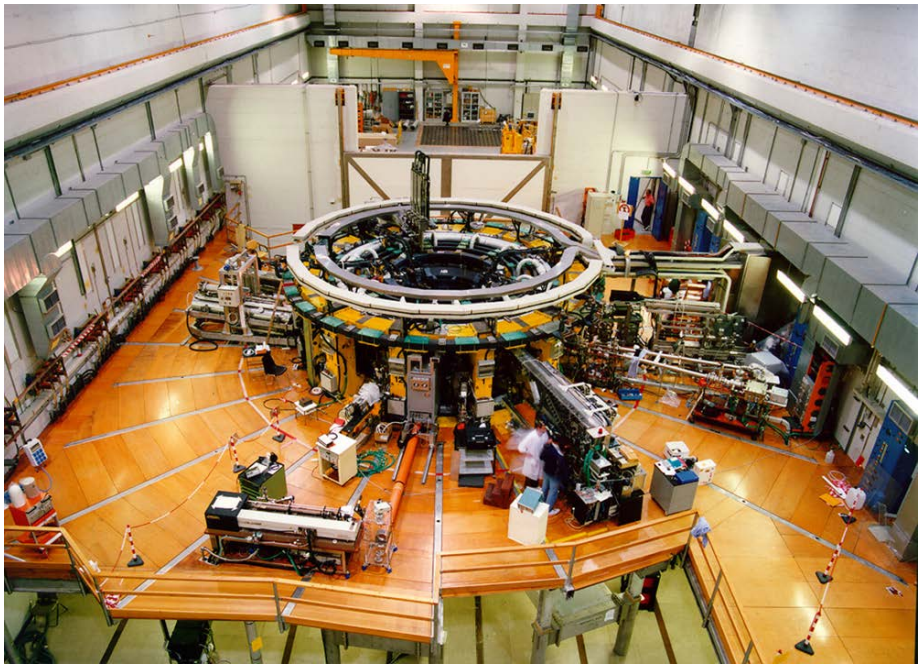

Figure 1.10: A birdview of the RFX-mod device, located in Padova, Italy.

- Magnetic diagnostics. Four Rogowski coils between the vacuum vessel and the shell for measurement of toroidal magnetic flux as well as plasma current. (8 toroidal and 6 poloidal voltage loops for measurements of flux variations.) 192 pick-up coils, distributed along 48 toroidal directions and 4 poloidal directions, measure toroidal and poloidal components of magnetic fields. 192 saddle probes distributed the same as the pick-up coils, measuring the radial component of the field, coupled to the active control coils.

- Tomographic reconstruction [4]. It is meant for the reconstruction of the poloidal emissivity map. The diagnostic is composed by 3 vertical fans each with 19 lines of sight and 1 horizontal fan with 21 lines of sight. The total 78 lines of measurements almost entirely cover the plasma cross section.

- Thomson scattering diagnostic [5]. It features spacial resolution of 84 points along the diameter of the vacuum chamber. The laser path lays on the mid-plan (poloidal angle $\theta = 0(\pi)$) with toroidal angle $\phi = 82.5°$. The maximum capacity per discharge is around 20:25 pulses.

- A multi-chord interferometer [6, 7]. It measures the electron density averaged

along 14 lines of sight. The measurement is performed measuring the phase variation induced in a CO_2 laser beam ($\lambda = 5.4\mu m$) that passes through the plasma.

- Spectroscopic diagnostics [8]. It measures line intensities of radiation emitted by main gas and by impurities, in order to calculate their influxes at the edge, the toroidal flow of the plasma and the effective charge.

- Soft-X Rays multi-filter diagnostic [9]. It is used for measuring electron temperature at the center of the plasma by means of comparing SXR emissions measured by differently filtered silicon detectors. It allows a higher time resolution with respect to the Thomson scattering, but with a lower spatial resolution; 4 chords with different filter thicknesses (40 μm, 75 μm, 100 μm, 150 μm) are used in order to measure temperature in a wider range of emission levels.

- an integrated system of internal sensors (ISIS) [10], which includes poloidal and toroidal arrays of 139 magnetic pick-up coils and 97 electrostatic (Langmuir) probes (used to measure and correlate fluctuations of electric and magnetic fields), and 8 calorimetric sensors.

TJ-II Stellarator

TJ-II stellarator flexible Heliaca under operation in CIEMAT, Madrid, Spain. It has a major radius $R = 1.5m$ and minor radius $a = 0.22m$. The magnetic field on axis is up to $1.2T$. Figure 1.11 shows a perspective view of TJ-II. In TJ-II, the magnetic trap is obtained by means of various sets of coils that completely determine the magnetic surfaces before plasma initiation. The toroidal field is created by 32 coils. The three-dimensional twist of the central axis of the configuration is generated by means of two central coils: one circular and one helical. The horizontal position of the plasma is controlled by the vertical field coils. The combined action of these magnetic fields generate bean-shaped magnetic surfaces. The heating systems are: Electron Cyclotron Resonant Heating, Neutral Beam Injection (NBI), Electron Bernstein Wave Heating. The fueling systems are Gas puff, NBI and Pellet injector. There are both passive and active diagnostic systems installed on TJ-II. Here listed briefly the main diagnostic systems installed on TJ-II. The main passive diagnostics are:

- A set of magnetic field diagnostic. There are two straight arrays of Mirnov coils and one poloidal array with 15 coils. The mirnov coils are with cylindrical shape and they measure the position of plasmas. Besides, there are two sets

of Rogowski coils installed to measure the poloidal magnetic flux. Also two internal diamagnetic loops are installed to provide the toroidal loop voltage.

- Electron Cyclotron Emission [11]. Electron temperature profiles are measured at TJ-II by means of a 16 channel heterodyne radiometer, covering the frequency range 50-60 GHz, corresponding to the second harmonic of electron cyclotron emission (ECE) in X-mode polarization at a magnetic field of 0.95 T on the plasma axis.

- Soft X-rays. The TJ-II multichannel soft X-ray system consists of 5 cameras with 16 channels each, allowing tomographic reconstruction of the plasma emissions

- Bolometry. Three 20-channel pinhole cameras, monitoring the same poloidal section and used for tomographic reconstructions of the total plasma emissivity.

- Four spectroscopy system: 1. Multichannel system with nine-channel, high-resolution, spectroscopic diagnostic system for measurements of ion impurity temperature and poloidal rotation via passive emission spectroscopy. 2. Toroidal rotation measurement. 3. Vacuum ultraviolet spectrometer (VUV) spectroscopy, covers wavelength from 20 to 300 nm on the purpose of obtaining the impurity ion temperature as well as its time evolution. 4. Charge exchange recombination spectroscopy.

- Charge Exchange Spectroscopy. It is used to obtain the ion temperature profile, assuming a Maxwellian energy distribution function.

- Fast Camera is installed for various studies like turbulence, dust, 2-dimensional electron and ion temperature imaging.

The main active diagnostics are:

- Interferometry [12] contains two parts: the microwave interferometer located at $\phi = 264.4°$. The probing beam has an inclination of 18.7° with respect to the vertical and a frequency of 140 GHz, corresponding to a wavelength of $\lambda = 2.14$ mm. There is also a two-color interferometry (CO_2 with 10.6 μm and NdYAG with 1.064 μm) provides the line integrated density.

- The reflectometry contains three parts: an amplitude modulation reflectometry system [13]; a fast frequency hopping reflectometer [14] and a doppler reflectometer [15]. The amplitude modulation reflectometry is used for density

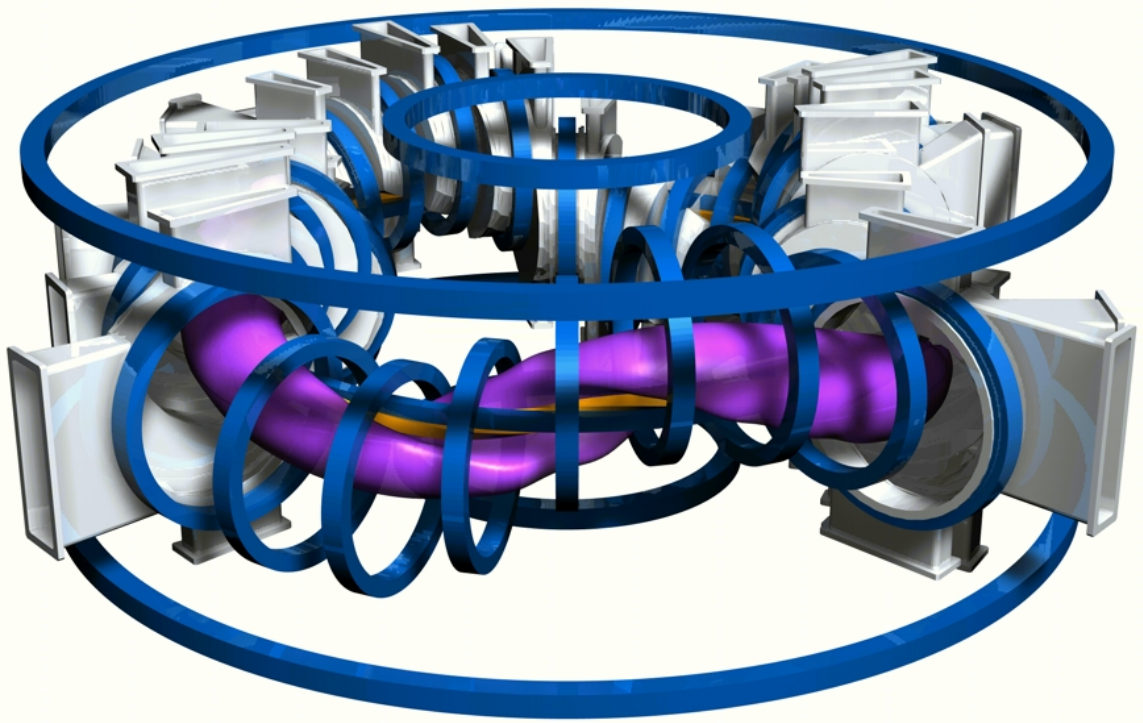

Figure 1.11: A sketch of TJ-II stellarator is presented.

profile measurement with a temporal resolution of 2 ms. The fluctuation reflectometer works in the frequency range between 33-50 GHZ and it was used to study the velocity shear layer and the radial position of its origin. Doppler reflectometer, located at $\phi = 337°$ measures plasma density fluctuation velocities and their wave number spectra. The spacial resolution of doppler reflectometer is about $r/a = 0.6 : 0.9$ with a the minor radius. The perpendicular wavenumber can be selected between $k_\perp = 3$ and $15cm^{-1}$.

- Heavy ion beam probe [16] has been installed for measurements of plasma electric potential, electron density and poloidal magnetic field component. These quantities are measured at one plasma location and it can scan through the plasma cross-section.

- Two Langmuir probe system [17] installed at position $\phi = 38.2°, R = 134cm$ and position $\phi = 195°$ for plasma potential and plasma density measurements. Also it can provides turbulence information. Several designs of the probe can

be mounted into the system like a rake probe, a multi-pin probe and a biasing probe.

- Thomson scattering diagnostic [18] located at $\phi = 14.5°$. It provides electron temperature, density and pressure profiles in a single discharge.

2

Three Dimensional Transport Induced by the Presence of Magnetic Islands

Transport is a common phenomenon in fusion devices. The transport is induced by the collisions between particles and through which, mass, momentum and energy are transferred. Consequently the transport phenomenon strongly affects the plasma confinement properties. The transport study in toroidal symmetry configurations with nested flux surfaces like tokamaks or helical symmetry with nested flux surfaces like stellarators can be treated on 1.5 dimensional level. The kinetic quantities like temperature, density are functions of flux surfaces and thus they can be averaged over the radial and poloidal directions. However, the existence of magnetic islands in above mentioned devices breaks the symmetry as well as nested flux surfaces, giving rise a ***three dimensional*** *transport process. In RFPs, similar situation with many tearing modes resonating also brings up three dimensional transport problems. This chapter describes the three dimensional transport induced by the presence of magnetic islands. General descriptions on both neoclassical transport and stochastic transport theory are also presented.*

2.1 Neoclassical Transport

Neoclassical transport is a theory describing the transport process due to Coulomb collisions in quiescent state, considering the field inhomogeneity of field lines induced by the toroidicity of the configuration. Compared with classical transport theory, it considered the complex geometry of the field, which gives rise to more complex particle orbits and drifts than Larmor radius and gyration motion of charged particles. Here we introduce the main particle drifts induced by the toroidicity in toroidal magnetic configurations developed within the framework of neoclassical transport theory. First of all, applying Faraday's law:

$$\nabla \times \boldsymbol{B} = \mu_0 \boldsymbol{j} \tag{2.1}$$

we have the toroidal magnetic field:

$$\boldsymbol{B}_\phi = \mu_0 j/(2\pi r)\boldsymbol{e}_\phi \tag{2.2}$$

This is the dominant part in tokamaks and it is inverse proportional to the radius r. $\boldsymbol{j}$ is the total poloidal current following in the coils, r is the radius from the toroidal geometry center and $\boldsymbol{e}_\phi$ indicates the toroidal direction. Now consider the first adiabatic invariant, magnetic moment $\mu = mv_\perp^2/2B$, the Larmor radius, $\rho = mv_\perp/|q|B$ becomes:

$$\rho = (2m\mu/B)^{1/2}/q \tag{2.3}$$

Where q is the charge carried by particles. Clearly, Larmor radius varies as the magnetic field strength changes. The Larmor radius is smaller in high field side than one in low field side. Accordingly, particles follows a much bigger orbit than Larmor radius. This new particle orbit is named as banana orbit, as its poloidal projection is like a banana. Figure 2.1 shows the particle trajectory on poloidal plan. Particle trajectories within this banana orbit is named trapped particles and particles who can exploring the whole plasma volume, i.e., the poloidal cross-section of their trajectories are complete circles. The boundary between trapped and passing particles is shown in velocity phase space in Figure 2.2. The gray shadow is the trapped region and the white region is the passing region. The critical angle θ_c defines the boundary. The fraction f of the trapped particles is $f = \cos\theta_c \approx a/R = \epsilon$. Here ϵ is the inverse respect ratio defined as the ratio between minor radius a and major radius R. This banana orbit particle trajectory followed is caused by the non-uniformity of magnetic field in toroidal configurations. Note that the Figure 2.2 shows a situation with no density gradient, i.e., the trapped particles between two neighboring banana orbits are equal. However, in a toroidal magnetic configurations, there exists the density gradient, which gives rising the unbalance of trapped particles between adjacent banana orbits. This will leads to momentum transfer between trapped particles and passing particles and consequently a net toroidal current is formed and this is the so-called bootstrap current. In advanced tokamak scenario, the bootstrap current could take a significantly part of the whole toroidal plasma current (in ITER, the designing is up to 70%).

Besides the banana orbit, another effect caused by this field non-uniformity leads to a particle drift motion:

$$\boldsymbol{v}_d = \frac{\mu}{q}\frac{\boldsymbol{B}\times\nabla\boldsymbol{B}}{\boldsymbol{B}^2} \tag{2.4}$$

The direction of this drift velocity depends on the sign of the particle charge. Consequently, it leads to a charge separation and a local vertical electric field is naturally appears. With the presence of the local electric field, another particle drift motion, deducted from momentum equation easily, will occur:

$$\boldsymbol{v}_d = (\boldsymbol{E}\times\boldsymbol{B})/B^2 \tag{2.5}$$

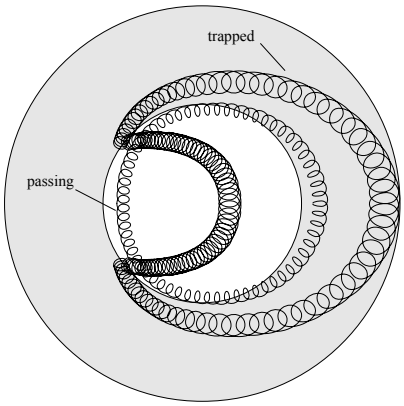

Figure 2.1: A sketch of banana orbit on the poloidal projection in tokamaks. This figure is from Reference [19].

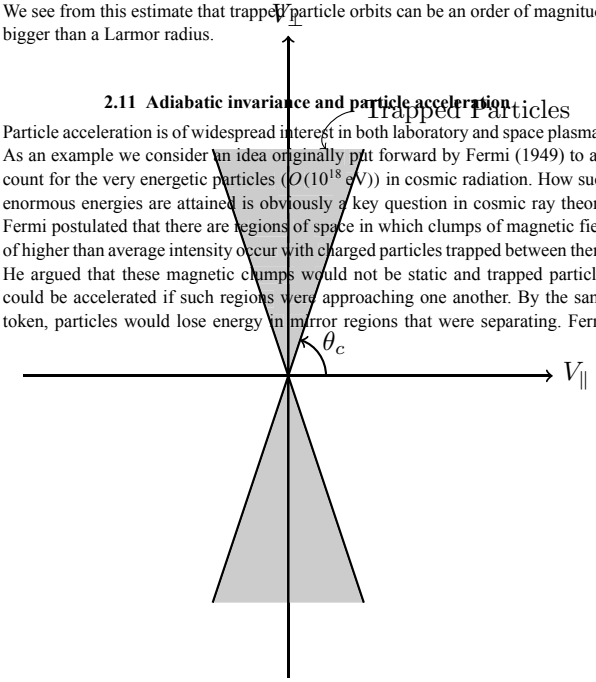

Figure 2.2: Velocity space showing the trapped-passing boundary. The critical angle θ_c defines the so-called loss cone which is the white space.

This drift motion is towards outwards, which could leads to serious degradation of plasma confinement. A rotational transform of the field lines, ι thus is realized in order to average this vertical charge separation. It is defined as the poloidal angle when particles complete one toroidal circle divided by 2π:

$$\frac{\iota}{2\pi} = \frac{d\psi}{d\Phi} = \frac{1}{q} = \frac{n}{m} \tag{2.6}$$

Where q is the safety factor, m and n are the poloidal and toroidal mode number, ψ and Φ are poloidal and toroidal magnetic flux, respectively, defined as follows:

$$\psi = \iint_{\boldsymbol{S}_\psi} \boldsymbol{B} \cdot d\boldsymbol{S}$$
$$\Phi = \iint_{\boldsymbol{S}_\phi} \boldsymbol{B} \cdot d\boldsymbol{S}$$

Where $\boldsymbol{S}_\psi$ and $\boldsymbol{S}_\phi$ are the area with its vector in the poloidal and toroidal direction, respectively.
The third important particle drift is the so-called curvature drift, which is generated by the curvature of field lines. A particle moves along a curved path, there is a centrifugal force, which in turned generates this particle drift in a magnetic field. It is defined as:

$$\boldsymbol{v}_d = m\boldsymbol{v}_\parallel^2(\boldsymbol{B} \times (\boldsymbol{B} \times \nabla)\boldsymbol{B})/eB^4 \tag{2.7}$$

By far we defined two kinds of particle drifts which commonly exist in fusion plasmas. These drifts enters the flux function, whose time evolution is:

$$\partial\mathcal{A}/\partial t = \nabla \cdot (\Gamma) + \mathcal{S} \tag{2.8}$$

Where $\mathcal{A}$ is particle density (particle transport) or energy density (energy transport), $\Gamma = D\nabla\mathcal{A}$ is the particle or energy flux with D the diffusion coefficient, and $\mathcal{S}$ is the source or sink. Note here the non compressive assumption is taken ($\nabla \cdot (\boldsymbol{v}\mathcal{A}) = 0$). For a tokamak case, a sketch of diffusion coefficient D versus the normalized collision frequency $\nu^* = \nu/\omega_b$ with ω_b the bounce frequency, is presented in Figure 2.3. The banana region is when $\nu^* \leqslant 1$ and this region is called *low collisionality* region. Particles in this region complete many banana orbits before they collide with each other. Here the bounce frequency $\omega_b = v/(Rq)$ is the frequency for trapped particles to complete the banana orbit.

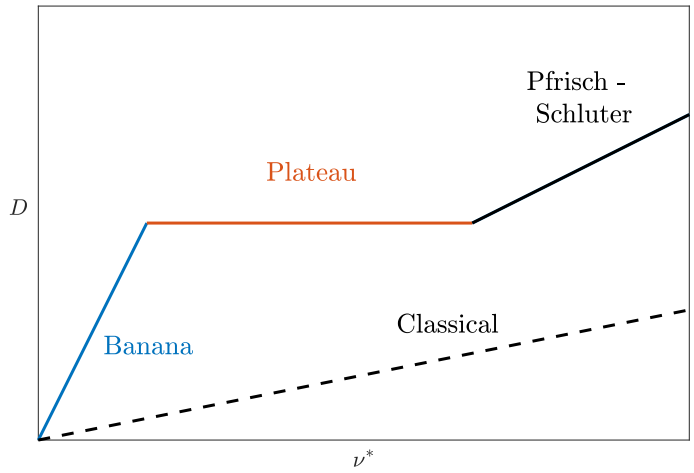

Figure 2.3: Diffusion coefficient D is plotted in log-log scale, as a function of collisionality ν^*. The solid line represents the neoclassical transport and the dashed line represents the classical transport. This plot is valid in magnetic configurations with toroidal symmetry. It starts with banana region, in which the collision frequency is lower than bounce frequency. Particles within this region are trapped inside of the banana orbit.

2.2 Stochastic Transport

In RFP plasmas, many MHD tearing modes resonating at the same time, nested flux surfaces no longer exist due to their overlapping. Thus, the transport in RFPs is dominated by stochastic transport. Here a rather simple description of stochastic transport theory, considering *collisionless* plasmas, developed by Rechester and Rosembluth [20] is presented. The model describes the parallel transport in plasmas with destroyed magnetic surfaces due to many resonating modes.
First of all, the magnetic field is written as $\boldsymbol{B} = \boldsymbol{B}_z + \boldsymbol{B}_\theta + \delta\boldsymbol{B}$, with the perturbation part:

$$\delta\boldsymbol{B} = \sum_{m,n} \boldsymbol{b}_{m,n}(r) \exp[i(m\theta - nz/R)] \tag{2.9}$$

m and n are the wave numbers in poloidal and toroidal direction, respectively. The shape of magnetic surfaces described with each harmonics is the magnetic island, which has been discussed in the previous section.
When many modes resonate at the same time, magnetic surfaces conserve if the Poincaré plot on a poloidal cross-section shows smooth curves. Starting from one poloidal plane at a fixed toroidal angle and following one field line, if the intersec-

tions betw
the magn
distribute
Consider
the two ec
preserving
process. T
its shape
expressio
tion lengt
number m
called stoc
decrease i
process is

but because the width of the area becomes extraordinarily small, any small spreading due to motion perpendicular to the field lines can be of great importance as we will see later. The precise mathematics and all details can be found in a good review on the subject.[7]

Let us turn now to the subject of this Letter: electron heat transport in a braided magnetic field. We note parenthetically that mass transport will be limited by ambipolar potentials which we will not consider here.

Suppose that in some small region we mark instantaneously a number of electrons and then watch for the time evolution of their radial distribution. Since the radial spreading of test electrons is a Brownian process, the radial thermal conductivity will be given by $\chi_r = \langle(\Delta r)^2\rangle/2t$, where $\langle(\Delta r)^2\rangle$ is the mean square of the radial displacements of electrons during the time interval t. We will determine χ_r in two limits: "collisionless," when the collisional mean free path λ is bounded by $r^2 v/\chi_r \gg \lambda \gg L_c$, and collisional, when $\lambda \ll L_c$. [We will make a number of simplifying assumptions and not attempt to give detailed

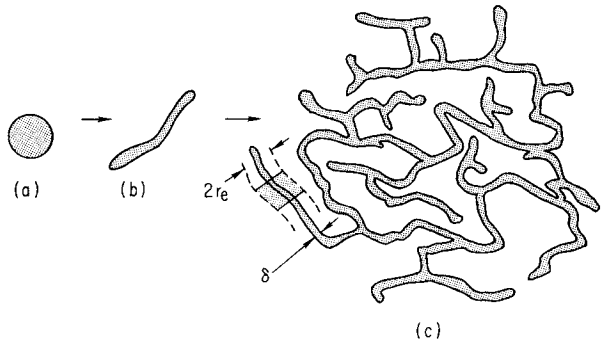

FIG. 1. The evolution of area mapping.

ally a distance r_e (or an electron
in the toroidal case). The latter
the perpendicular jump of the gui
the time of collision.

Let us start our experiment. I
a small circle of radius r_e. It m
liding a distance $\lambda = v\tau$ along the
ping into a complicated thin regio
drawn in Fig. 1(c), with the width
L_c). The average squared displa
ments in a radial direction is equ
$= 2D_{st}\lambda$. The collision now incre
this area to r_e. We can now cut
large number of small square pie
r_e and proceed in exactly the san
first step; see Fig. 1(c). Becaus
sionless case $r_e \gg \delta(\lambda)$, each of t
ments will evolve on the second s
dependently from its previous his
the spreading of our area in the
is similar to a random walk and
efficient is given by

$$\chi_r = \langle(\Delta r)^2\rangle/2\tau = D_{st} v .$$

This formula does not depend on
quency in spite of the importance
spreading.[10]

It is instructive to compare thi
similar evolution without any per
tion. Suppose that the particle r
rallel velocity after the first coll
second-step area will map exactl
initial small circle. Obviously,
it to expand in the radial directio
collisionally along the field line.
$t \gg \tau$, the average squared distan
particle in the z direction is $L^2 \approx$
introduced here the usual classic

Figure 2.4: A sketch of area mapping in multiple modes resonating magnetic field.

can be described as:

$$\left\langle(\delta r)^2\right\rangle = 2LD_{st} \tag{2.10}$$

L is the distance in the ζ direction with $L \gg L_{c0} = L_c \ln(rmr_0)$. D_{st} is given:

$$D_{st}(r) = \pi R \sum_{m,n} \frac{|b_{m,n}(r)|^2}{B_z^2} \delta\left(\frac{m}{g(r)} - n\right) \tag{2.11}$$

The function $g(r)$ describes the locations of resonant surfaces and it is equivalent to Equation 1.9.

Now consider the time evolution of electrons in a small region. Being a Brownian process, the radial spreading process has its thermal conductivity as $\chi_r = \langle(\Delta r)^2\rangle/2\tau$

with τ the time interval and Δr the radial displacement within this time interval. This is equivalent to *collisionless* condition, which brings us the thermal conductivity in radial direction:

$$\chi_r = \left\langle (\Delta r)^2 \right\rangle / 2\tau = 2LD_{st}/2\tau = D_{st}v \tag{2.12}$$

The thermal conductivity in a stochastic field is proportional to the ion thermal velocity $v = (2T_i/m_i)$ instead of the collision frequency. Also it is proportional to the sum of all the modes, which is shown in the expression of $D_{st}(r)$ above. The stochastic transport in RFPs are the dominant transport process due to the overlap of resonant modes. This mechanism has been studied and discussed in the study of thermal properties in Quasi-Single Helicity state on RFX-mod, presented in Chapter 4.

2.3 Three Dimensional Transport due to the Presence of Magnetic Islands

Transport theory deals with the particle and energy flow inside of the plasma and it is one of the critical point for thermal nuclear fusion. Transport phenomenon, depending on the direction of mass/energy flow, can be divided into parallel and perpendicular transport, with its direction respect to magnetic field. In toroidal configurations with preserved nested flux surfaces, perpendicular transport, although very small compared with parallel transport, is the one who plays an important role in plasma confinement properties. This is not valid in configurations where nested flux surfaces are broken. In this case, the field lines fill in the whole plasma volume and the 'radial' transport is dominated by the parallel one.
Confinement in toroidal magnetic configurations with nested flux surfaces strongly depends on the constrain of radial particle or energy transport across the magnetic surfaces. Field inhomogeneity is the fundamental reason for the radial transport within the framework of neoclassical transport theory. For tokamaks, the existence of nested flux surfaces indicates the kinetic quantiles are functions of the flux surface labels. Temperature and density on one flux surfaces can be considered constant due to very high parallel motion of charged particles. The transport study has been intensely carried out on 1.5 dimensional level due to the possession of toroidal symmetry. Here 1.5 dimensional means 2 dimensional (poloidal (θ) and radial (r) directions) quantities averaged over the magnetic flux surfaces. This simplification significantly reduced the calculation task because now the problem is simplified to one dimensional.

Despite of lacking axisymmetry, for stellarators, transport work has also been carried out on 1.5 dimensional level due to the possession of nested flux surfaces. And finally for RFPs, due to lack of nested flux surfaces, transport processes are dominated by stochastic transport.
In real magnetic configurations, however, the commonly existed magnetic islands, i.e., the resonant MHD tearing modes rises intrinsically three dimensional aspect of transport study. In tokamaks and stellarators, nested flux surfaces are distorted in vicinity of magnetic islands. This brings two main issues for transport study:

- No monotonic coordinate could be defined to describe the whole plasma volume. With presence of magnetic islands, there are two zeros in flux coordinate, one is the original magnetic axis and the second one is the center of magnetic islands.
- The distorted flux surfaces break the toroidal symmetry (tokamaks) or helical symmetry (stellarators), leading to non-closed banana orbit of trapped particles drifting outwards. This effect is essentially induced by the increase of toroidal viscosity and the consequence is that it increases the radial particle drifts.

This dissertation is focused on the transport study with the presence of magnetic islands. The thesis work has been carried on two toroidal configurations: RFX-mod and TJ-II. To be more specific, this work contains the following two parts:

- The first part is the thermal property study as well as transport study on three sub-states within Quasi-Single Helicity state (QSH) on RFPs. QSH state has been observed on all RFP devices under proper plasma conditions. It reveals a better confinement regime compared to multiple helicity state. The thermal structure with high electron temperature in QSH features a bean-shaped helical structure. There are three sub-states, named Double Axes (DAx), Single Helical Axis (SHAx_n) and SHAx_w with n and w indicating narrow and wide thermal structure. This part has been dedicated to the study of characterization on thermal properties of these three sub-states. A complete comparison between these three sub-states has been firstly studied. This part has been carried out on a selected database obtained from RFX-mod [22], the largest RFP devices on operation in Padova, Italy. The detailed results are presented in Chapter 4.
  The transport study on these three substates has been carried out to solve the multiple magnetic axis issue and for this purpose, a multi-domain scheme, dividing the whole plasma volume into three separated regions has been studied. Monotonic coordinate can be defined in each of the three separated regions and consequently, the transport equation can be solved in each region. The

interface between these three region is the so-called separatrix and it is the connection for solving the transport in the whole plasma volume. A routine named Multiple Axes Solver has been developed and benchmarked with code ASTRA. Preliminary transport study with the help of MAxS has also been performed. This part is presented in both Chapter 3 and 4.

- The second part has been carried on TJ-II [23], a stellarator device in CIEMAT, Madrid. This part is focused on the transport modification in the vicinity of magnetic islands, using the Neoclassical Toroidal Viscosity (NTV) developed by K. C. Shaing [24]. It has been reported that magnetic islands plays a role of transport barrier [25] and also it modifies the local electric field [26]. The original theory developed by K. C. Shaing is focused on the toroidal plasma viscosity induced by axisymmetry breaking effect due to the presence of magnetic islands in tokamaks. The same equations, with an *extra* geometry factor, are adopted due to the fact that the distortion effect induced by magnetic islands is similar in tokamaks and stellarators. The geometry factor is applied because that the non-ambipolar fluxes in stellarators are much higher than in tokamaks. A general description on the theory of NTV is presented in Chapter 5. The application of this theory on TJ-II plasmas has been carried out. The detailed results and discussions are presented in Chapter 6.

Part II

Thermal Properties and Transport Study on Three Sub-states in QSH

3

Quasi-Single Helicity and Multiple Domain Scheme

Quasi-Single Helicity state has been observed on RFX-mod firstly and confirmed by other RFP devices afterwards. It shows a better confinement regime compared with multiple helicity state. This chapter presents the description of QSH state as well as its three sub-states. Moreover, the tool for transport study in multiple magnetic axes situations has also been developed and tested, based on the concept of multiple domain scheme, which is also presented.

3.1 Multiple Helicity and Quasi-Single Helicity

In RFX discharges with low plasma current $I_P < 1MA$, due to unique safety factor profile $q < 1$, many MHD modes saturated intrinsically, producing superposing magnetic islands and giving rise to a chaotic magnetic field in the plasma core. This chaotic magnetic field leads to high transport in the center with very limited confinement properties. Indeed, the electron temperature in such states shows a flat profile with low amplitude in the center and this is named as Multiple Helicity (MH) state. On the other hand, the nonlinear interactions between these modes gives rise a part in Ohm's law acting as effective electric field, via the average interactions between velocity and field pertubation $\left\langle \tilde{\boldsymbol{v}} \times \tilde{\boldsymbol{b}} \right\rangle$. This is called dynamo mechanism mentioned in Chapter 3. Compared with other fusion devices like tokamaks, RPFs in MH states shows a big gap due to the bad plasma confinement properties.
Nevertheless, it has been theoretically predicated with 3-dimensional MHD simulations [27, 28] that one single helical mode could sustain the dynamo effect and this state is named Single Helicity state (SH). This shows a promising future for RFPs in fusion research since nested flux surfaces are preserved inside of the single helical mode and radial transport could be significantly reduced compared with MH state. Experimentally, however, SH state has never been observed while an intermediate state, with enhanced plasma confinement properties has been observed in RFX-mod and further been confirmed on all RFP machines[29, 30]. This new regime which appears periodically in the high plasma current discharges ($I_P > 1MA$ in RFX-mod) is Quasi-Single Helical (QSH) state, with active control of radial magnetic perturbations [22, 31]. A typical discharge with $I_P > 1MA$ in RFX-mod is shown in Figure

3.1. The upper graph is the time evolution of the plasma current and the lower one is the time evolution of the toroidal magnetic tearing mode spectrum in which the red line represents the m=1, n=-7 mode, whose amplitude dominants the spectrum periodically during the discharge and the blue line represents the rest of the modes (secondary modes) defined as $b_{sec} = \left[\sum_{n=-8}^{-17}(b_\phi^{1,n})^2\right]^{1/2}$ (in this thesis the toroidal mode number -8:-17 is used). The duration time of one cycle increases with the increase of the plasma current [32]. A typical mode spectrum of both QSH and MH are presented in Figure 3.2. One could see that modes shows a comparable amplitude in MH w[illegible]

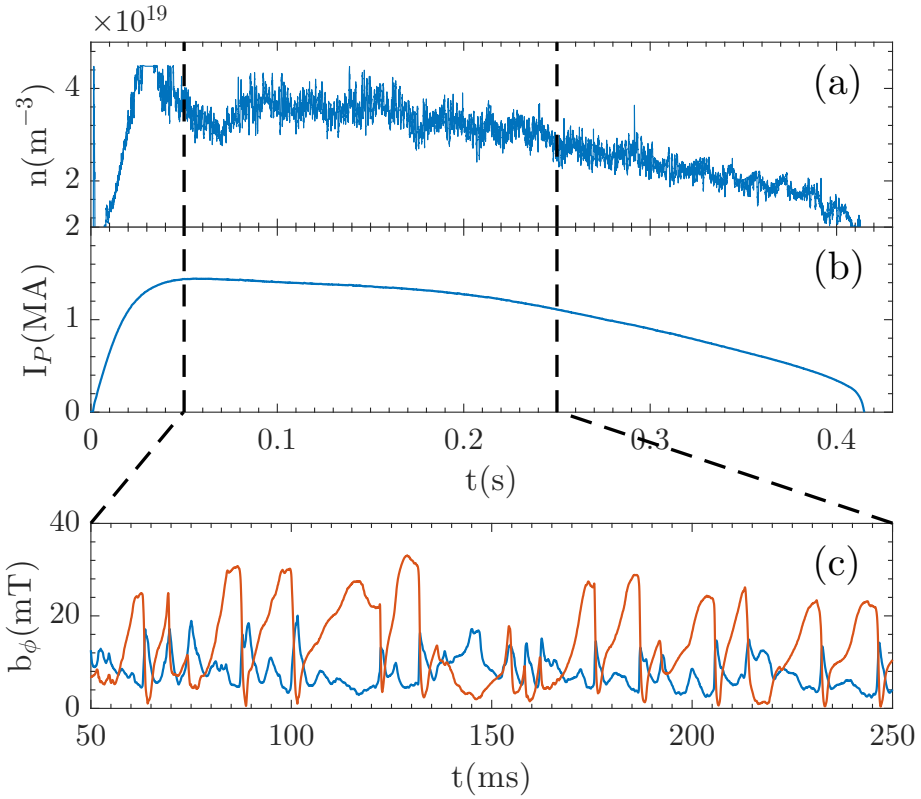

Figure 3.1: A typical discharge in RFX-mod. (a): plasma density. (b): plasma current. (c): The time evolution of toroidal magnetic component b_ϕ with red line representing the dominant mode (m=1,n=-7) and the blue line representing the secondary modes (m=1, n=8:17).

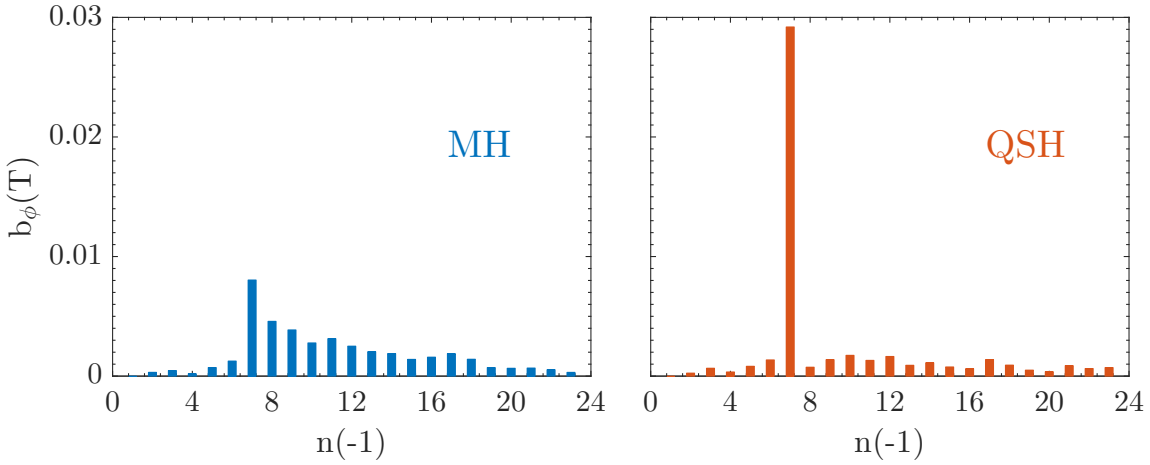

Figure 3.2: Typical toroidal field b_ϕ spectra (2ms averaged value) for m=1 mode against the toroidal mode number n. The blue spectrum is for MH state and the red one is for QSH state.

3.2 Three Sub-States in QSH

There are three sub-states in one cycle of QSH state. One cycle of QSH begins with the most inner mode starting to grow, while the rest of the modes remains at a low amplitude, forming one dominant magnetic island with a separatrix. A bean-shaped thermal structure with narrow, off-axis electron temperature structure spontaneously formed in the island center. This first stage is named Double Axes state (DAx) in the sense that there are two magnetic axes existing at the same time. Afterwards, the dominant mode grows further, reaching the threshold on which a magnetic topological transition takes place: the X point of the dominant mode anneals with the original magnetic axis and the O point of the dominant mode survives as the new magnetic axis. During this process, the bean-shaped thermal structure remains relatively unchanged: narrow and off-axis. This is the second stage and it is named Single Helical Axis state (SHAx_n) with the subscribe n meaning narrow thermal structure. When the dominant mode grows up to 4% of the edge magnetic field, the high electron temperature structure usually evolves from off-axis in SHAx_n into a wider profile enclosing the geometrical axis. This third sub-state is named as SHAX_w state with the subscribe w indicating wide thermal structure. The three sub-states of QSH are shown in Figure 3.3. The lower three figures d, e, f, are electron temperature profiles measured with an 84-point Thomson scattering diagnostic [5] in each sub-state. The upper three figures a, b, c, are the corresponding

T_e contour plots, calculated with the magnetic equilibrium reconstruction produced by the code SHEq [33], thanks to the fact that temperature, in QSH states, is a flux function [31]. Both DAx and SHAx_n feature narrow and off-axis T_e thermal structure. The SHAx_w, on the other hand, has a wide thermal structure in the plasma core.
The transition from MH to QSH features a bean-shaped thermal structure with high electron temperature forming in the center of the plasma sustained by the existence of the so-called electron internal transport barrier (eITB)[34] with significantly low thermal diffusivity. This critical region should be studied in order to understand the physics of QSH states. Accompanied with the thermal evolution, MHD modes also shows an interesting evolution, partially in their amplitude. A thermal gradient study as well as a preliminary transport study, based on 208 selected electron temperature profiles obtained from Thomson scattering has been performed to understand the role of dominant mode and secondary modes in the time evolution of 3 sub-states in QSH and the results are shown in the following chapter.

3.3 Multiple Domain Scheme

Transport research benefits of the availability of several well-developed 1.5D transport codes, which have been widely used in single axis magnetic configuration for decades while it is beyond their capability to treat situations with the presence of magnetic islands due to the fact that it is impossible to find a monotonic coordinate to describe the whole plasma volume. Indeed, in plasma configurations with multi-axes, a monotonic radial coordinate is undefinable in the whole plasma volume, which, together with the correct metrics (the spatial derivative of the volume and the first element of the metric tensor, denoted as V' and G_1, respectively), are essential to solve the transport equations:

$$\frac{3}{2} n_e \frac{\partial T_e}{\partial t} + \frac{1}{V'} \frac{\partial \Gamma_e}{\partial \rho} = S_e \tag{3.1}$$

where n_e and T_e are the electron density and temperature, $\Gamma_e = -V' G_1 n_e \chi \partial T_e / \partial \rho$ is the energy flux, χ is the thermal diffusivity and S_e is the energy source.
Facing this issue, a new approach, named Multiple Axes Solver (MAxS), capable of studying transport under multi-axis configuration is developed and tested on RFX-mod. Figure 3.4 shows a sketch of a poloidal cross-section of a magnetic field with the presence of a magnetic island. The 3 regions are: Region I, the circular plasma containing the original magnetic axis; Region II, the magnetic island containing its

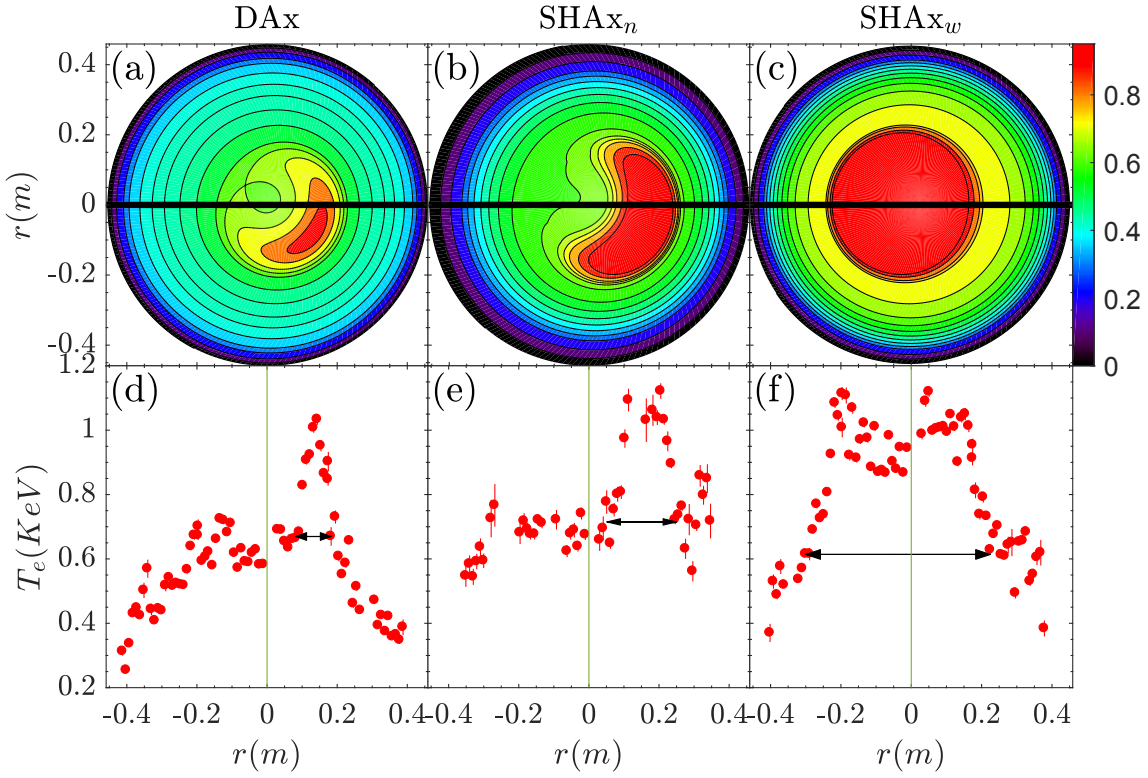

Figure 3.3: Three sub-states: (a) DAx, (b) SHAx$_n$ and (c) SHAX$_w$ are presented. The black horizontal lines in the contour plots represents the Thomson scattering laser path and ones in the lower 3 plots are the width of the thermal structure.

own axis and Region III, the outer region in the plasma edge. The red line represents the separatrix, which is a thin layer around the magnetic island and it features high stochasticity. In each of the 3 zones, monotonic coordinate ρ could be well defined and the temperature could also be considered as a function of ρ in each zone, which will be demonstrated later. The separatrix region is the interface between the three zones, which has very small volume compared with the three zones. Hence, there is assumed to be no heat source nor sink in the separatrix region. What is more, due to the stochastic property of the separatrix, the transport is high so that the electron temperature is uniform everywhere inside of the separatrix. The main steps for MAxS are:

- Make initial 'guess' for thermal diffusivity χ in each zones and set the proper boundary conditions.

- Evolve transport equations in three zones until the temperature profiles remains unchanged. Then get the fluxes from three zones, namely Γ_I, Γ_{II} and Γ_{III}.
- These fluxes enters into separatrix and evolve according to $\partial T_{sep}/\partial t = (2/3n_e)[(\Gamma_I + \Gamma_{II} + \Gamma_{III})/V_{sep}]$.
- If $\partial T_{sep}/\partial t \leq 10^3 eV/s$ then break. The consequente χ profiles are the ones we are seeking.
- If $\partial T_{sep}/\partial t \leq 10^3 eV/s$ then go back to step 2, adjusting the χ profile via the genetic algorithm.

The chart flow of code MAxS is presented in Figure 3.5.

MAxS have been developed and benchmarked with a well know 1.5 dimensional

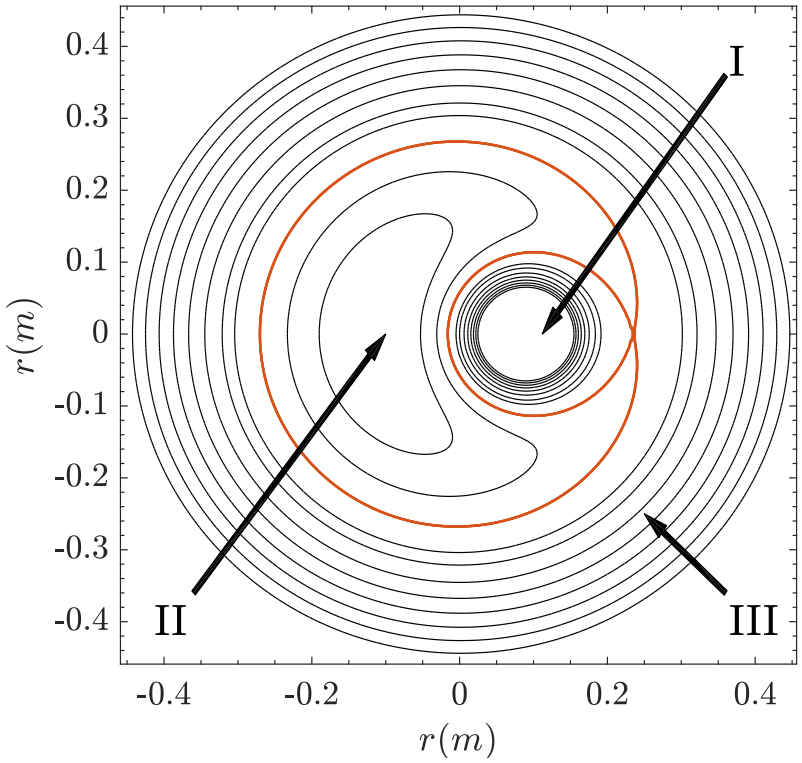

Figure 3.4: A sketch of poloidal cross section of a magnetic field with the presence of a magnetic island. The red line represents the separatrix.

transport code ASTRA [35]. The benchmark has been carried based on two SHAx$_n$

the volume of the cell containing the separatrix;

- the calculated T_{sep} is the new boundary condition for the next step of transport equation integration.

The simulation run until the balancing of the thermal fluxes in the separatrix region is achieved and the separatrix temperature becomes stationary (convergence to stationary solution). In case of evolutive simulation, there are no convergence criteria and the simulation ends after a prescribed number of time steps.

The flow chart of MAxS is:

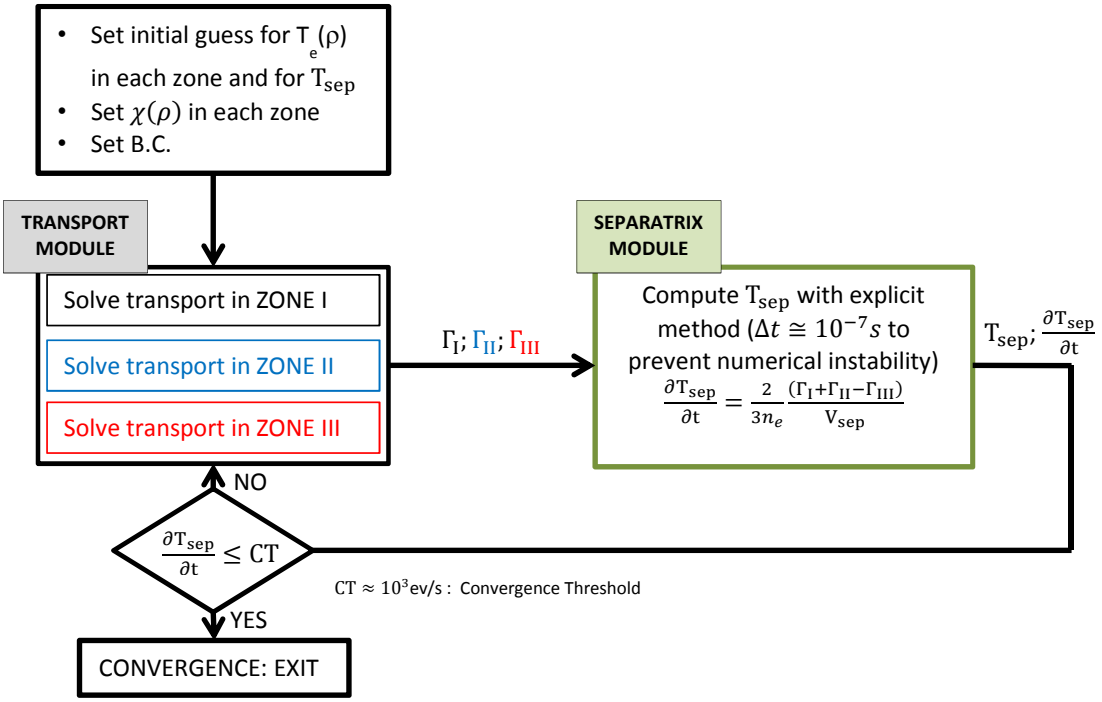

Figure 3.5: Flow chart of code MAxS.

Introduction.

An electron heat transport simulation has been performed with MAxS on LHD in presence of magnetic islands.

To run the simulation, MAxS needs a minimum set of input data for each plasma zone:

- Metrics:
  - monotonic radial coordinate ρ
  - $g_1 = \nabla\rho \cdot \nabla\rho$
  - $V' = \frac{dV}{d\rho}$
- Kinetic profiles:
  - $n_e(\rho)$

cases obtained in RFX-mod. The quantities ρ, $T_e(\rho)$, V' and G_1 are provided by code SHEq. The main principle is to let these two codes to find the best thermal diffusivity profile which promises the best fit between simulated and real electron temperature profile. For MAxS, the selection of χ profile is done by hand while for ASTRA, it is done automatically using Genetic Algorithm, which is implemented in RFX, generates a serials of "best choices", also named confidence interval (CI's). The result of benchmark between these two codes is shown in Figure 3.6. The upper graphs are the two electron temperature profiles from experiment (blue stars), best fit solution from MAxS (red solid line) and the CI's from ASTRA (gray shadow). The lower two graphs are the corresponding thermal diffusivity profiles from MAxS (red solid line) and from ASTRA (gray shadow). The result shows a good agreement in both the electron temperature profiles and the thermal diffusivity profiles between MAxS and ASTRA, which gives confidence for MAxS to perform further transport study. Moreover, the Genetic Algorithm has also been implemented into MAxS for further work.

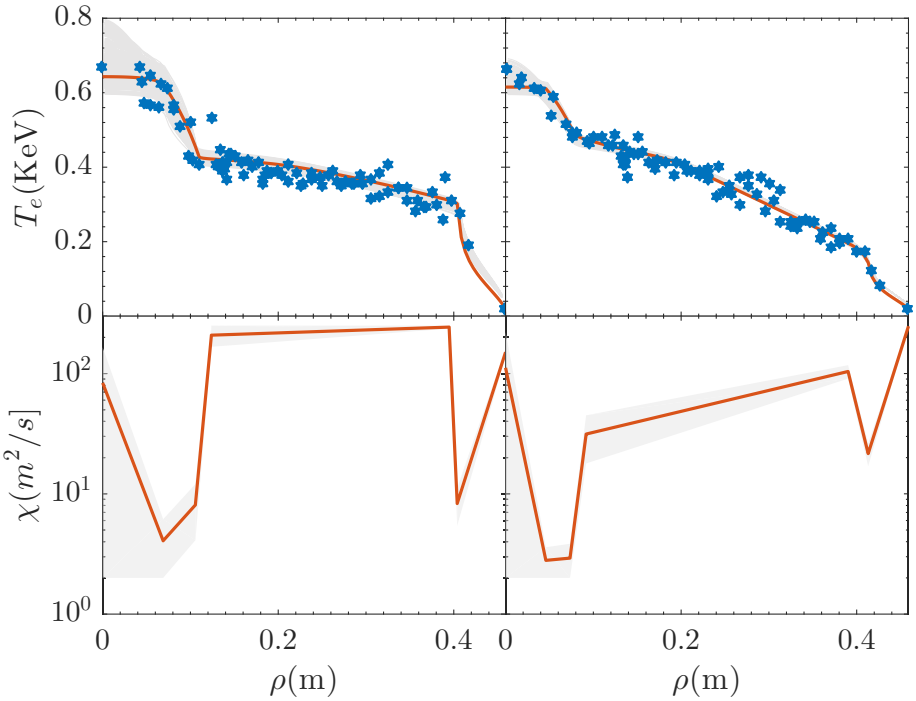

Figure 3.6: Benchmark between MAxS and ASTRA applying two SHAx$_n$ cases in RFX-mod. The upper figures are the electron temperature profiles (green stars) from Thomson scattering and the simulated electron temperature profile from MAxS (red line). The gray shadow is the acceptable range obtained from ASTRA.

3.4 Flux Coordinate

The coordinate system adopted by MAxS is the radial flux coordinate.The equilibrium quantities and the eigenfunctions are obtained solving the force balance equation in toroidal geometry with a perturbative approach. The basic equations are:

$$\nabla \cdot \boldsymbol{B} = 0 \qquad \nabla \times \boldsymbol{B} = \mu_0 \boldsymbol{J} \qquad \boldsymbol{J} \times \boldsymbol{B} = \nabla P = 0 \tag{3.2}$$

A physical quantity ξ could be written as the equilibrium part plus the perturbation: $\xi(r,\theta,\phi) = \xi_0(r) + \xi_1(r)$ where $\xi_0 \gg \xi_1$. By taking the Fourier analysis on the pertubation ξ_1, one have:

$$\xi(r,\theta,\phi) = \xi_0(r) + \sum_{m,n} |\xi_1^{m,n}| \exp i(m\theta - n\phi) \tag{3.3}$$

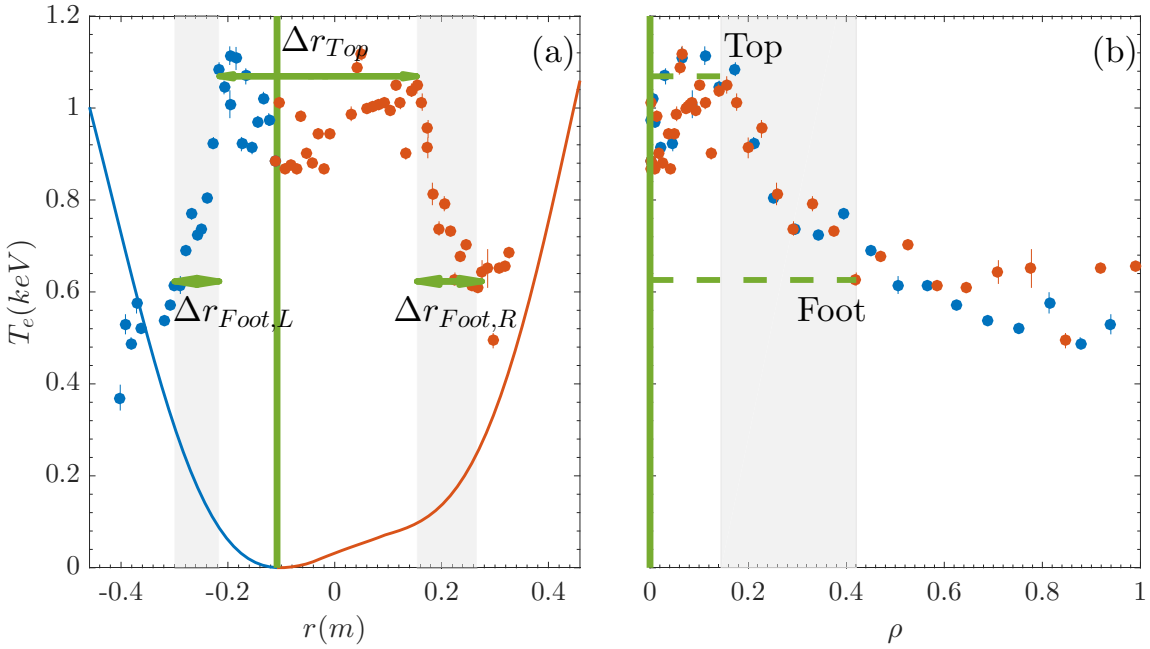

Figure 3.7: (a) A typical electron temperature from SHAx$_w$ state as a function of the radius is presented using the symbol of dot while the solid line represents the normalized helical flux function ρ.(b) The same electron temperature profile as in (a), presented as a function of ρ with two colors representing the two sides between the ρ_{min}. The green dash line represents the location and T_e value for the top and foot of the eITB, which is obtained from TeGrA routine.

Write quantities in forms of Equation 3.3 and substitute into Equation 3.2, a set of partial differential equations is obtained, with boundary conditions from experimental data.

The next step is to map electron temperature over the flux surfaces, under the assumption that the kinetic quantity, such as electron temperature, is a monotonic function of the helical flux in one axis condition. A typical electron temperature profile, measured in SHAx$_w$ state is presented in Figure 3.7(a), as a function of the radius r. There is one flat region with high electron temperature in the core and on both sides of the flat region, there are two temperature gradients, marked as the gray shadow which are eITB regions. The width of the eITB is denoted as $\Delta r_{Foot,R(L)}$ with subscript $Foot$ meaning the foot of the gradient and $R(L)$ meaning the two regions located in the right and left side. The width of the flat top is denoted as Δr_{Top}, which is also shown in Figure 3.7(a). The T_e profile is split into two parts,

marked as blue and red, by a vertical green line which corresponds to the minimum value of the square root of the normalized helical flux $\rho = \sqrt{\Phi/\Phi_0}$ where Φ is the helical flux defined as $\Phi = m\Psi_0 - nF_0 + m\psi^{m,n} - nf^{m,n}$ with m,n the poloidal and toroidal mode number, Ψ_0, F_0 are the equilibrium poloidal and toroidal magnetic flux. The ψ, f are the poloidal and toroidal magnetic flux of the dominant mode. Φ_0 is the helical flux on the plasma edge [33]. Using ρ as a new radial coordinate, the result of T_e remapping along ρ shown in Figure 3.7(b) indicates the kinetic quantity T_e can be described as a function of the normalized helical flux. Figure 3.8 shows results of a remapping done in a DAx case, in which both the core region and the island region are detected by Thomson scattering system.

- (a). Contour plot of the helical flux at Thomson scattering angle, with the thick red curve representing the separatrix. There are four intersections between the separatrix and mid plan ($\theta = 0$) and their locations are marked with four dashed black vertical lines. The three vertical lines represents the location of maximum or minimum of the helical flux, red for magnetic island region and blue for the core region.

- (b). The normalized helical flux ρ is plotted versus the geometrical redius. There are two separated island regions detected by Thomson scattering, shown as the two red curves, together with one core region, marked as blue. The two black curves are the outer regions. The horizontal black line represents the sepatratrix. The four vertical dashed black lines are the corresponding intersections shown in graph a.

- (c). The electron temperature, measured by Thomson scattering diagnostic, is plotted versus the geometrical radius. The red color indicates the island region, the blue color indicates the core region and the black color indicates the outer region.

- (d). Remapped electron temperature in island region is plotted versus ρ. The remapping is to build the relations between T_e and ρ, through the information of the radial distribution. The pink color represents the right side and the green color represents the left side.
  (e). The remapped electron temperature in the core region.
  (f). The remapped electron temperature in the outer region.

The minimum helical flux doesn't reach value zero is due to the face that the Thomson scattering laser did detect, in fact most of the cases it cannot, the island center. This brings the fact that the electron temperature measured cannot show the whole

structure. Nonetheless, the information of the thermal gradient can be, at least partially reflected via the T_e profiles obtained. Meanwhile, most of the T_e points measured in experiments are in outer region. This leads to the problem that the points in island region sometimes are not enough to perform an automatic algorithm for gradient analysis in flux coordinate. Hence, the thermal properties are, in the following chapter, performed and discussed in the geometrical coordinate.

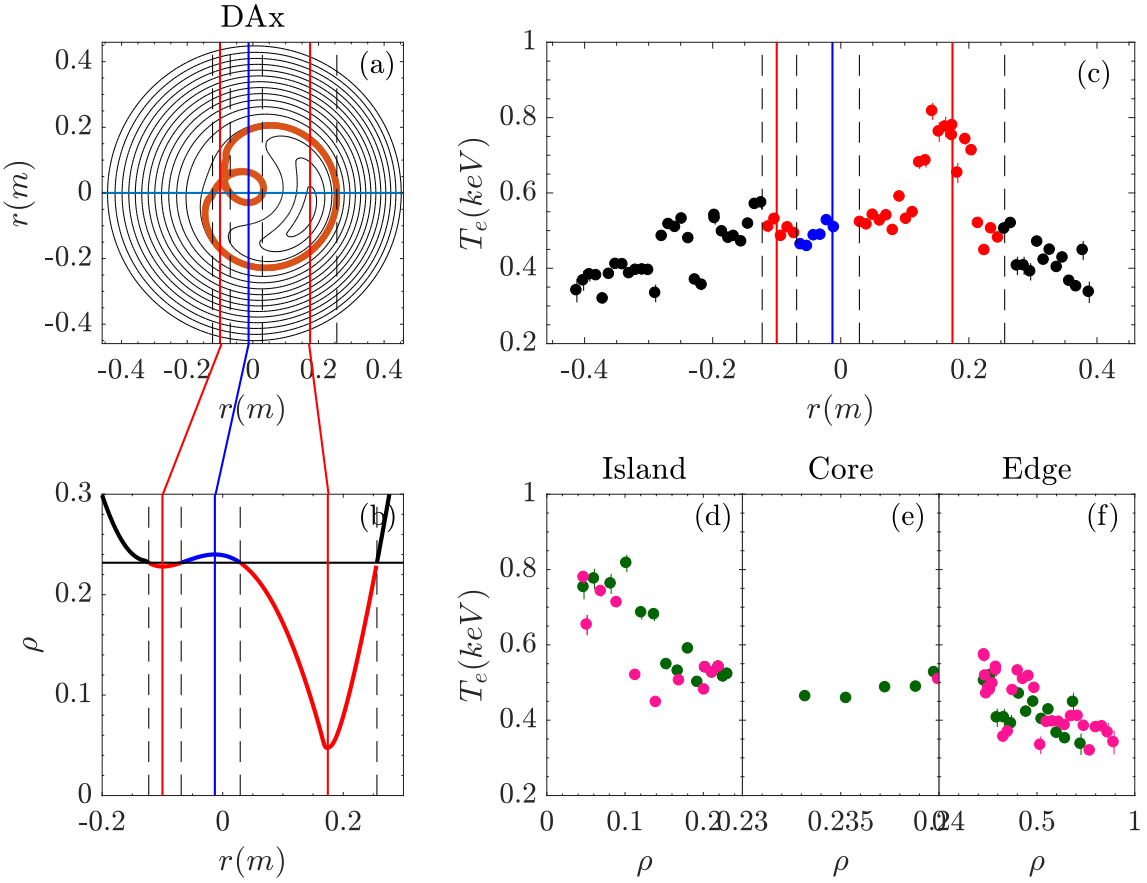

Figure 3.8: Electron temperature remapped on the flux surfaces in a DAx state. Vertical dashed black lines represent the location of separatrix intersected by mid plan at Thomson scattering angle $\phi = 82.5°$. The vertical thin lines represents the local maximum or minimum of the helical flux (red for island region and blue for the core region). (a). Contour plot for the helical flux on the poloidal cross-section at Thomson scattering toroidal angle. The horizontal line represents the Thomson scattering laser path and the thick red curve represents the separatrix. (b). The normalized helical flux plotted versus the geometrical radial, zoomed at the island region. The horizontal line represents the separatrix, intersected with the curve with four intersections, marked with the dashed black line. There are two parts belongs to magnetic island, marked with red. The blue part is the core region and the two black part on both side of the profile represents the outer region. (c). The Thomson scattering profile versus radius of vacuum vessel. The colors represents different regions. (d), (e) ,(f). The results of remapping in island (d), core (e) and outer region (f). The pink represents left side and the green represents the right side.

4 Thermal Properties of Three sub-states in QSH state

The Quasi-Single Helicity state has shown a better confinement regime compared with multiple helicity state. Here the thermal properties, with the help of a routine named TeGrA, as well as the preliminary energy transport, with the help of MAxS, study are presented. The behavior of thermal gradients respect to both dominant and secondary modes are presented and discussed within the framework of stochastic transport theory. In the end, the energy confinement time is evaluated within these three sub-states.

4.1 Thermal Gradient Analysis

This chapter presents the study on the thermal properties of three sub-states in QSH. The work is based on a selected database contains 208 electron temperature profiles obtained from Thomson scattering diagnostic in QSH state whose signal path lies in the middle plane at the poloidal angle $\theta = 0°$ and toroidal angle $\phi = 82.5°$. The angle between the Thomson scattering laser path and the line going through the maximum thermal width is between -35° and 35° in order to be sure to not miss the highest temperature region in the plasma. The database was further selected based on the density range from 2.5 to 3.5 with unit of $10^{19}m^{-3}$ and the plasma current varies from 1.2MA to 1.5MA.
A gradient automatic analysis (TeGrA) routine, capable of extracting the positions as well as T_e value of the foots and tops of the eITB, has been developed. The TeGrA routine, in general, has the same procedure for all the T_e profiles with minor differences between peaked T_e profile and flat ones. TeGrA is based on the principle that the left and right of the eITB foot should share the same T_e value, which is equivalent to the assumption that T_e is a function of ρ. The basic algorithm for TeGrA are:

- Get the original $T_e(r)$ profile.
- Get the mean value of the $T_e(r)$ profile, T_e^M.
- For top analysis, update the $T_e(r)$ profile with $T_e(r) > (1 - x_1)T_e^M$ with $0 < x_1 < 1$, a parameter to be decided based on the profiles.

- Repeat step 2 on the updated $T_e(r)$ profile until the value of T_e^M doesn't change anymore and the final value of T_e^M is the value of $T_e(top)$ with its corresponding value of r being the $r(top)$.

For foot analysis, similar steps are applied with a difference in step 2 which is $Te < (1 + x_2)T_e^M$, where $x_2 > 1$. The main steps of routine TeGrA are shown in Figure 4.1.

Applying TeGrA routine on the selected database, the *absolute value* for left and right gradients of the electron temperature could be easily obtained, denoted as ∇T_e^L and ∇T_e^R. The minimum values of the two gradients are shown in Figure 4.2, as a function of the toroidal component of the dominant mode $b_\phi^{1,-7}$ normalized to the edge magnetic field $B(a)$. The error bar is estimated as follows:

$$\delta\nabla T_e/\nabla T_e = \sqrt{\sum(\delta T_e/T_e)^2 + \sum(\delta r/r)^2} \tag{4.1}$$

Where δT_e and δr are the error of electron temperature and the corresponding radial errors obtained from experiments. There are two clear points of transition between substates: the first one is between DAx and SHAx_n states when the normalized dominant mode $b_\phi^{1,-7}/B(a) \approx 2\%$, and the second one is between SHAx_n and SHAx_w where $b_\phi^{1,-7}/B(a) \approx 4\%$. Furthermore, with the increase of the normalized dominant mode, the minimum temperature gradient decreases. This result might give us a hint of a local increase of energy transport and this might play a role in energy confinement time behavior and this is confirmed by the priliminary transport study results using MAxS, which is shown in Figure 4.3. Indeed, with the increase of the dominant mode, the minimum thermal diffusivity χ increases. Here it is worth mentioning that in Ref [36], a thermal gradient oscillation has been observed below 2 keV/m around $b_\phi^{1,-7}/B(a) \approx 4\%$ on the flat top of one QSH cycle. This result is agreed with Figure 4.2, in which there are both SHAx_n and SHAx_w around $b_\phi^{1,-7}/B(a) \approx 4\%$.

Moreover, the evolution of the thermal structures is also studied. The width of the thermal structure, $W_{Te} = \Delta r_{Top} + \Delta r_{Foot,R} + \Delta r_{Foot,L}$, has been reported a sudden change from SHAx_n to SHAx_w in Ref [37]. Here we look into the evolution of Δr_{Foot} and Δr_{top} separately. The minimum value between $\Delta r_{Foot,L}$ and $\Delta r_{Foot,R}$, Δr_{Foot}^m, shows a continuous increase from DAx to $\text{SHAx}_{n,w}$ as a function of the normalized dominant mode. This is shown as empty symbols in Figure 4.4. Δr_{Top} shows a sudden jump in its amplitude (solid symbols in Figure 4.4) from SHAx_n to SHAx_w. This indicates that the sudden jump in W_{T_e} reported in Ref [37] is due to the growth of the top region in T_e profile rather than the gradient width Δr_{Foot}.
Finally, the value of $T_{e,Top}$, $T_{e,Foot}$ and $\Delta T_e = T_{e,top} - T_{e,Foot}$ are calculated and shown in Figure 4.5. The value of $T_{e,Foot}$ slightly decreases within these three states. An

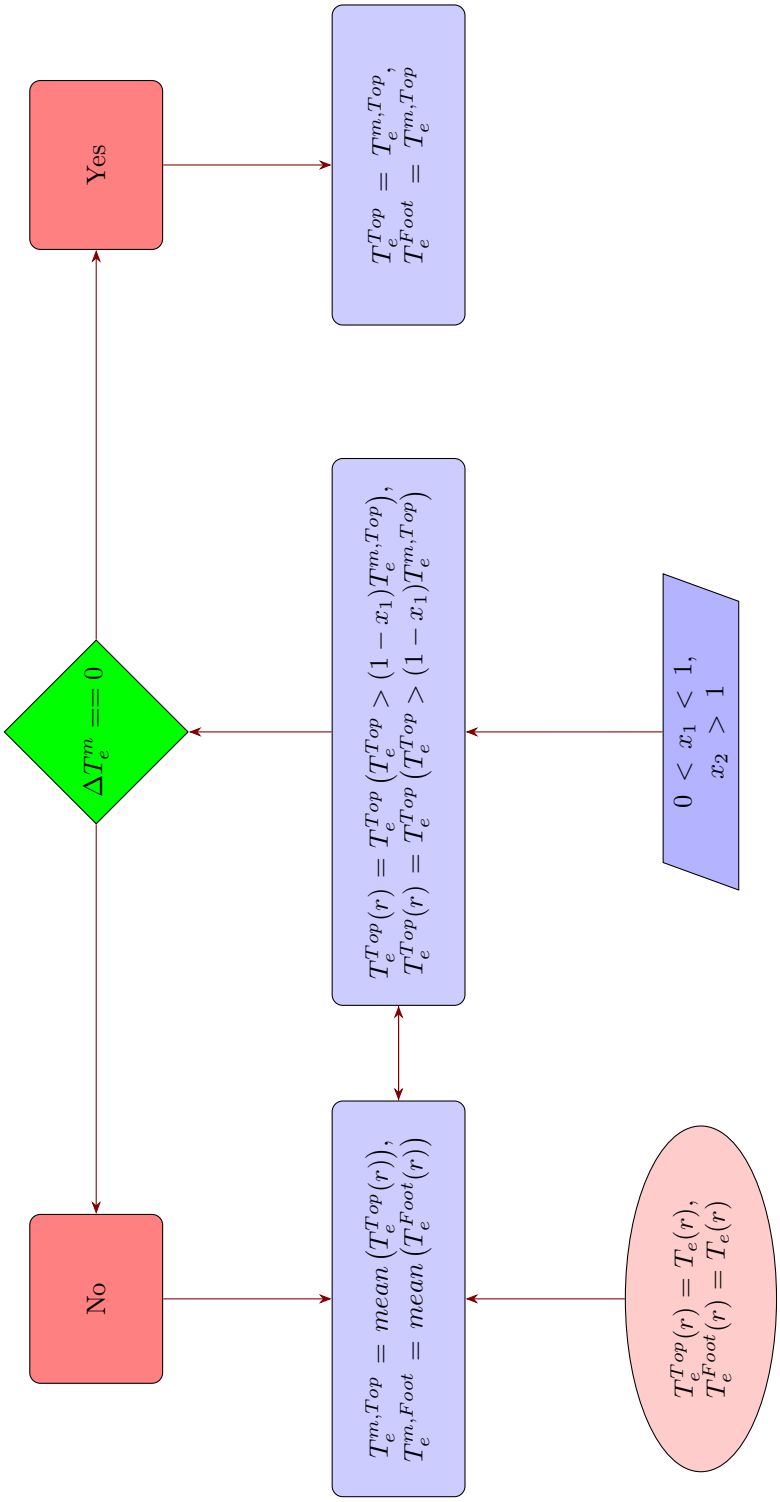

Figure 4.1: The main steps for routine TeGrA.

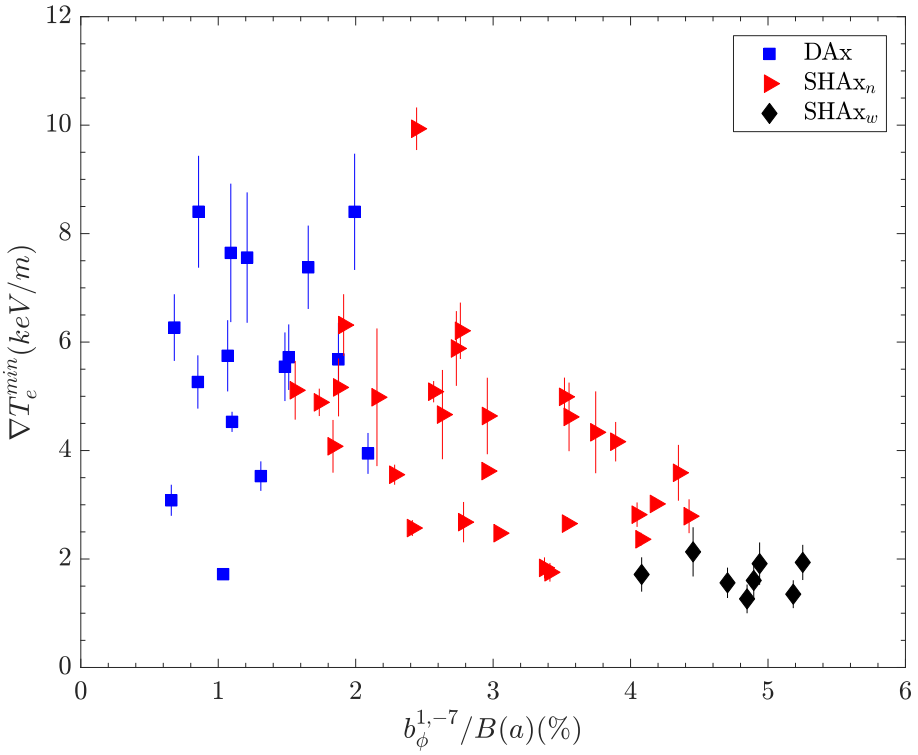

Figure 4.2: The minimum temperature ∇T_e^{min} between ∇T_e^L and ∇T_e^R is presented as a function of the dominant mode normalized by the edge magnetic field.

explanation is that the foot of the gradient is expanding towards outer region where electron temperature is lower. The top value, however, shows an increase trend from DAx to SHAx$_n$ and decreases in SHAx$_w$. Consequently, the value ΔT_e slightly increases from DAx to SHAx$_n$ and then decreases in SHAx$_w$.

The results shown above confirmed that the thermal structure enlarges within these three sub-states as the dominant mode increases. However, the thermal gradient decreases as the dominant mode increases. In order to check if this peculiar thermal gradient behavior is related to the stochastic transport in RFPs, we investigated the behavior of secondary modes, defined as $b_{sec} = \left(\sum_{n=-8:-17} b_{1,n}^2\right)^{1/2}$. Figure 4.6 shows the minimum gradient versus the secondary modes normalized to the edge field. The plot shows a clear separation between the group of SHAx$_n$ and DAx structures, that occurs when the secondary modes are higher than 0.85%, and the SHAx$_w$, that occurs when the secondary modes is lower than 0.85%. In DAx and SHAx$_n$ group, the thermal gradient tends to increase with the decrease of the secondary modes. This

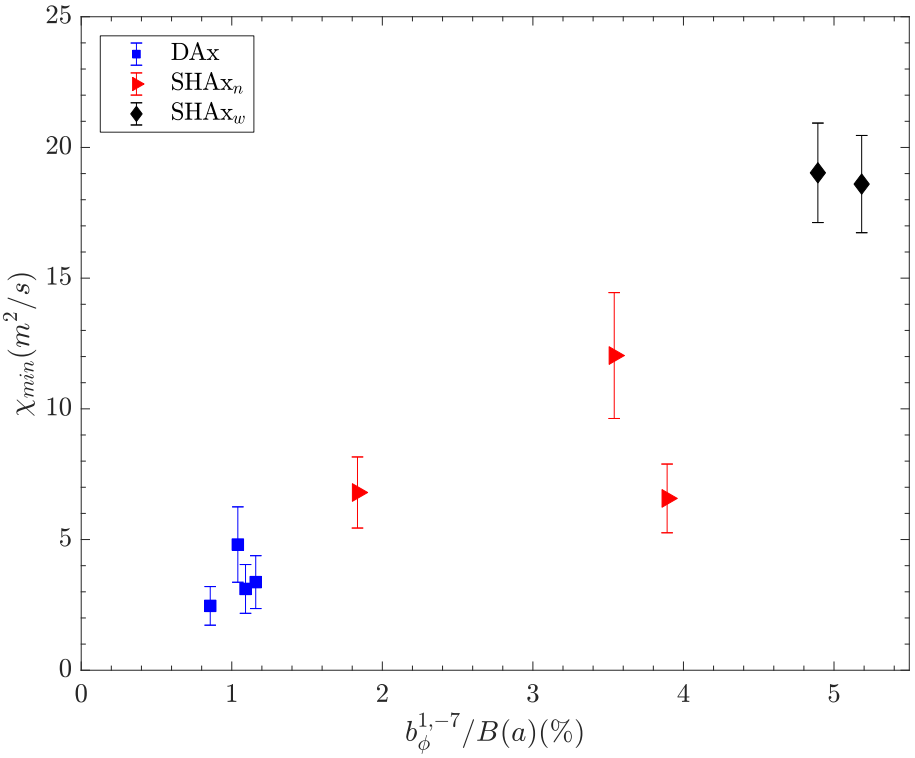

Figure 4.3: Preliminary results of transport study is presented.

trend agrees with stochastic transport in RFP plasmas. The steepness of the gradient suddenly decreases in the SHAx$_w$ group. Such last behavior can be understood in the light of the analyses presented in Ref [37]. In such paper it is shown that the transition from narrow to wide thermal structures is related to the stabilization of the subdominant, m=1, n=-8,-9 modes, whose amplitude is significantly reduced in SHAx$_w$ state. In particular the m=1, n=-8 mode, which usually is the highest among secondary modes, in such states becomes comparable to higher n modes. The widening of structures is then attributed to the decrease of stochasticity produced by such two modes, which allows the region enclosed by the resonance radii, where the temperature is usually flat due to the high transport, to host the eITB gradients. This conclusion is supported by the result that, while the DAx and SHAx$_n$ gradients form internally to the m=-1, n=-8 mode resonance radius, SHAx$_w$ gradients form between m=-1, n=-8,-9 mode resonance radii. Since the SHAx$_w$ gradients develop more externally than the others, they are supposed to be more sensible to the field stochastization produced by higher n modes, being near to their resonance radii.

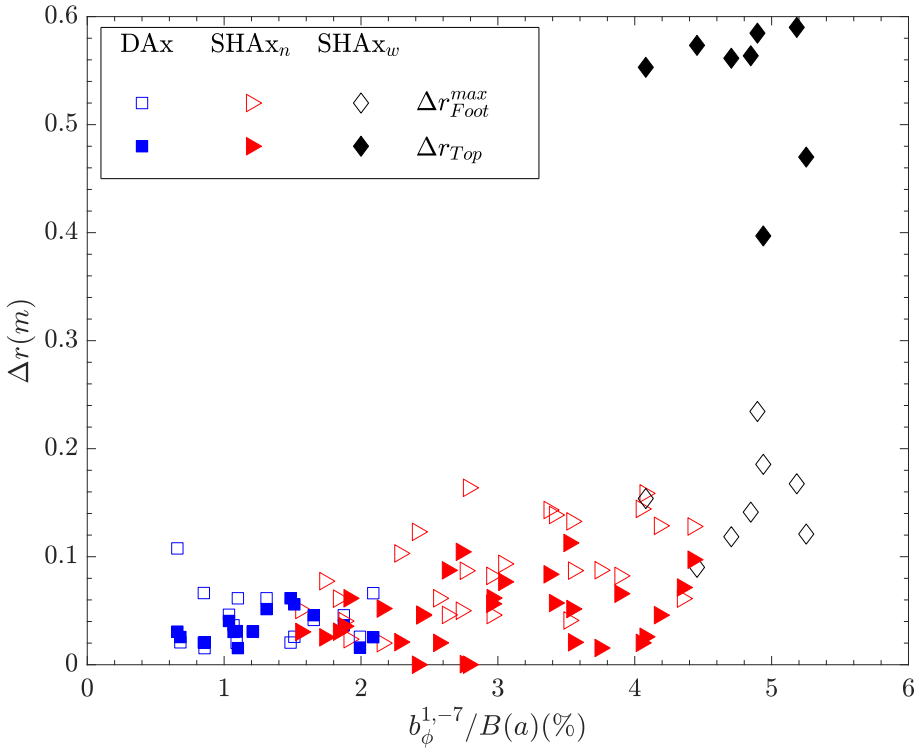

Figure 4.4: The maximum value of the gradient width Δr_{Foot}^{max} (empty symbols) and Δr_{Top} (solid symbols) plotted as a function of the normalized dominant mode. The foot shows a continuous growth while there is a sudden jump between SHAx$_n$ and SHAx$_w$.

This last element could explain why such gradients are less steep than the DAx and SHAx$_n$ ones although the secondary modes are the lowest ones.
So far we know that both dominant mode and secondary modes play a role in setting thermal gradient in eITB region. In both DAx and SHAx$_n$ groups, the thermal gradients are, on certain levels, negatively correlated with both dominant mode and secondary modes. While in SHAx$_w$ group, the thermal gradients does not share the same behavior pattern. Now we investigate the weight of setting thermal gradients due to dominant mode and secondary modes, which is shown in Figure 4.7. In DAx state, thermal gradients show an increase trend with decrease of the ratio $b_{sec}/b_\phi^{1,-7}$ while in both SHAx$_n$ and SHAx$_w$, the thermal gradients are positively correlated with the value of $b_{sec}/b_\phi^{1,-7}$. This result could be explained by the stochastic reduction by separatrix. In DAx state where there is separatrix, the thermal gradients are

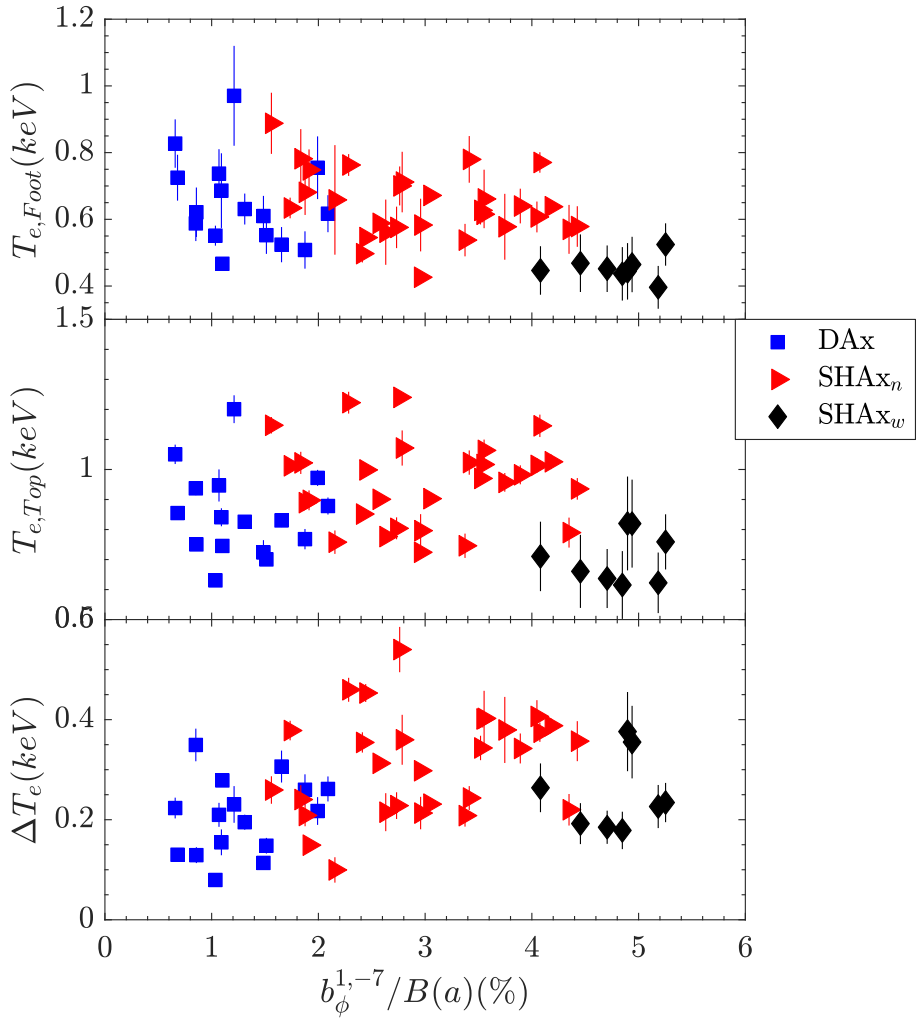

Figure 4.5: The top and foot value of T_e and the difference ΔT_e are shown as a function of the normalized dominant mode.

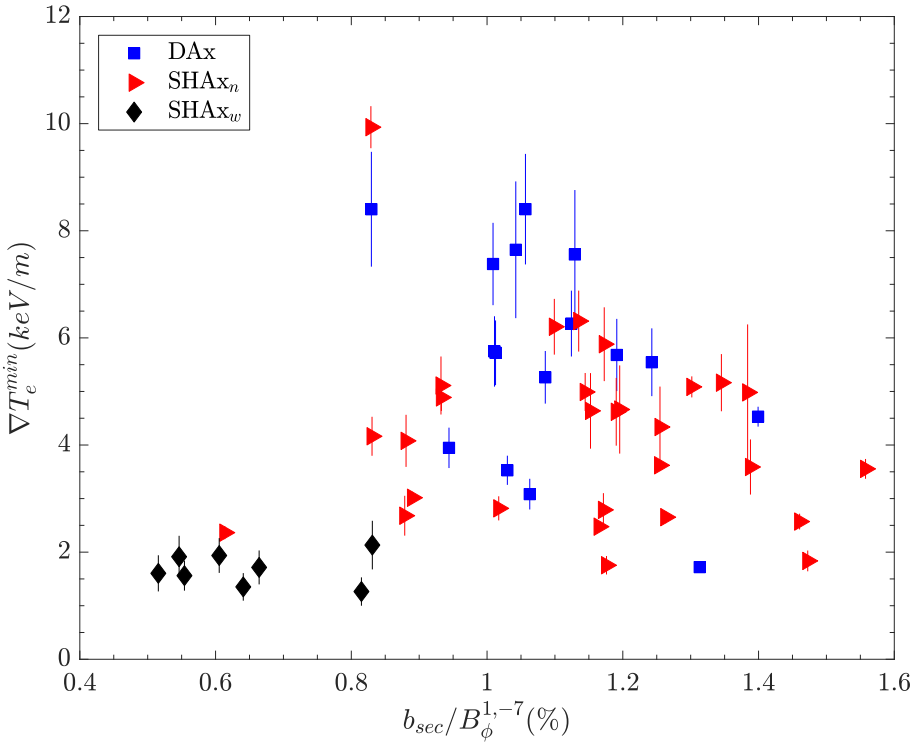

Figure 4.6: The minimum gradient is plotted as a function of the secondary modes. In both DAx and SHAx$_n$, the thermal gradient increases with the decrease of secondary modes, indicating a stochastic transport in both sub-states. While when it comes to SHAxw, the thermal gradient shows a sudden decrease. This change indicates a reduced stochastic transport properties from DAx/SHAx$_n$ to SHAx$_w$.

maintained by the reduction of stochastic transport by the existence of the separatrix as well as the stabilization due to the secondary modes. After the disappearance of the separatrix, the thermal gradients, still benefiting the stabilization of secondary modes, suffers more from the increases of stochastic transport due to the expulsion of separatrix.

The behavior of thermal gradients discussed above are localized in the eITB region. To further understand the global confinement properties in QSH states, the total energy confinement time is investigated in the following section.

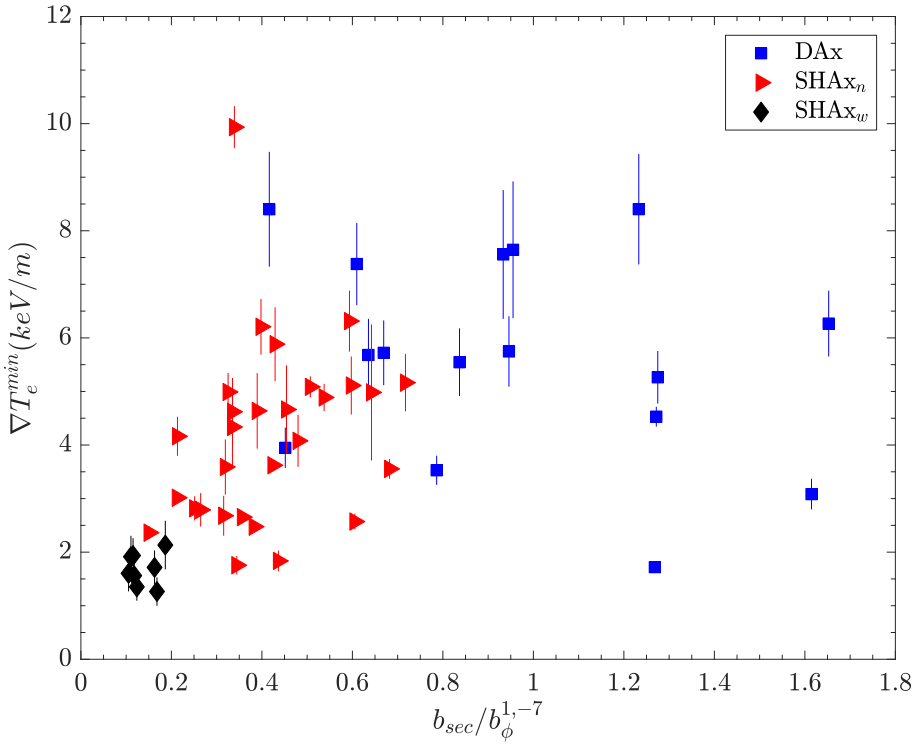

Figure 4.7: Minimum thermal gradient is plotted as a function of $b_{sec}/b_\phi^{1,-7}$.In DAx group, the thermal gradients shows a negative correlation with respect to the value of $b_{sec}/b_\phi^{1,-7}$ while in both SHAx$_n$ and SHAx$-w$ groups, the thermal gradients show a positive correlation, instead.

4.2 Energy confinement time

Energy confinement time is calculated as:

$$\tau = \frac{3}{2}\int_V K_B n(T_e + T_i)dV\,/(P_{in}) \tag{4.2}$$

where K_B is the Boltzmann constant, n is the electron density, T_i is the ion temperature and P_{in} is the input power. Concerning the volume information, a more detailed approach, considering the correct shape of the non-axisymmetric flux surfaces is adopted with the helical reconstruction of magnetic field using SHEq. Also, all the profiles used here (T_e, T_i and n) are remapped over the helical flux surfaces based on the same reconstruction. In this way, a more precise energy confinement

time is obtained. The density profiles are assumed to have this shape:

$$n = 0.8n_0 \left[1 - (r/a)^{10}\right] + 0.2n_0 \tag{4.3}$$

where n_0 is the plasma density in the core. This is due to the fact that in RFX-mod, the shape of the density profile is mainly ruled by the density level, by an interplay of stochastic transport, electrostatic transport and source effects[38, 39].
Also the ion temperature is assumed to be the same as electron temperature. Note that this assumption only affects the absolute value of the energy confinement time. The confinement time, plotted as a function of the normalized dominant mode, is shown in Figure 4.8(a). In DAx states, the average confinement time is around 1.4ms. It increases to 1.7ms in SHAx_n and eventually in SHAx_w, confinement time arrives at around 2ms. The increase of the confinement time indicates a less chaotic plasma in SHAx_w than in DAx. This is confirmed by looking into the global dynamo parameter: $(1-F)/\Theta$. From Figure 4.8(b) it can be seen that the dynamo parameter slightly decreases with the increase of the normalized dominant mode, which means that from DAx to SHAx_w, the plasma goes into more ordered states.

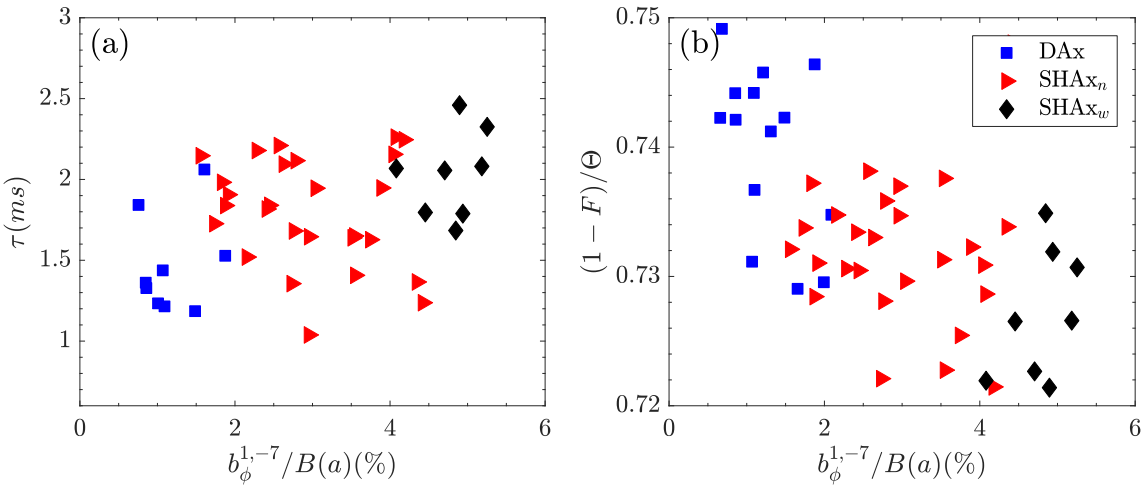

Figure 4.8: (a): Total energy confinement time as a function of normalized dominant mode. The mean value increases from around 1.4ms in DAx up to around 2ms in SHAx_w. (b): The dynamo effect $(1-F)/\Theta$ decreases with the increase of the normalized dominant mode.

4.3 Thermal Gradient after Remapping

As mentioned above, the database was selected based on the angle range of -35° and 35°. The above mentioned results are based on the experimental data. Here we briefly present the results after rotating the angle to be 0, i.e., the maximum thermal structure width lies on the mid plan. The rotation is based on the principle that after rotation, the minimum helical flux lies on the mid-plane. The definition of the helical flux function Φ, containing both the equilibrium flux and the dominant mode flux:

$$\Phi = \Phi_0 + \tilde{\Phi}\sin(m\theta - n\phi + \phi_0) \tag{4.4}$$

Where Φ_0 is the equilibrium flux function, $\tilde{\Phi}$ is the amplitude of the m=1, n=-7 mode flux and ϕ_0 is the phase of the dominant mode. The minimum helical flux lies on the mid-plane thus becomes:

$$m\theta - n\phi + \phi_0 = -\pi/2 \tag{4.5}$$

If the minimum helical flux lies on the high field side, then $\theta = \pi$. If the minimum helical flux lies on the low field side, then $\theta = 0$. Depending on these two different situations, the correct toroidal angle which should be used for rotation is thus obtained. The rotation proceeds as follows:

- Get the information of eITB gradients, i.e., four critical locations of the eITB: r^R_{Foot}, r^L_{Foot}, r^R_{Top}, r^L_{Top} and two critical temperatures: T_e^{Top} and T_e^{Foot}.
- Get the helical flux function Φ_{TS} on the Thomson Scattering toroidal angle $\phi_{TS} = 82.5°$.
- Interpolate the helical flux values on the four radial positions of the eITB mentioned in step 1, being $\Phi^{TS}_{Foot,R}$, $\Phi^{TS}_{Toot,L}$, $\Phi^{TS}_{Top,R}$ and $\Phi^{TS}_{Top,L}$.
- Obtain the new helical flux function Φ_{new} at a new toroidal angle calculated based on the rotation principle mentioned above.
- Find the new four radial locations via the four helical flux values obtained in the previous step.
- Using the new radial locations, together with the temperature values obtained in step 1, the new thermal gradients, after rotation are thus calculated.

An example of rotation, performed in a DAx state, is presented in Figure 4.9. Graph (a) and (b) are the contour plots of the helical fluxes before and after rotation,

respectively. Graph (c) shows the helical flux on the mid-plane versus the geometrical radius. Red lines indicate before rotation and blue lines indicate after rotation. The vertical lines are the locations of the thermal gradients obtained from TeGrA. Note that in DAx cases, one needs to pay attention that the remap should perform within the island region because for the same χ value, there might be another point in the core region. Also one may notice that the χ_{min} does not reach 0, this should be the reason that the grid to obtain the value of χ is not dens enough.

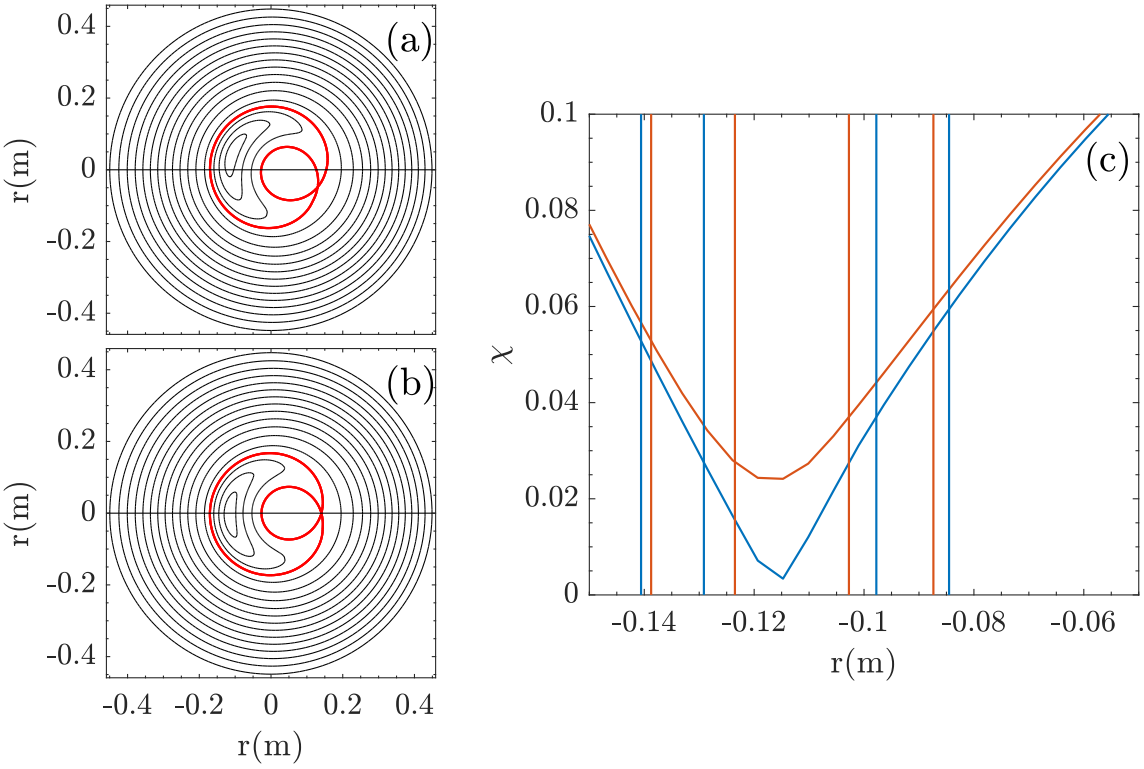

Figure 4.9: An example of rotation is presented. (a), The contour of helical flux at Thomson scattering angle. (b), the contour of helical flux after rotation. (c), The corresponding helical flux along mid-plane before (red) and after (blue) rotation. The vertical lines represent the location of the thermal gradients obtained from TeGra.

The reason why we performed TeGrA on the Thomson scattering angle rather than on the actual line of maximum thermal width is to reduce the errors induced by the remapping process. As we mentioned in Chapter 3, The remapping suffers some lack of accuracy in DAx cases and in single axis situations, even the remapping results are acceptable, the extra error induced by remapping is hard to evaluate.

Nevertheless, here we neglect the errors induced by the remapping process, only considering the error induced by TeGrA, and did the calculations on the remapped grid in machine coordinate and the results shows a good agreement with the results shown above in the sense that they both shows the same statistical trend. Here we present the 'new' results in Figure 4.10. The thermal gradients as well as the thermal structure widening behaviors the same as ones obtained in the previous sections.

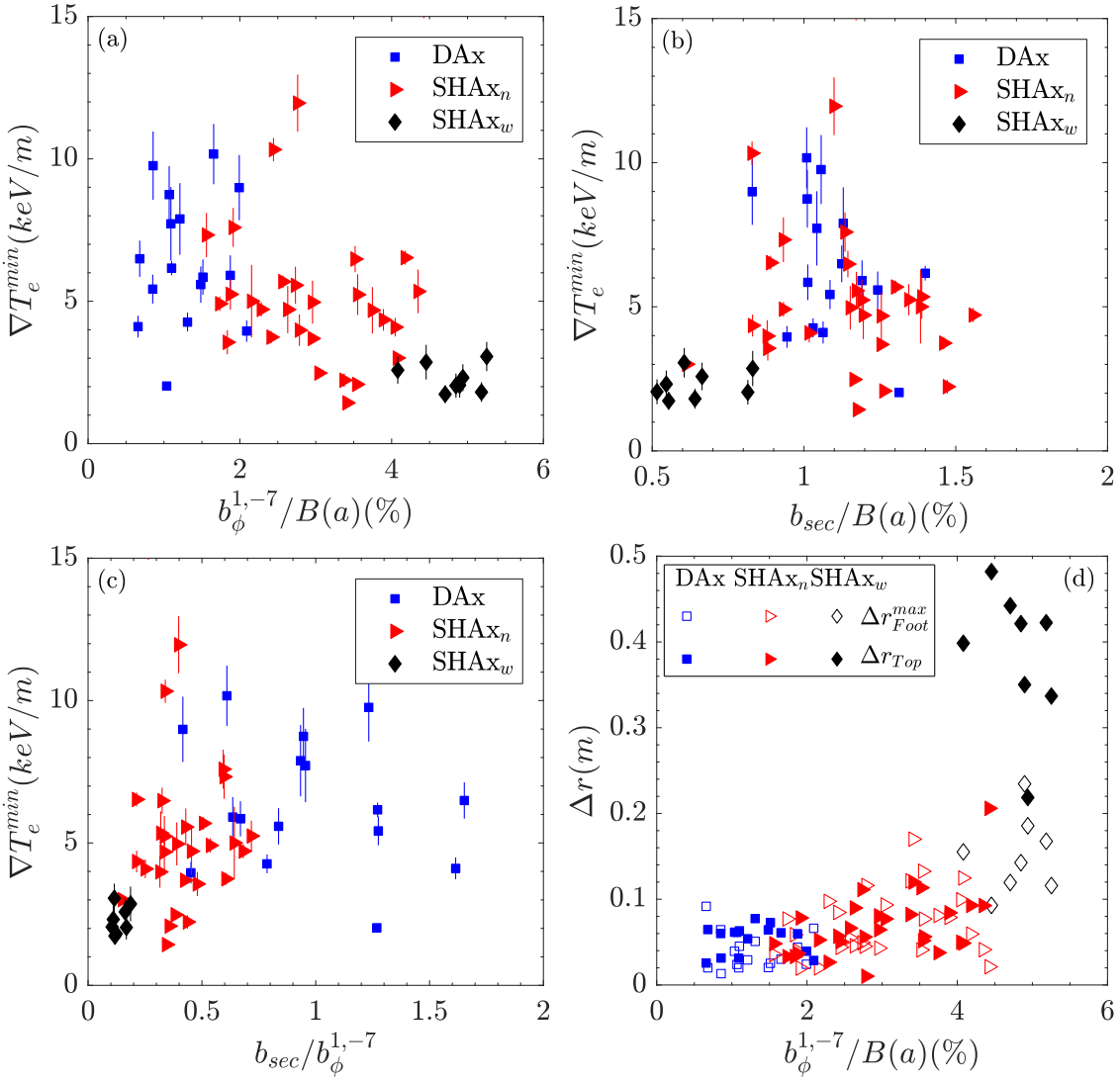

Figure 4.10: Thermal properties after rotation. (a), the minimum thermal gradients versus the normalized dominant mode. (b), The minimum thermal gradients versus the normalized secondary modes. (c) The minimum thermal gradients versus the ratio between secondary modes and the dominant mode. (d), The maximum thermal gradient width Δr_{Foot}^{max} (empty symbols) and the top width of the thermal structure Δr_{Top} (solid symbols) versus the normalized dominant mode.

Part III

Radial Electric Field in Vicinity of Magnetic Island in TJ-II

5

Enhanced Radial Transport due to Toroidal Viscosity in Tokamaks

Plasma confinement property is one of the most important issue for fusion research. The goal of fusion reactor is to achieve fusion by confining plasmas within sufficient long time. Thanks to the existence of nested magnetic flux surfaces, the radial particle transport processes are strongly suppressed. Nonetheless, the radial transport is sill one of the main particle and energy loss in fusion plasmas. This chapter discuss the situation of distorted magnetic surfaces due to the existence of magnetic islands. More specifically, the enhanced radial transport in vicinity of magnetic islands due to the enhanced toroidal viscosity is presented.

5.1 Symmetry Breaking Effect: Enhanced Radial Transport

Tokamak is a toroidal magnetic fusion device featuring toroidal symmetry. Charged particles are bonded on the flux surfaces with small loss via radial transport process across the magnetic flux surfaces. This is true within neoclassical transport theory and the magnetic configuration poses perfect toroidal symmetry. Particle fluxes are intrinsically ambipolar:

$$\Gamma_i = \Gamma_e \tag{5.1}$$

Also the guiding center trajectories of particles are closed banana orbit on poloidal cross-section. However, in real tokamak operation, the presence of error fields or MHD activities could break the toroidal symmetry, which leads to the increase of toroidal viscosity. Consequently, the banana orbits are not closed any more and particles are drifting outwards. An enhanced radial particle transport is thus induced by the symmetry broken.

Recall the banana region in Figure 2.3, which is a linear relation between particle diffusivity D_{11} and collision frequency ν in log-log scale, it is modified into three regions according to different collision frequency: ν, $\sqrt{\nu}$ and $1/\nu$. A log-log scale plot of particle diffusivity versus collisionality is shown in Figure 5.1, for magnetic configurations with no toroidal symmetry (perturbed tokamaks or stellarators). This

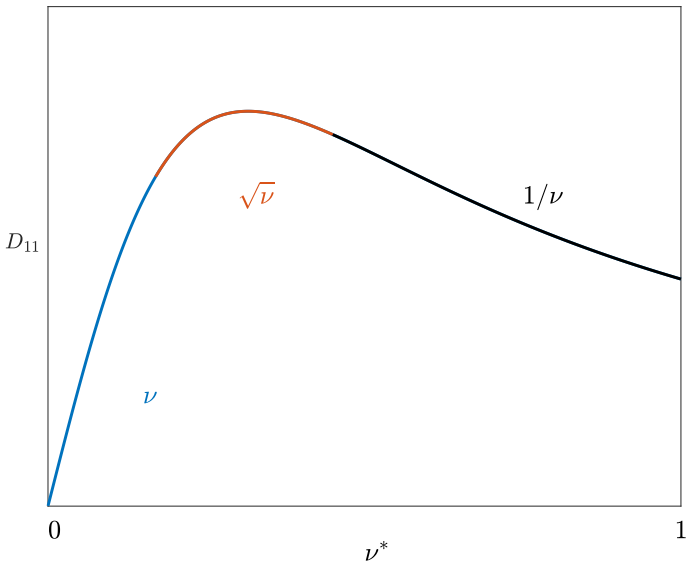

Figure 5.1: A log-log sketch of particle diffusivity D_{11} is presented as a function of the collisionality ν^*. This figure shows only the low collisionality region, i.e., $\nu^* \leqslant 1$. There are three regions grouped according to different collisionaltiy regions: ν, $\sqrt{\nu}$ and $1/\nu$. This figure is valid for tokamaks with broken toroidal symmetry and stellarators who doesn't poses any toroidal symmetry.

will leads to non-ambipolar fluxes and a local electric field is thus generated:

$$\partial \boldsymbol{E}/\partial t = \Gamma_e - \Gamma_i \tag{5.2}$$

It may play a role in plasma confinement properties by means of $\boldsymbol{E} \times \boldsymbol{B}$ plasma drift, which is considered to play an important role in $L - H$ transition by reducing the size of turbulence structure in the plasma edge.
Magnetic islands, i.e., MHD tearing modes, exist in resistive plasmas on the resonant surfaces. It modifies the magnetic topology and breaks the toroidal symmetry by distorting the nested magnetic flux surfaces. Thus, the presence of magnetic island leads to an increase of radial transport. In vicinity of magnet island, non-ambipolar flux appears and this leads to the formation of local radial electric field. In the following section, the methodology of neoclassical transport theory is presented to derive non-ambipolar flux with toroidal symmetry broken due to the presence of magnetic islands in tokamak configurations. There are two approached for neoclassical fluxes, being moment approach and kinetic approach and it has been shows that the non-

ambipolar flux origins in the appearance of toroidal viscosity [24] (see Appendix 6.10).

5.2 Radial Electric Field in Vicinity of Magnetic Island in Tokamaks

There are at least two mechanisms which can affect the toroidal viscosity. The first one is the electromagnetic torque induced by the interaction between the islands and the wall or error fields [40] and a detailed work has been carried out by A. J. Cole, etc. in Ref [41]. The second one is the plasma viscosity induced by the distortion of the magnetic surface in the vicinity of the islands. Here we present the theory developed by K. C. Shaing, focused on the second mechanism.

To begin with, the proper coordinate system should be introduced. Since we are dealing regions in vicinity of magnetic islands, it is better to use a coordinate centered in the O-point of a magnetic island. Figure 5.2 shows a contour with constant helical flux function $\Psi = \psi - \chi/q$ with ψ the the unperturbed equilibrium poloidal flux function, q the safety factor and χ the toroidal flux function. The main idea

Phys. Plasmas, Vol. 9, No. 8, August 2002 Radial electric fiel and plasma confinem

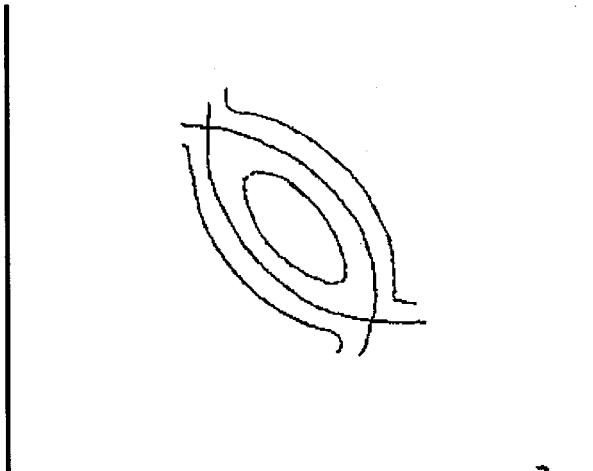

FIG. 1. A schematic diagram of a magnetic island. The constant Ψ contour is shown here. The helical angle α is similar to the polar angle in this diagram.

Figure 5.2: A schematic diagram of a magnetic island. The constant Ψ contour is shown.

is to solve the nonambipolar equation in vicinity of magnetic islands described in

Here distribution f_d is the particle drift magnetic, α is $-\zeta/q_s$ is the helical angle, q_s is the safety factor q at the rational surface where the island is centered, Ψ is the helical flu function, $C(f)$ is the Coulomb collision operator, and $f_{\rm M}$ is the Maxwellian distribution. A schematic diagram of a magnetic island is shown in Fig. 1. The radial surface label of constant Ψ is shown. The bounce averaged drift speed in the $\nabla\alpha$ direction is

$$\langle \mathbf{v}_d\cdot\nabla\alpha\rangle_b = -(I/M\Omega)(\partial\Psi/\partial\psi)(\mathbf{B}_0\cdot\nabla\theta/B) \times(\partial J/\partial\Psi)/(\partial J/\partial E), \quad (3)$$

where $I=RB_t$, R is the major radius, B_t is the toroidal mag-

where $\Phi' = \partial\Phi/\partial\Psi$. For a large aspect tol $\ll 1$, the **E×B** drift dominates the $\langle \mathbf{v}_d\cdot\nabla\alpha\rangle_b$ the island separatrix for thermal particles Here, T is the plasma temperature. For simpl that the **E×B** drift speed dominates the speed. This assumption removes the possib super-bananas which are caused by the car ∇B drift and the **E×B** drift so that $\langle \mathbf{v}_d\cdot\nabla\alpha$ because κ^2 is a function of α through its dep it is possible that trapped particles can be co trapped or the circulating particles can be tr lessly when κ^2 is close to 1. We will ignore ity, i.e., we neglect the δ_w dependence *afte* radial drift speed from it. This is equivalent t terms of δ_w. Neglecting both of these effects banana and collisionless trapping/detrapping the radial electric dependence in the transp bounce averaged radial drift speed is

$$\langle \mathbf{v}_d\cdot\nabla\Psi\rangle_b = (I/M\Omega)(\partial\Psi/\partial\psi)(\mathbf{B}_0\cdot\nabla\theta/B \quad -1)\partial\Delta/\partial\alpha].$$

It is obvious that Eq. (2) is a complex pa equation with complete elliptical integrals as make progress, we approximate $\mathbf{K}\approx(\pi/2$ and $\mathbf{E}\approx(\pi/2)(1-\kappa^2/4+\cdots)$ for the trapped $\kappa^2<1$. With these approximations, we have $-\kappa^2$. Note that this approximation is not acc to the boundary where κ^2 is unity, as exp this approximation is consistent with our pu neglect the possibility of the collisionless t trapping that can occur when κ^2 is close to u averaged collision operator is

$$\langle C(f)\rangle_b = (\nu/B)[\partial(J\mu\partial f/\partial\mu)/\partial\mu]/(\partial J$$

Equation 5.2. The particle fluxes, by definition, is obtained as:

$$\Gamma = \int d\boldsymbol{v} f \boldsymbol{v}_d \cdot \nabla \Psi \tag{5.3}$$

$\boldsymbol{v}$ is the particle velocity, $\boldsymbol{v}_d$ is the drift velocity, f is the particle distribution function and $\nabla\Psi$ indicates the radial direction. The theory is to obtain the distribution function f through solving the kinetic equation. The theory focused on the vicinity of magnetic islands and has the following assumptions:

- Large aspect ratio devices. In this condition, the $E \times B$ drift velocity is higher than ∇B drift and curvature drift. So the drift velocity could be approximately $V_{E\times B}$.
- The size of the drift orbit is δr $rV_{dr}/V_{E\times B}$ where r is the radius and V_{dr} is the radial drift speed due to both ∇B and curvature drift. The physical meaning of this condition is to neglect the formation of supper banana orbit [42, 43].
- The process of trapping-detrapping process is neglected, i.e., the amount of particles inside of banana orbits is constant.

Guiding Center Description of Drift Kinetic Equation

The neoclassical toroidal viscosity developed by K. C. Shaing adopts the kinetic description, which starts with the guiding center description of drift kinetic equation. The general kinetic equation for charged particles is:

$$\frac{\partial f}{\partial t} + \boldsymbol{v} \cdot \nabla f + \boldsymbol{a} \cdot \frac{\partial f}{\partial \boldsymbol{v}} = C(f) \tag{5.4}$$

Where $C(f)$ is the Coulomb collision operator and $\boldsymbol{a}$, the acceleration, is given by the Lorentz force:

$$\boldsymbol{a} \equiv \boldsymbol{a}\left(\boldsymbol{x}, \boldsymbol{v}, t\right) = \frac{e}{m}\left[\boldsymbol{E}(\boldsymbol{x}, t) + \frac{1}{c}\boldsymbol{v} \times \boldsymbol{B}(\boldsymbol{x}, t)\right] \tag{5.5}$$

The equation 5.4 could be summarized as:

$$\frac{\partial f}{\partial t} + \frac{dz^i}{dt}\frac{\partial f}{\partial z^i} = C(f) \tag{5.6}$$

where z^i satisfies the transformation of $(\boldsymbol{x}, \boldsymbol{v}) \rightarrow (z^1, \cdots, z^6)$. Each guiding center can be specified by its position, magnetic moment and energy: $(\boldsymbol{x}, \mu, U)$. Adopting this guiding center coordinate, equation 5.4 could be reformed as:

$$\frac{\partial f}{\partial t} + \boldsymbol{v}_{gc} \cdot \nabla f + \frac{dU}{dt}\frac{\partial f}{\partial U} + \frac{d\mu}{dt}\frac{\partial f}{\partial \mu} = C(f) \tag{5.7}$$

Where $\boldsymbol{v}_{gc}$ is the guiding center velocity and it is dominated along $\mathbf{B}$:

$$\boldsymbol{v}_{gc} = \boldsymbol{b} v_{\parallel} + \mathcal{O}(\delta) \tag{5.8}$$

With $\boldsymbol{b} = \boldsymbol{B}/B$. The higher order is $\boldsymbol{v}_{gc} = \boldsymbol{b} v_{\parallel} + \boldsymbol{v}_d + \mathcal{O}\delta^2$, where $\boldsymbol{v}_d$ is the drift velocity and it is given by:

$$\boldsymbol{v}_d = \boldsymbol{v}_E + \frac{1}{\Omega}\boldsymbol{b} \times \left(\frac{\mu}{m}\nabla B + v_{\parallel}^2 \boldsymbol{\kappa} + v_{\parallel}\frac{\partial \boldsymbol{b}}{\partial t} \right) \tag{5.9}$$

Where Ω is the groradius of charged particles. The theory is to solve the linear version of Equation 5.7 by expressing the particle distribution f as

$$f = f_M + f_1 \tag{5.10}$$

where f_M is the equilibrium Maxwellian distribution function and f_1 is the perturbed distribution function. Thus, we have $C(f) = C(f_1)$. The zero order of equation 5.7 would be:

$$v_{\parallel}\boldsymbol{b} \cdot \nabla f_0 = C(f_0) \tag{5.11}$$

The solution is $f_0 = f_M(\Psi)$ for an unperturbed tokamak and $f_0 = f_M(\Psi, \alpha)$ for an perturbed tokamak and stellarator , where α is the helical angel.
The first order of the drift kinetic equation is:

$$v_{\parallel}\boldsymbol{b} \cdot \nabla f_1 + \boldsymbol{v}_d \cdot \nabla f_0 = C(f_1) \tag{5.12}$$

The physics in the non axis symmetric system is governed by the bounce averaged drift kinetic equation, which eliminates the information along the magnetic field. The bouncing average is defined as:

$$\langle \cdot \rangle_b = \oint d\theta (\cdot) \boldsymbol{B}_0 / |v_{\parallel}| \Big/ \oint d\theta \boldsymbol{B}_0 / |v_{\parallel}| \tag{5.13}$$

For the passing particles the integral is performed between 0 and 2π and for the trapped particles the integral is performed between $-\theta_c$ to θ_c instead. Taking the

bounce average of Equation 5.12, $v_{\|}\boldsymbol{b}\cdot\nabla f_1$ could be annihilated (see Appendix 6.8) and Equation 5.12 becomes:

$$\langle \boldsymbol{v}_d\cdot\nabla\alpha\rangle_b \frac{\partial f_0}{\partial\alpha} + \langle \boldsymbol{v}_d\cdot\nabla\Psi\rangle_b \frac{\partial f_0}{\partial\Psi} = \langle C(f_0)\rangle_b \tag{5.14}$$

In order to solve Equation 5.14, a subsidiary ordering is adapted:
In the case of $\langle \boldsymbol{v}_d\cdot\nabla\alpha\rangle_b \partial f_0/\partial\alpha \sim \langle C(f_0)\rangle_b > \langle \boldsymbol{v}_d\cdot\nabla\Psi\rangle_b \partial f_0/\partial\Psi$, which implies the drift orbit is much smaller than the characteristic length of the plasma, equation 5.14 yields to:

$$\langle \boldsymbol{v}_d\cdot\nabla\alpha\rangle_b \frac{\partial f_{00}}{\partial\alpha} = \langle C(f_{00})\rangle_b \tag{5.15}$$

And the solution is $f_{00} = f_M$. The next order equation in the subsidiary ordering is:

$$\langle \boldsymbol{v}_d\cdot\nabla\alpha\rangle_b \frac{\partial f_{01}}{\partial\alpha} + \langle \boldsymbol{v}_d\cdot\nabla\Psi\rangle_b \frac{\partial f_M}{\partial\Psi} = \langle C(f_{01})\rangle_b \tag{5.16}$$

In order to solve equation 5.16, the relative strength of the toroidal(helical) drift frequency and the collision frequency should be examined.

- The toroidal(helical) drift frequency is much smaller than the colision frequency. Equation 5.16 reduces to:

$$\langle \boldsymbol{v}_d\cdot\nabla\Psi\rangle_b \frac{\partial f_M}{\partial\psi} = \langle C(f_{01})\rangle_b \tag{5.17}$$

  The bounced averaged radial drift velocity is [44]:

$$\langle \boldsymbol{v}_d\cdot\nabla\Psi\rangle = 8\frac{I}{\Omega}\frac{\partial\Psi}{\partial\psi}\sqrt{\frac{\mu B_0}{M\Delta}}\left(\boldsymbol{E}-\frac{\boldsymbol{K}}{2}\right)\frac{\partial\Delta}{\partial\alpha} \tag{5.18}$$

  Where M is the mass, $\boldsymbol{K}$ and $\boldsymbol{E}$ are complete eliptic intergrals of the first and second kind, respectively, and $\Delta = \epsilon_s \pm \delta_W(\bar{\Psi}+\cos m\alpha)^{1/2}$ with ϵ_s the inverse aspect ratio evaluated at the resonant surface, δ_w is the island width r_W normalized by the major radius and $\bar{\Psi}$ is the helical flux function normalized by perturbed poloidal flux function $\tilde{\psi}$. The argument of the complete elliptic integrals is $\kappa^2 = (E-\mu B_0 - e\Phi + \mu B_0\Delta)/2\mu B_0\Delta$. For particles trapped in the toroidal magnetic well, $\kappa^2 < 1$ and for circulating particles $\kappa^2 > 1$.
  With a pitch angle scattering Coulomb collision operator, Equation 5.17 can be easily integrated once to obtain:

$$\frac{\partial f_0}{\partial\kappa^2} = \frac{\mu B_0}{\nu}\Delta\frac{\partial f_M}{\partial\Psi}\frac{IB_0\cdot\nabla\theta}{M\Omega B_0}\frac{\partial\Psi}{\partial\psi}\frac{\partial\Delta}{\partial\alpha}\frac{\int_0^{\kappa^2} d\kappa^2(2\boldsymbol{E}-\boldsymbol{K})}{[\boldsymbol{E}-(1-\kappa^2)\boldsymbol{K}]} \tag{5.19}$$

The flux surface averaged transport fluxes $\Gamma =< N\boldsymbol{V}\cdot\nabla\Psi >_f$ is thus obtained:

$$\Gamma = -\frac{C_1}{2}\frac{(I\boldsymbol{n}_0\cdot\nabla\theta)^2}{M^{7/2}\Omega^2}\left(\frac{q_s'}{q_s}r_w\right)^2 m^2\delta_W\epsilon_s^{3/2}\frac{F(\bar{\Psi})\sqrt{1+\bar{\Psi}}}{K(\kappa_f)}\int dW W^{5/2}\frac{1}{\nu}\frac{\partial f_M}{\partial\Psi} \tag{5.20}$$

Where N is the plasma density, $\boldsymbol{V}$ is the flow velocity, $<>_f$ indicates flux surface average, $C_1 = 0.884$, $W = Mv^2/2$, $F(\bar{\Psi}) = \oint d\alpha(\sin m\alpha)^2(\Delta/\epsilon_s)^{3/2}/\sqrt{\bar{\Psi}+\cos m\alpha}$, $I = RB_t$ and $\kappa_f^2 = 2/(1+\bar{\Psi})$.

- When the collision frequency decreases further, $\langle C(f_{01})\rangle_b < \langle \boldsymbol{v}_d\cdot\nabla\alpha\rangle_b$, equation 5.16 reduces to:

$$\langle \boldsymbol{v}_d\cdot\nabla\alpha\rangle_b\frac{\partial f_{010}}{\partial\alpha} + \langle \boldsymbol{v}_d\cdot\nabla\Psi\rangle_b\frac{\partial f_M}{\partial\Psi} = 0 \tag{5.21}$$

and

$$\langle \boldsymbol{v}_d\cdot\nabla\alpha\rangle_b\frac{\partial f_{011}}{\partial\alpha} = \langle C(f_{010})\rangle_b \tag{5.22}$$

The bounce averaged drift speed in the $\nabla\alpha$ direction is:

$$< \boldsymbol{v}_d\cdot\nabla\alpha >_b = -(I/M\Omega)(\partial\Psi/\partial\psi)(\boldsymbol{B}_0\cdot\nabla\theta/B)(\partial J/\partial\Psi)/(\partial J/\partial E) \tag{5.23}$$

Here E is the particle energy and $J = \oint d\theta v_\parallel$ is the second adiabatic invariant:

$$J = 16(\mu B\Delta/M)^{1/2}[\boldsymbol{E}(\kappa) - (1-\kappa^2)\boldsymbol{K}(\kappa)] \tag{5.24}$$

Applying Equation 5.24, the helical drift velocity after bounce average is thus:

$$< \boldsymbol{v}_d\cdot\nabla\alpha >_b = -(I/M\Omega)(\partial\Psi/\partial\psi)(\boldsymbol{B}_0\cdot\nabla\theta/B)[\mu B(2\boldsymbol{E}/\boldsymbol{K}-1)\partial\Delta/\partial\Psi - e\Phi'] \tag{5.25}$$

Where $\Phi' = \partial\Phi/\partial\Psi$. The radial drift speed after bounce average, neglecting the super banana and trapping-detrapping process, is:

$$< \boldsymbol{v}_d\cdot\nabla\Psi >_b = -(I/M\Omega)(\partial\Psi/\partial\psi)(\boldsymbol{B}_0\cdot\nabla\theta/B)[\mu B(2\boldsymbol{E}/\boldsymbol{K}-1)\partial\Delta/\partial\alpha] \tag{5.26}$$

Applying these condition, we could obtain the distribution function f_{010}:

$$f_{010} = -(\mu B_0/e\Phi')(1-\kappa^2)[(\pm\delta_W)(\bar{\Psi}+\cos m\alpha)^{1/2} \pm C1]\partial f_M/\partial\Psi \tag{5.27}$$

With $C_1 = -(\pi/2)(1+\bar{\Psi})^{1/2}/\boldsymbol{K}(\kappa_f)$ is the integration constant. The corresponding particle flux is:

$$\Gamma = -(\pi/ < g^{1/2} >) \int d\alpha \int dE(\nu q_s/MB\Delta)[(\partial\Psi/\partial\psi) \times (\boldsymbol{B}_0 \cdot \nabla\theta/B)\partial f_M/\partial\Psi]^{-1} \int_0^1 d\kappa^2 J(\partial f_0/\partial\kappa^2)^2 \quad (5.28)$$

Where $< g^{1/2} >= \int d\theta \int d\alpha/\nabla\Psi \times \nabla\alpha \cdot \nabla\theta$.

By far, we have already obtained the formula of particle fluxes with presence of magnetic islands. These equation contains complex integrals, which brings the difficulty to study. In Chapter 6, the simplified equations, based on the cylindrical approximation are presented. The justification of transfer from tokamak to stellarator is discussed. The study on this model, using the TJ-II stellarator parameters is also presented.

6 Radial Electric Field on TJ-II

This chapter presents the study of enhanced radial electric field induced by the existence of magnetic islands in TJ-II stellarators, whose mechanism is that the toroidal plasma viscosity is increased by the distortion of magnetic flux surfaces induced by magnetic islands. The naturally existed magnetic islands in stellarators have been reported that they plays a role of the formation of internal thermal transport barriers as well as the modification of local radial electric field, which is considered to play a critical role in the so-called L-H transition by the $\boldsymbol{E} \times \boldsymbol{B}$ shear. This experimentally observed radial electric field needs to be reproduced in theory in order to get a better understanding.
The theory adoped here is developed by K. C. Shaing and it was developed in tokamak plasmas who pose toroidal symmetry. Here the same equations with minor modifications has been used in TJ-II plasmas. The validation of the theory in stellarators is discussed and the results are presented.

6.1 Magnetic Islands in TJ-II

The magnetic islands in stellarators, which are current free devices, is produced by coils rather than plasma current. The natural presence of magnetic islands plays similar role compared ones in tokamaks. Low order rational surfaces are found to ease the formation of internal transport barriers both, in tokamaks and in helical devices [45, 46, 47, 48], and the transition to High confinement mode (H-mode) in helical devices [49, 50, 51, 52]. These results have been interpreted in terms of local changes in the radial electric eld and zonal ow development near low order rational surfaces which may result in a reduction of plasma turbulence [53, 54, 55]. In Ref [26], the modification of local radial electric field in TJ-II has been reported. This modification is associated with the change of the non-ambipolar fluxes, which enters into the time evolution of electric field $\partial E/\partial t = \Gamma_e - \Gamma_i$. K. C. Shaing explained this phenomenon in tokamak cases [24, 44] whose main principles are presented in Chapter 5. The main idea is that the existence of magnetic islands distorts the nested flux surfaces, giving rise to the toroidal plasma viscosity. This effect shares the common features in all fusion devices so that the same effects is induced in stellarators by the presence of magnetic islands. Here we adopt Shaing's theory for

TJ-II analysis.
First of all, two typical ι profiles, characterized by two different resonant location is shown in Figure 6.1. Unlike the big magnetic islands in RFPs, the magnetic island

Figure 6.1: Cross section of the vacuum flux surfaces in two magnetic configurations of the TJ-II Heliac and corresponding ι profiles. The resonance $\iota = 8/5$ is located in $\rho = 0.56$ in configuration labeled 96_47_63 (left), while it shifts to $\rho = 0.76$ in configuration 100_44_64 (right). The circled crosses indicate the section of the central conductors, which are protected from the plasma by the hard core.

in TJ-II are small. So in the flux equations, we neglect the T'/T in vicinity of magnetic islands. There are two points which should be clarified in order to justify the validation of Shaing's theory in stellarators:

- First of all, the neoclassical transport particle flux in stellarators is much higher than in tokamaks. This is true for stellarators with no transport optimization. The reason for this phenomenon is that the banana orbit is much bigger in stellarators than in tokamaks because there is no toroidal symmetry in the former one. Nevertheless, it is also worth mentioning that the optimized stellarators has much smaller particle fluxes by reducing the banana orbit [56]. TJ-II is a stellarator with no transport optimization so in order to 'compensate' the flux difference between tokamak and stellarator due to different geometry, a factor $big = 1000$ is multiplied to the flux equations.

- Secondly, one of the assumption in the theory developed by K. C. Shaing is that it neglects the effect of super banana. Super banana is caused by

Particle orbits in stellarators

- Following a field-line around a tokamak the magnetic field strength is approximately sinusoidal
- In a classical stellarator, there is another harmonic

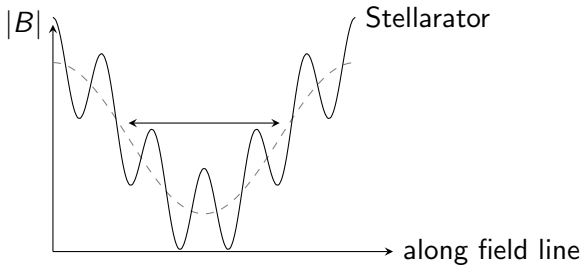

- As in a tokamak, particles can be passing or trapped due to toroidicity

Figure 6.2: Magnetic field strength $|B|$ in tokamaks (dashed line) and stellarators (solid line) along field line is presented. There are many local magnetic wells exist in stellarators.

local trapped particles due local magnetic well. Particles trapped in the super banana cannot explore the whole field. Instead, they are trapped either on the high field surfaces (upper surfaces) or on the low field surfaces (lower surfaces). Such situation will let them directly drift out because there is no cancellation effect between $\boldsymbol{E} \times \boldsymbol{B}$ and ∇B any more. In stellarators, local magnetic well commonly exists, which is shown in Figure 6.2. Hence, this assumption might be not valid for stellarator. Nevertheless, it has been proved that including the super banana does not change the dependence of the particle flux on the radial electric field [57]. Here this effect is not considered, but it should be checked in the future since the super banana effect should be much higher in TJ-II than in tokamaks.

6.2 Flux Equation for Region ν and $1/\nu$

From here on, we discuss the flux equations derived by Shaing, in cylindrical geometry. As mentioned in Chapter 5, there are mainly three sub-regions in the low collisionality region: ν, $\sqrt{\nu}$ and $1/\nu$. For ν and $1/\nu$ region, Shaing presented equations which could well describe these two regions [58]:

$$\Gamma_\nu = -C \cdot (0.22 N\nu) \left(\frac{eT}{eBr}\right)^2 \left(\frac{\delta_W}{\omega_E}\right)^2 \epsilon^{-1/2} G(\bar{\Psi}) \tag{6.1}$$

$$\Gamma_{1/\nu} = -C \cdot 0.5 \left(\frac{N}{\nu}\right) \left(\frac{eT}{eBr}\right)^2 (RB_P)^2 \left(\frac{q_s' r_W}{q_s}\right)^2 (m\delta_W)^2 \epsilon^{3/2} H(\bar{\Psi}) \tag{6.2}$$

$$\Gamma = -C \cdot \frac{N\,(cT/eBr)^2\,(\nu/\epsilon)(RB_P)^2(q_s' r_W/q_s)^2(m\delta_W)^2\epsilon^{1/2}}{\omega_E^2(RB_P)^2(q_s' r_W/q_s)^2 m^2/[0.22G(\bar{\Psi})] + (\nu/\epsilon)^2/[0.5H(\bar{\Psi})]} \tag{6.3}$$

The basic quantities are: N is the electron density, ν is the collision frequency, c is the speed of light, T is the electron temperature, $P = NT$ is the plasma pressure, Φ is the electric potential, e is the electron charge, B is the magnetic field. a is the minor radius, R is the major radius, m is the poloidal mode number. $r_W = \sqrt{2q_s^2\tilde{\psi}/(q_s' B r_s)}$ is the island width, $\delta_W = r_W/R$, $\omega_E = cE_\Psi/(Br)$ is the $E \times B$ angular speed with $E_\Psi = -d\Phi/d\Psi$, $\epsilon = a/R$ is the reversed aspect ratio. $q_s' = dq/dr$ evaluated as the resonant surface. $P' = dP/d\Psi$ and $\Phi' = d\Phi/d\Psi$. Ψ is the helical flux function centered at the magnetic island O point.
Equation 6.3 is the combined equation which could well reproduce Equation 6.1 and Equation 6.2 with the common factor $C = (P'/P + e\Phi'/T)$, assuming $T'/T = 0$ because of the small islands in TJ-II. Here the function $G(\bar{\Psi})$ is related to the first and second elliptical integrals and essentially it is a function that defines the location of the island region. Hence, for simplicity reason, here we use a Gaussian distribution function to replace it. The same technique is applied for the $H(\bar{\Psi})$ function and $X(\bar{\Psi})$ functions (presented later). Applying Equation 6.3, one could see the result of reproduction from Figure 6.2. The two graphs are the log-log scale plots of particle diffusivity $D_{11}^{i(e)}$ versus the normalized collision frequency. The superscript i and e represents ions and electrons. The black and blue dashed lines are for ν and $1/\nu$ regions. The black gray vertical lines represents the boundary below which the ν region is valid. The thine vertical red and blue lines represents the value of ion and electron ν^*, respectively. The red curves are produced by Equation 6.3. The results show a good agreement with Equation 6.1, 6.2 and Equation 6.3.
The boundary between ν and $1/\nu$ is defined as:

$$\nu_{\text{eff}} < \omega_E(RB_P)(q_s' r_W/q_s) \tag{6.4}$$

With $\nu_{eff} = \nu/\epsilon$ is the effective collision frequency defied as the ration between collision frequency ν and the revered aspect ratio ϵ.

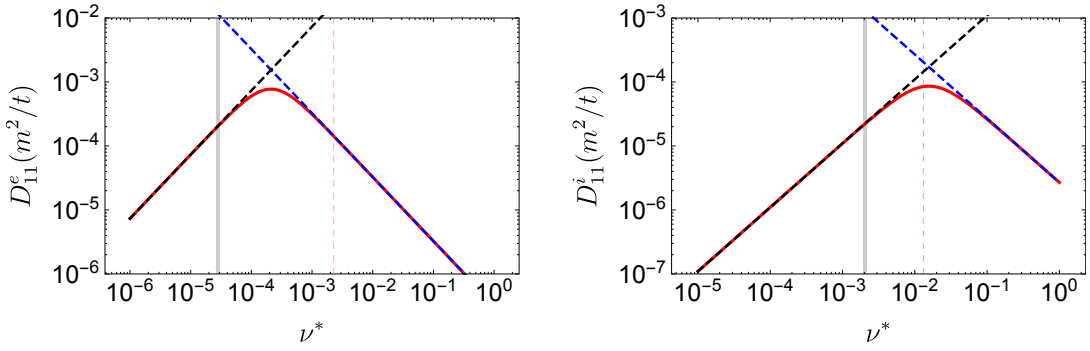

Figure 6.3: Using TJ-II parameters, the combined function(in red) could well reproduce the two separated functions in ν(dashed black line) and $1/\nu$(dashed blue line) regions. The thick gray vertical line represents the critical ν^* which indicates the end of ν region. The red vertical dashed line is the electron collisionality and the blue dashed one is the ion collisinality.

6.3 Equation for $\sqrt{\nu}$ and the complete Flux Euqation

For the $\sqrt{\nu}$ region, applying the equation from Ref [59], we could get the follow equation:

$$\Gamma_{\sqrt{\nu}} = -C \cdot 0.1\sqrt{\nu}\,(cT/eBr)^2\,\delta_W^2\sqrt{B_P R m}\,(-q' r_W/q)^{0.5}\,|\omega_E|^{-1.5}\,X(\bar{\Psi}) \qquad (6.5)$$

For the complete equation which could describe the whole ν, $\sqrt{\nu}$ and $1/\nu$ regions(equivalent to $\nu^* < 1$), first we simplify the separate flux function as:

$$\Gamma_{\nu} = -C \cdot K_{\nu} \cdot (\nu)$$
$$\Gamma_{\sqrt{\nu}} = -C \cdot K_{\sqrt{\nu}} \cdot (1/\nu)$$
$$\Gamma_{1/\nu} = -C \cdot K_{1/\nu} \cdot (\sqrt{\nu})$$

and the corosponding coefficient K_{ν}, $K_{\sqrt{\nu}}$, $K_{1/\nu}$ are:

$$K_{\nu} = 0.22N(cT/eBr)^2(\delta_W/\omega_E)^2\epsilon^{-1/2}G(\bar{\Psi})$$
$$K_{\sqrt{\nu}} = 0.1\,(cT/eBr)^2\,\delta_W^2\sqrt{RB_P m}\,(q_s' r_W/q)^{0.5}\,|\omega_E|^{-1.5}\,X(\bar{\Psi})$$
$$K_{1/\nu} = 0.5N(cT/eBr)^2(RB_P)^2(q_s' r_W/q_s)^2(m\delta_W)^2\epsilon^{3/2}H(\bar{\Psi})$$

Using these notation we present the complete transport equation for $\nu^* < 1$ region, including ν, $\sqrt{\nu}$ and $1/\nu$ regions:

$$\Gamma = -C \cdot \frac{K_\nu K_{\sqrt{\nu}} K_{1/\nu} \cdot \nu}{(K_{\sqrt{\nu}} + K_\nu \cdot \sqrt{\nu})(K_{1/\nu} + K_{\sqrt{\nu}} \cdot \nu^{1.5})} \tag{6.6}$$

The comparison between Equation 6.3 and 6.6 is shown in Figure 6.4. The green dashed line represents the $\sqrt{\nu}$ region and it shares one common point with the black solid line from Equation 6.3 and the gray vertical line from Equation 6.4. The red solid line is from Equation 6.6. It is clear to see that when collisionality reaches $\sqrt{\nu}$, the value of D_{11} is.

Now we used this complete equation to compare tokamak with stellarators. Using

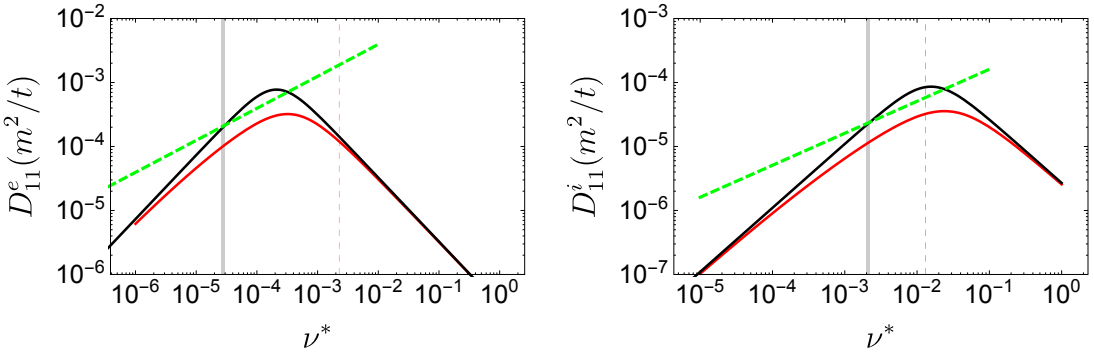

Figure 6.4: Comparison between equation 6.3(black, solid) and equation 6.6(red, solid). The dashed green line represents the $\sqrt{\nu}$. It is clear to see that the green line and black line has a common point which also belongs to the gray vertical line which is the end of ν region. The vertical red and blue dashed lines are the collisionality for electrons and ions, respectively.

Equation 6.6, one needs to justify that it suits the situation for tokamaks and also for stellarators. Using the Figure in Ref[60] as the standard TJ-II $D_{11} - \nu^*$ diagram and applying the same plasma parameters in Equation 6.6, the comparison is obtained and shown in Figure 6.5. The black figure is from Ref [60]. The red line represents electrons and the blue line represents ions. Note that the geometry factor $big = 1000$ has been multiplied to Equation 6.6.

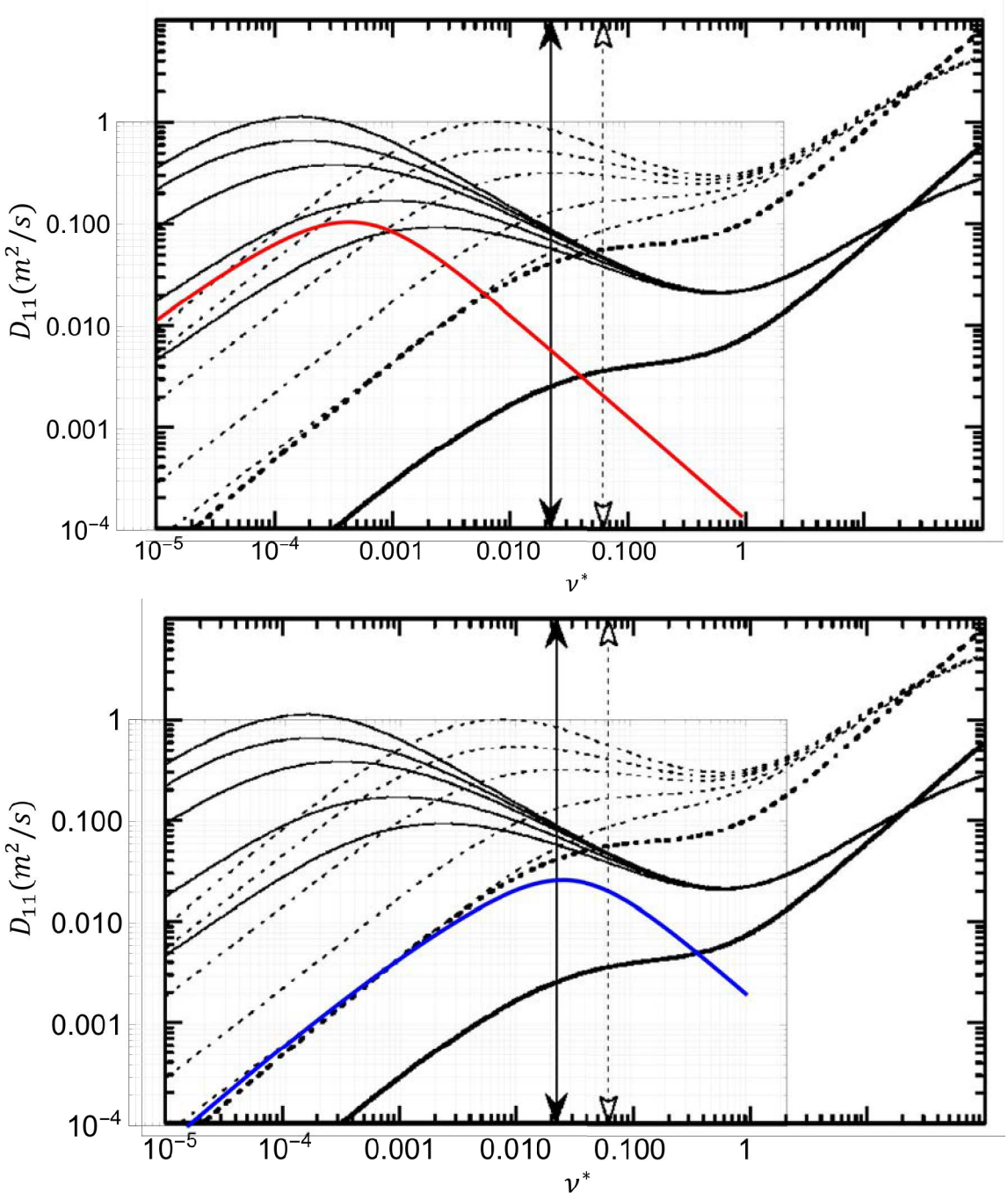

Figure 6.5: Comparison between Equation 6.6 multiplied by 1000 (colored lines with $|E_r| = 2300V/m$) and the TJ-II data as well as tokamak cases. The black background figure is from Ref [60]. The solid black lines are for electrons and the dashed ones are for ions. From top to bottom with $e\Phi/T = 0, 1, 2, 5, 10$. The thick solid and dashed black lines are corresponding curves to the equivalent tokamak. The red and blue lines represents electrons and ions, respectively.

Quantity	Value
N(m^{-3})	0.36×10^{19}
$T_e(eV)$	350
$T_i(eV)$	$T_e/3$
$B_T(T)$	0.995
B(T)	1
R(m)	1.5
a(m)	0.2
m	5
n	8
q	$1/[1.551 + 0.05238r - 0.07569(r/a)^2 + 0.12862(r/a)^3]$

Table 6.1: A typical TJ-II plasma parameter.

6.4 Discussions on the Complete Equation

Unit Analysis

The flux equations mentioned above is derived from $\Gamma = \langle NV \cdot \nabla\Psi \rangle$ with $\langle \cdots \rangle$ represents the flux surface average. This definition leads to a different flux unit $[B]/(lt)$ since $\nabla\Psi$ has a unit of $[B]l$ which is different from 1. Secondly, $P' = dP/d\Psi$, $\Phi' = d\Phi/d\Psi$ and $E_\Psi = -d\Phi/d\Psi$ will have units which doesn't have physical meaning. So here one coordinate transformation is needed to convert the equations in order to use the physical quantities with international units. One may apply $dr/d\Psi = (dr/d\Psi_P)(d\Psi_P/d\Psi) = [(2\pi B_P R)(q'_s r_W/q_s)]^{-1}$ on the flux equations to get there. Note that this 'extra' step is due to the choice of coordinate. The three coefficient K_ν, $K_{\sqrt{\nu}}$ and $K_{1/\nu}$ are:

$$K_\nu = 0.22(dr/d\Psi_P)^{-2} N (cT/eBr)^2 (\delta_W/\omega_{E_r})^2 \epsilon^{-1/2} G(\bar{\Psi}) \tag{6.7}$$

$$K_{\sqrt{\nu}} = 0.1(dr/d\Psi_P)^{-1.5} (cT/eBr)^2 \delta_W^2 \sqrt{RB_P m} (q'_s r_W/q)^{0.5} |\omega_{E_r}|^{-1.5} X(\bar{\Psi}) \tag{6.8}$$

$$K_{1/\nu} = 0.5N(cT/eBr)^2 (RB_P)^2 (q'_s r_W/q_s)^2 (m\delta_W)^2 \epsilon^{3/2} H(\bar{\Psi}) \tag{6.9}$$

Where $\omega_{E_r} = cE_r/Br = -(c/br)(d\Phi/dr)$. Together with the common factor $C = (dr/d\Psi_P)(1/P \cdot dP/dr + 1/T \cdot d\Phi/dr)$ and the complete flux equation $\Gamma = (dr/d\Psi)\Gamma_r$, Γ_r indicating the flux with unit of $1/(l^2 \cdot t)$, $(q'_s r_W/q)$ disappears in those three coefficient.

Validation of the collision frequency region

As this theory is derived from the "low" collision frequency region, meaning the $\nu^*_{i,e} = \nu_{i,e}/\omega_{b,(i,e)} < 1$ with ν the collision frequency and $\omega_b = v_{th}/qR$ the bounce frequency. This condition leads to a collision frequency limit:

$$T_e > 2.22 \times 10^{-9}\sqrt{N_e \ln \Lambda_e} \tag{6.10}$$

$$T_i > 1.86 \times 10^{-9} Z^2 \mu^{-1/4}\sqrt{N_i \ln \Lambda_i} \tag{6.11}$$

With $\nu_e = 2.91 \times 10^{-12} N_e \ln \Lambda_e T_e^{-3/2}$, $\nu_i = 4.80 \times 10^{-14} Z^4 \mu^{-1/2} N_i \ln \Lambda_i T_i^{-3/2}$, Z is the ion charge state, $\mu = m_i/m_p$ where m_i is the ion mass expressed in the proton mass m_p. $\ln \Lambda_{e,i}$ is the Coulomb logarithm for electron and ion.
Given the Coulomb logarithm doesn't change much, it is clear to see that the ion and electron temperature has a lower limit respect to a given plasma density.

Scan of the E_r

As one could see from the two equations, the Γ_ν depends on the radial electric field E_r. In order to see the function of the E_r, a scan of the E_r value, which could see from Table 6.1 , is shown in Figure 6.6 based on a typical TJ-II plasma with its parameters: $n = 10^{19}$, $T = 300eV$, $B = 1T$. It is obvious to see that since the $D_{11}(1/\nu)$ doesn't depend on electric field, the $D_{11}(\nu)$ curve decreases as the E_r increases and the cross point between the two curves moves in the positive direction of collision frequency.

Effect on radial electric field E_r from different plasma parameters

- $q'_s r_W/q_s$. This parameter is not in the particle flux equation, as one could see from the discussion in the unit analysis 6.4. However, the island width r_W is a function of q'. If the magnetic island width r_W is fixed, then particle diffusivity D_{11} doesn't depend on the parameter $q'_s r_W/q_s$. Therefore, changing this parameter will lead to the same D_{11} and E_r. The reason this parameter is irrelevant to both D_{11} and E_r is because it comes from the choice of the flux coordinate system and when we calculate the flux, one should convert back to machine coordinate so this factor disappears.

- Island width r_W. As one could see from Equation 6.6, the island width, which is inside of $\delta_W = r_W/R$, is an universal parameter of the particle flux. The

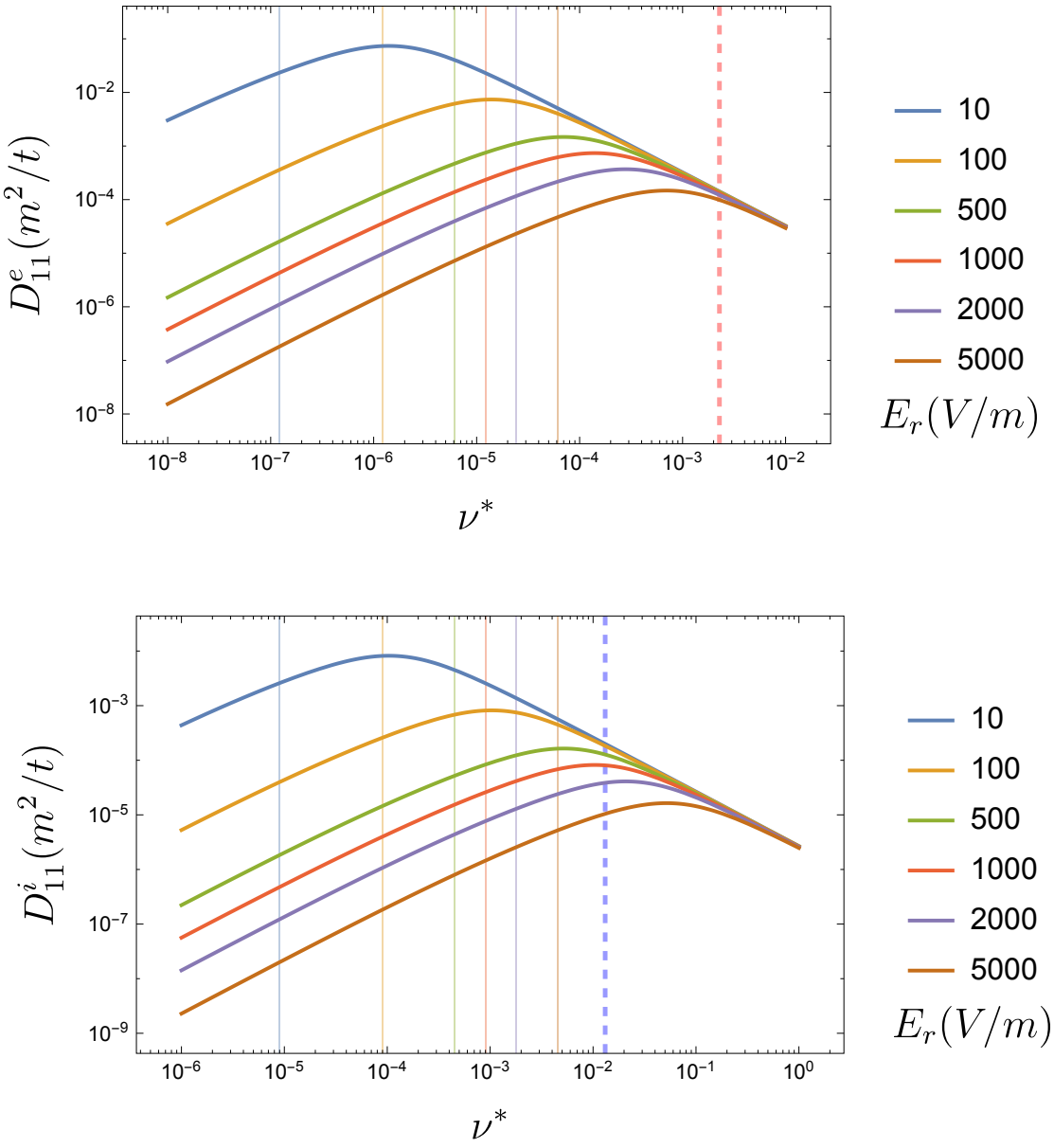

Figure 6.6: Radial electric field E_r scan in a typical TJ-II plasma. The red vertical dashed line is the electron collisionality and the blue one is the ion collisionality.

three coefficients $K_{\nu,\sqrt{\nu},1/\nu}$ have common dependence on δ_W, which justify the comment before. Hence, the island width could only affect the absolute value of the separated particle flux in each region while as for the radial electric field E_r which is the root of equation of $\Gamma_e - \Gamma_i = 0$, is independent of the island width and this is confirmed by the simulation results.

- Poloidal mode number m. The poloidal mode number, especially the low m number islands, in principle, should have big impact on the radial electric field. Here the impact of poloidal mode number is investigated. The poloidal mode number is functional when the collision frequency is in the $\sqrt{\nu}$ or $1/\nu$ regions, as one could see from the diffusivity equations. The simulations are performed on the same TJ-II plasma parameters used before and the result is shown in Figure 6.7. Strangely, changing the mode number does not change the value of radial electric field. The reason is that the electric field in these three calculations are around -300 V/m and using this value to back check in Figure 6.6, we find that roughly both electrons and ions are all in $1/\nu$ region and thus the mode number doesn't play a role in the charge balance equation.

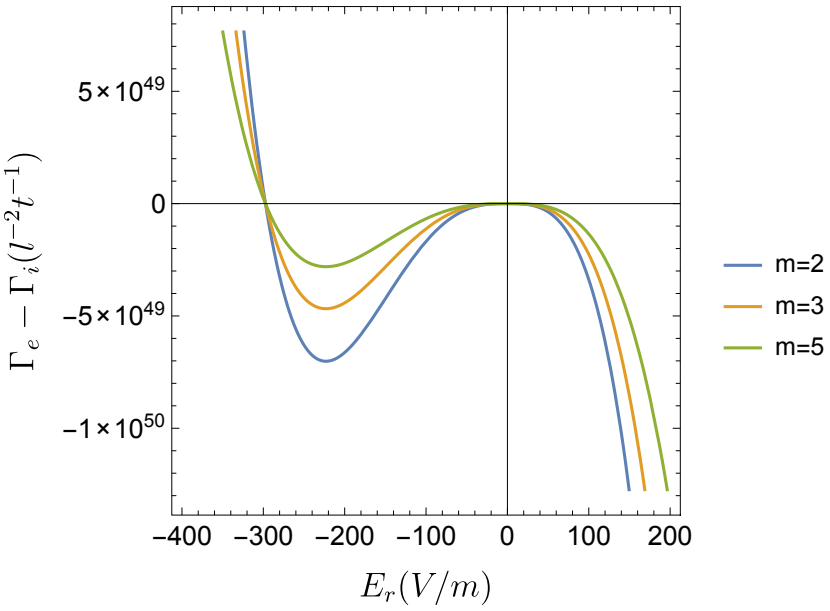

Figure 6.7: Estimate the effect of poloidal mode number m on the radial electric field, using the plasma parameter listed in Table 6.1.

- Scan of T_i. This section is to investigate the effect of T_i/T_e on radial electric field. The excises are done based on the same plasma parameters presented in Table 6.1 with the only exception of electron temperature T_e=350eV. The value of $\Gamma_e - \Gamma_i$ is plotted as a function of both E_r and T_i, shown in Figure 6.8. The contour line which has the value of zero is where the root(s) of equation $\Gamma_e - \Gamma_i$ lies on, i.e., the solution of ambipolar electric field. At the region $T_i < 105eV$, there is single, positive ambipolar electric field. When ion temperature increases between 105 eV and 250 eV, three ambipolar electric field appears with the middle one usually the unstable one [61]. And in the region with $T_i > 250eV$, single, negative ambipolar electric field appears. Finally, one interesting point around $T_i = 105eV$ should be pointed out. At this point, the electric field is zero, meaning the fluxes $\Gamma_e = \Gamma_i$ fulfill the ambipolar condition. This phenomenon is further studied below.

- Investigate the effect of T_i/T_e on the ambipolar electric field. This time we make scans on both electron and ion temperatures and we calculated the value of ambipolar electric field, by solving the equation $\Gamma_e = \Gamma_i$. The result of these scans are shown in Figure 6.9.

  There is a vertical contour line with its value $E_r = 0$ around $T_i/T_e \approx 0.3$. This means ambipolar fluxes generates in vicinity of magnetic islands under the condition of $T_i/T_e = 0.3$. This can be easily proved. Let us take the charge balance equation $\Gamma_e - \Gamma_i = 0$ with the condition of $E_r = 0$. One could easily get the solution:

  $$(T_i/T_e)^{7/2} \approx 60.42\,(\ln \Lambda_e / \ln \Lambda_i) \tag{6.12}$$

  where $\ln \Lambda_e$ and $\ln \Lambda_i$ are the Coulomb logarithm for electrons and ions, respectively. The value of $\ln \Lambda_e / \ln \Lambda_i$, despite of depending on the value of electron and ion temperature as well as the plasma density, has tiny change around the value 1.1. So the solution to $\Gamma_e - \Gamma_i = 0$ with $E_r = 0$ is $T_i/T_e \approx 0.3$. This confirmed the observation of $E_r = 0$ around $T_i = 1 - 5$ eV in Figure 6.9. In that case, the ratio $T_i/T_e = 105/350 \approx 0.3$.

- Here the effect of plasma density on the ambipolar electric field is investigated. As the plasma density increases a factor of 50%, one root solution appears in all T_i/T_e region, which is shown in Figure 6.10. The same $E_r = 0$ point appears, which has been shown in Figure 6.9.

From the discussion above, we know that the ambipolar electric field disappears when $T_i/T_e \approx 0.3$. This results shows that the modification effect due to magnetic

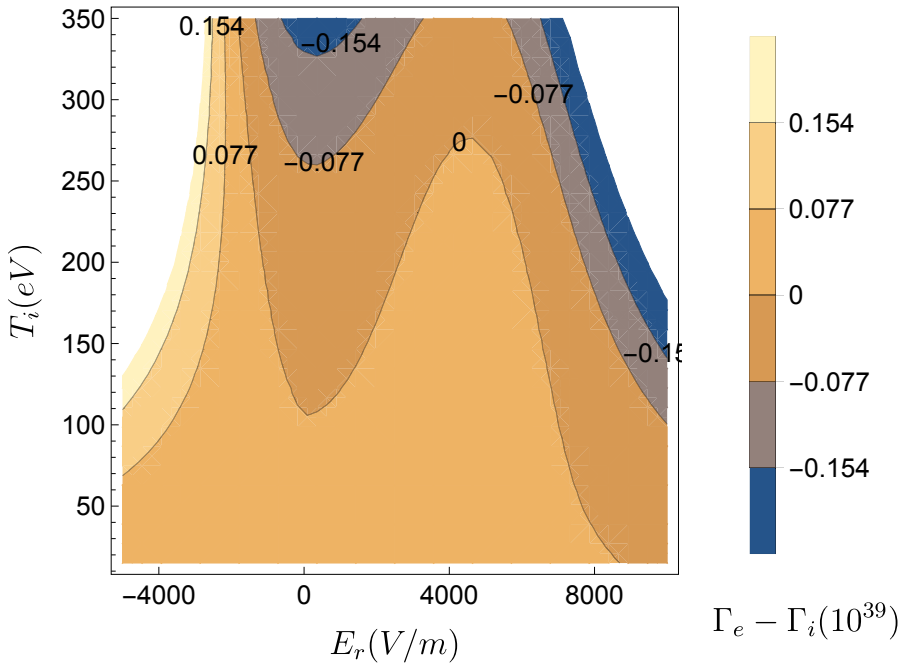

Figure 6.8: The solution for electric field under steady state assumption. The plasma parameters used is presented in Table 6.1 with electron temperature modified to 350 eV. The contour line with $E_r = 0$ is the solution for ambipolar conditions. With ion temperature below 105 eV, single positive electric field appears. As the ion temperature increases, three electric field solutions, one negative and two positive, appear. The middle solution is unstable [61]. And finally, when the ion temperature increases above 250 eV, single negative ambipolar electric field appears.

islands disappears and the fluxes are ambipolar. What is more, if we increase the ratio between ion and electron temperature, the electric field changes its sign from positive to negative and its amplitude also increases (neglecting the unstable ones in the middle). Finally, the plasma density also plays a role of island modification effect. The unstable ambipolar electric field region disappears with an increase of plasma density (in our case, 50% increases on plasma density shows the disappearance of non-stable E_r region). These studies have been performed on an steady state situation $\partial E/\partial t = 0$, which suffers lack of time evolution process. In the next section, this model has been implemented into ASTRA and the preliminary results are presented and discussed.

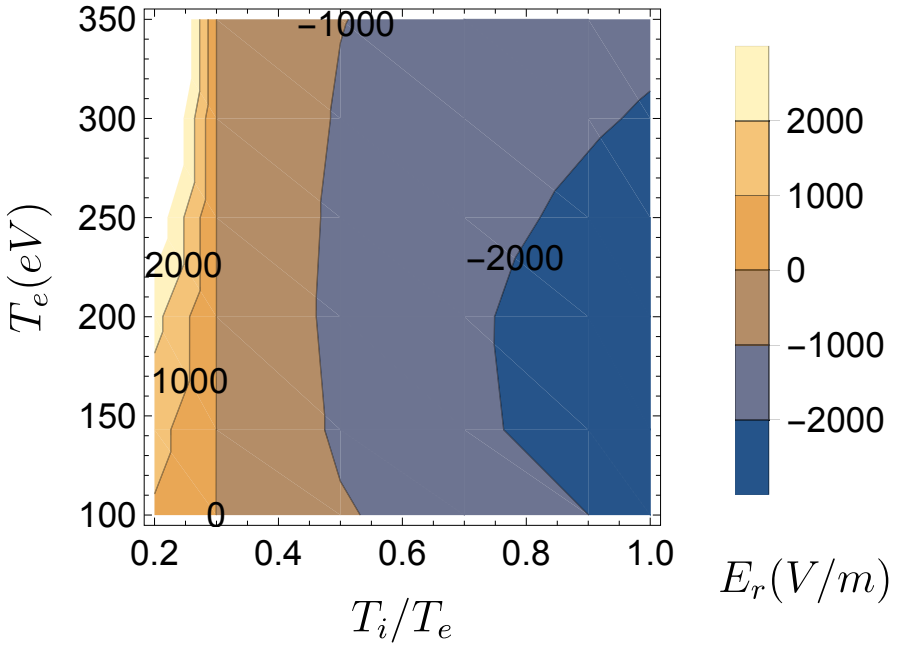

Figure 6.9: The solution for electric field under steady state assumption. The plasma parameters used is presented in Table 6.1. With a fixed electron temperature, the solution of ambipolar electric field is positive in low ratio of $T_i/Te < 0.3$ and negative in high ratio of $T_i/T_e > 0.3$. When the ratio between ion and electron temperature equals 0.3, the ambipolar electric field equals zero, which is shown as the vertical line at T_i/T_e.

6.5 Preliminary Results Using ASTRA

The above mentioned theory is adopted in ASTRA via $\Gamma = \Gamma^{Neoclassical} + \Gamma^{island}$. The plasma parameters used here is presented in Figure 6.11 and the plasma is obtained with electron cyclotron heating (ECRH). The island width is assumed to be 0.5cm. First of all, the theory is tested on a tokamak case, i.e., $\Gamma^{Neoclassical} = 0$ for different island locations. The result is shown in Figure 6.12. The radial electric field in tokamaks changes its sign depends on different locations of the resonant positions. It is positive in both $\rho = 0.48$ and $\rho = 0.65$. When the resonant position moves outwards, reaching $\rho = 0.82$, the electric field shows positive on the inner side and negative on the other side. Thus, a electric shear generated. With further outer moving, arriving at $\rho = 0.94$, the electric field becomes negative. Also it it clear that the electric field only appears around the resonant location. This is true because in

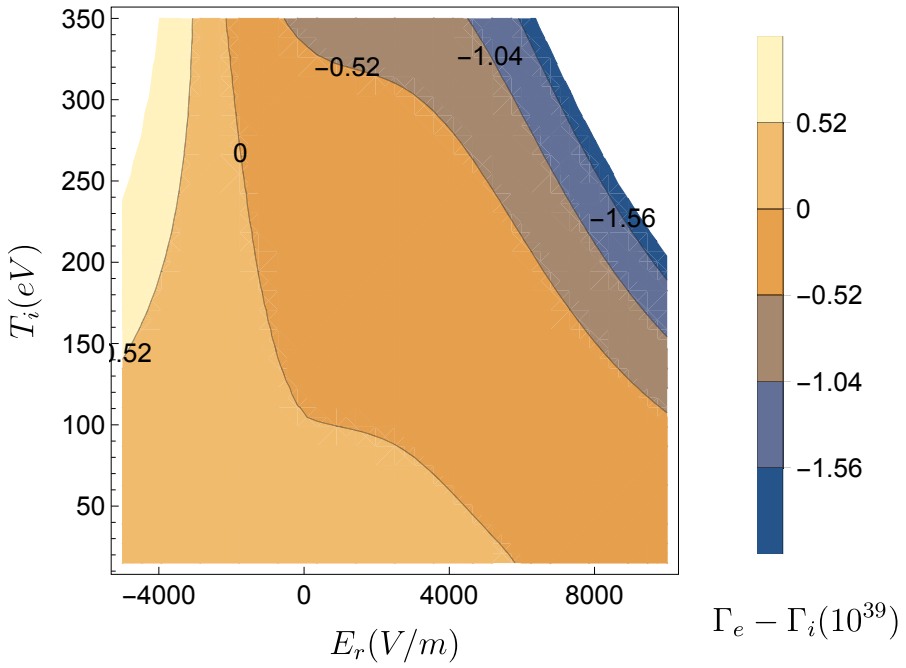

Figure 6.10: The solution for electric field under steady state assumption. The plasma parameters used is presented in Table 6.1 with 150% plasma density and electron temperature $T_e e$=350eV. At all ion temperatures, the ambipolar electric field only has one solution, as indicated by the 0 coutour line. When the ion temperature is below 100 eV, the ambipolar electric field is positive and above this value, it is negative.

tokamaks, regions far away from the vicinity of resonant surfaces, the electron and ion fluxes are intrinsically ambipolar.

Secondly, a neoclassical model developed by Koverizhnykh [62] is included as the background of the neoclassical transport, together with Shaing's model. The result is presented in Figure 6.13. The smooth line represents the background profile, i.e., generated only by Kovrizhnykh's model. The three 'bumps', located in the inner and outer regions, are one generated with also Shaing's formula. The inner two results shows a positive results with either enhancement or decrease effect on the background profile. In the outer region, however, the electric field is negative and it shows a enhancement on the background profile.

And finally, another neoclassical transport model developed by Beidler [63] is applied as the background transport, together with Shaing's model. The result is presented

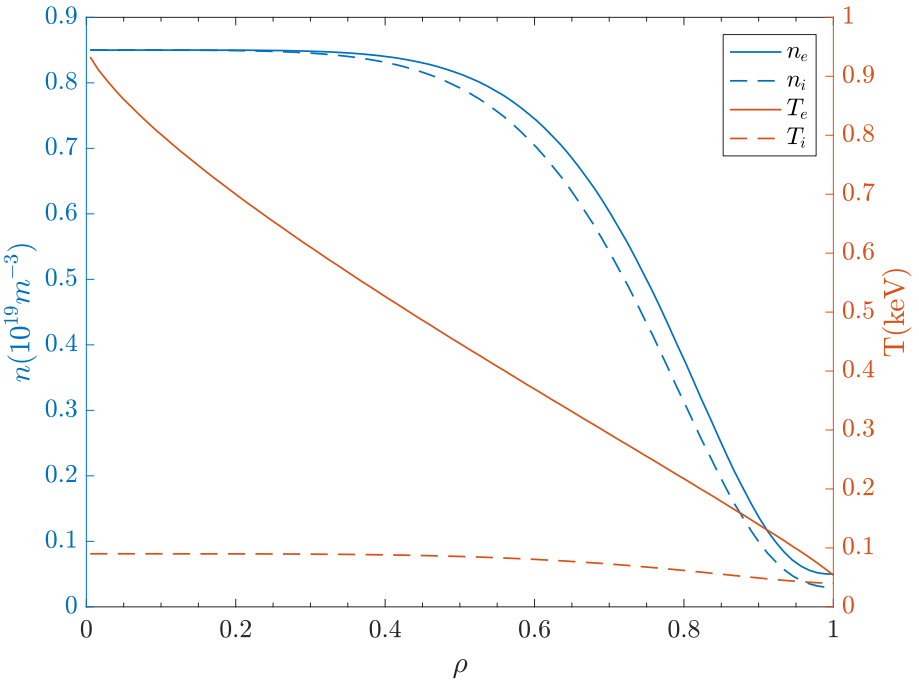

Figure 6.11: The parameters of ECRH plasma in TJ-II. The blue solid line represents the electron density and the dashed blue line represents the ion density. The red solid line represents the electron temperature and the dashed one represents the ion temperature. This parameters are used in the following calculations in ASTRA.

in Figure 6.14. Unlike the results shown in Figure 6.13, the modification on the electric profile using Beidler's model shows always enhancement effect. The most inner resonant position shows a big decrease effect on the background and the most outer one shows a increase effect. These two positions agrees with the one shown in Koverizhnykh's model. However, the middle resonant position, shows a decrease effect which is different from the one in Koverizhnykh's model.

From the preliminary results shown above, we begin to understand the theory proposed by Shaing. The island effect will effect the background electric field, both increase and decrease. Also the sign of electric field due to modification really differs from one model to another. Another important thing needs to emphases is that so far, all the excises are done in ECRH plasmas.

Besides this ECRH plasmas, an NBI plasma in TJ-II is also used to test this model. The plasma density is around $1.2\times10^{19}m^{-3}$, the central electron and ion temperatures are $0.35keV$ and $0.15keV$, respectively. The same island width as well as the locations

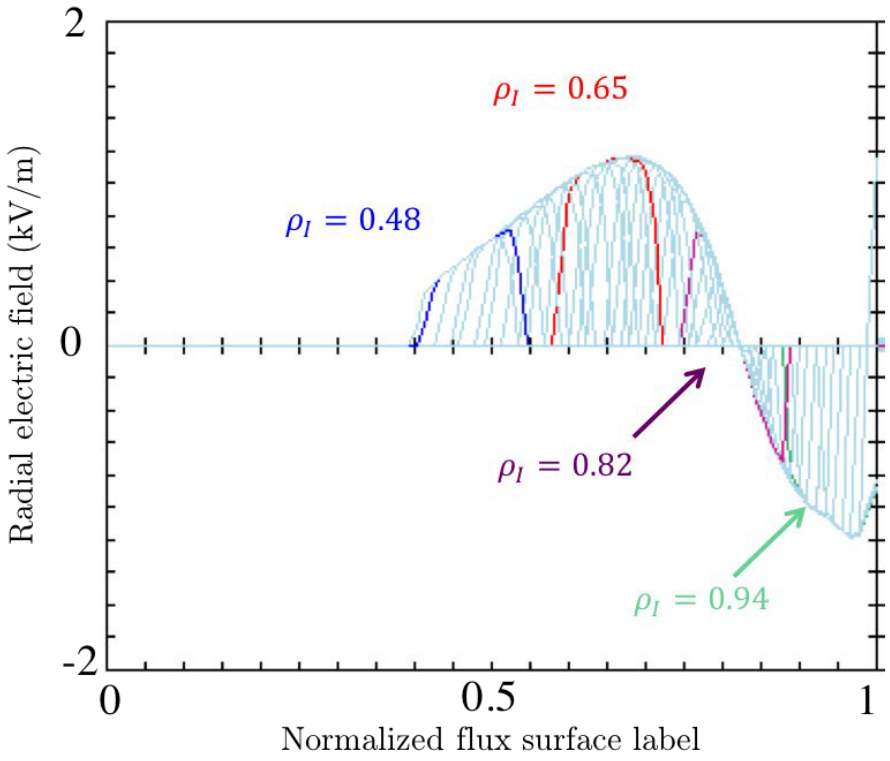

Figure 6.12: Electric field profiles with scan of resonant positions in tokamak parameters. Four different island locations have been applied in ASTRA with Shaing's model. Four positions are marked at normalized flux labels $\rho = 0.48, 0.65, 0.820.94$, respectively.

are used here, adopting 1. Kovrizhnykhs model together with Shaing's model; 2. Beidlers model with Shaing's model. The results are shown in Figure 6.15. The left graph is obtained using both Kovrizhnykh's model and Shaing's formula. The left one is obtained using both Beidler's model and Shaing's formula. The smooth line represents the background radial electric field and the 'bumps' are the extra contribution from Shaing's theory. Clearly, the background radial electric field profile is always negative and the contribution from Shaing's theory is always positive.

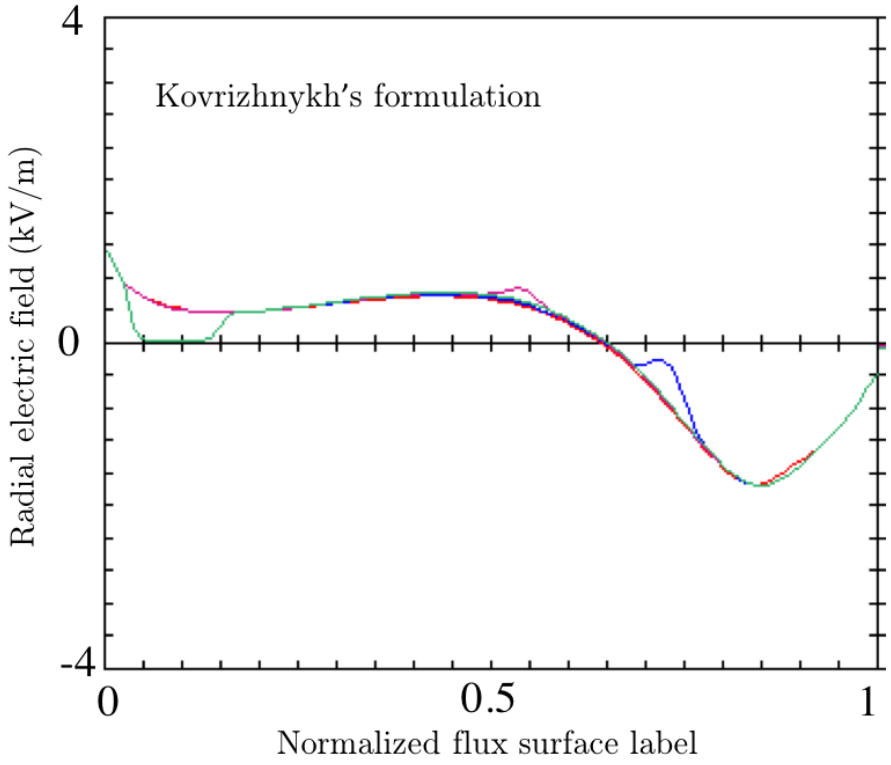

Figure 6.13: Electric field profiles obtained from Kovrizhnykh's model, together with Shaing's model is presented as a function of the normalized flux surface label. The smooth line represents the background of neoclassical transport, i.e., the profile generated only by Kovrizhnykh's model. The three 'bumps' are the results when Shaing's model is applied. In the inner locations, the electric field is positive with enhancement or decrease of the background electric field. In the outer region, however, the electric field is negative and it shows an enhancement of the background electric field.

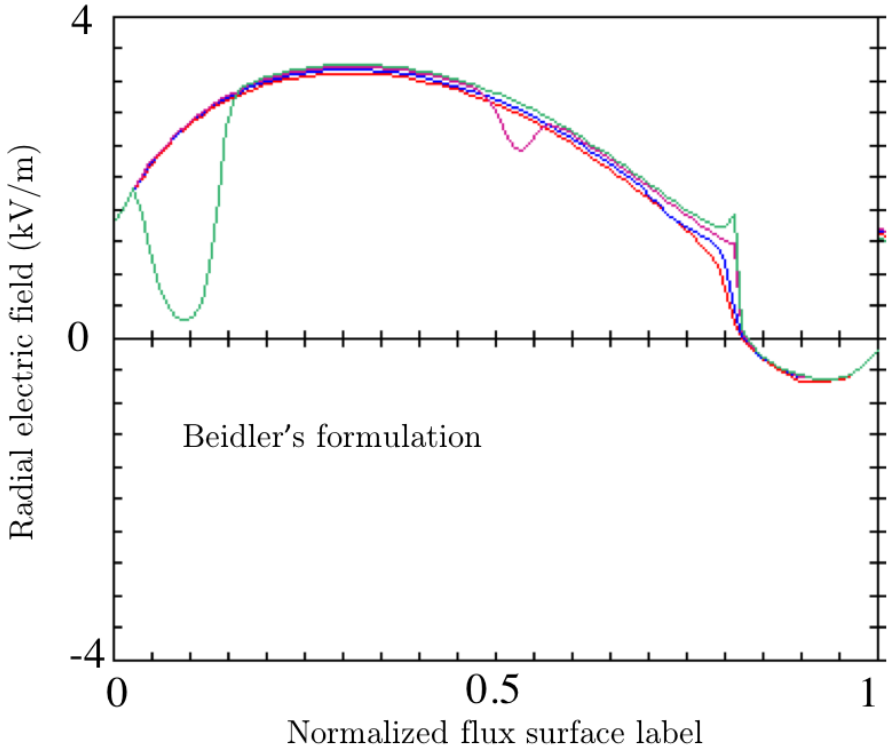

Figure 6.14: Electric field profiles obtained from Beidler's model, together with Shaing's model is presented as a function of the normalized flux surface label. The smooth line represents the background of neoclassical transport. The three 'bumps' are the results with Shaing's model. In this case all three resonant positions shows a positive electric contribution from Shaing's model and only the edge one shows an enhancement of the background electric field.

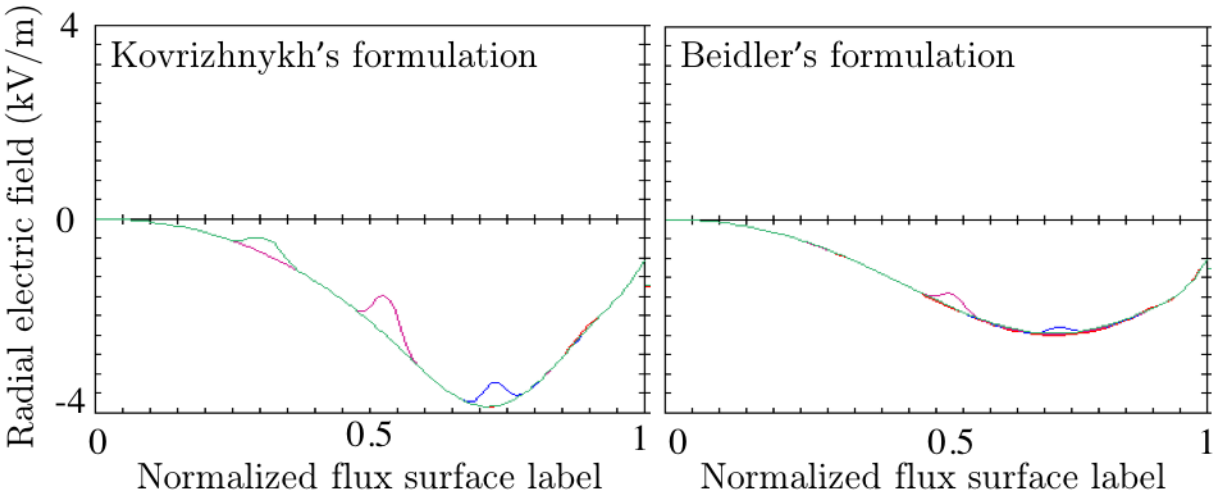

Figure 6.15: Two simulations performed with different neoclassical models together with Shaing's formula in NBI plasma obtained in TJ-II. The left graph is obtained using both Kovrizhnykh's model and Shaing's formula. The left one is obtained using both Beidler's model and Shaing's formula. The smooth line represents the background radial electric field and the 'bumps' are the extra contribution from Shaing's theory. Clearly, the background radial electric field profile is always negative and the contribution from Shaing's theory is always positive.

6.6 Summary

The magnetic islands in TJ-II stellarators have been reported to play a role of modifying the local radial electric field, which in turn, could play a role in L-H transition. The main principle of this phenomenon is that the existence of magnetic islands distorted the flux surfaces, which increases the plasma viscosity. It has been shown by Shaing that in tokamaks, for trapped particles, toroidal viscosity indeed plays a role of modifying the non-ambipolar neoclassical transport in vicinity of magnetic islands. Here we adopted his formulas in TJ-II plasmas to study the modification of radial electric field in vicinity of magnetic island.
From tokamaks to stellarators, there is a big difference and one need to adjust this transformation. One of the issue is that in stellarators, there is no toroidal symmetry so that usually the neoclassical transport is much higher than one in tokamaks. Hence, a factor of 1000 is applied to the flux function and this modification shows a reasonable result compared with the experimental data. Secondly, Shaing's formula

did not include super banana orbit. The validation of this assumption should be further checked in stellarators.

The preliminary study shows that the presence of magnetic island indeed modifies the radial electric field. In ECRH plasmas, the modification varies with the choice of 'background' neoclassical transport model, as well as the location of the magnetic islands. In NBI plasmas, however, the modification due to magnetic islands is always positive.

The formulas used here need to be studied and modified in the future in the sense that the factor $big = 1000$ we applied is just a rough assumption. Also the super banana effect, as mentioned above should be studied further. And finally, the interactions between Shaing's model and other neoclassical model is not simply $\Gamma = \Gamma^{background} + \Gamma^{island}$. The interactions between the two models should be further studied.

Part IV

Acknowledgement

Part V

Appendices

6.7 Ideal MHD

6.8 Flux Surface Average

The flux surface average of a function F is defined as follows:

$$\left\langle F \right\rangle_s = \frac{\int F d\theta d\psi \sqrt{g}}{\int d\theta d\psi \sqrt{g}} \tag{6.13}$$

If we consider the toroidal symmetry and substitute $\sqrt{g} = 1/(\mathbf{B} \cdot \nabla\theta)$we have:

$$\left\langle F \right\rangle_s = \frac{\int F d\theta / \mathbf{B} \cdot \nabla\theta}{\int d\theta / \mathbf{B} \cdot \nabla\theta} \tag{6.14}$$

The orbit average of a function F is defined as follows:

$$\left\langle F \right\rangle_o = \frac{\left\langle FB/|u| \right\rangle_s}{\left\langle B/|u| \right\rangle_s} = \frac{\int FBd\theta/(|u|\mathbf{B} \cdot \nabla\theta)}{\int Bd\theta/(|u|\mathbf{B} \cdot \nabla\theta)} = \frac{\int Fd\theta/(|u|\mathbf{n} \cdot \nabla\theta)}{\int d\theta/(|u|\mathbf{n} \cdot \nabla\theta)} \tag{6.15}$$

So if we take the orbit average in the form of $\left\langle u\nabla F \right\rangle_o$, we have:

$$\left\langle u\nabla F \right\rangle_o = \frac{\int n|u|\nabla F d\theta/(|u|\mathbf{n} \cdot \nabla\theta)}{\int d\theta/(|u|\mathbf{n} \cdot \nabla\theta)} = \frac{\int \mathbf{n} \cdot (\partial F/\partial\theta \nabla\theta) d\theta/(\mathbf{n} \cdot \nabla\theta)}{\int d\theta/(|u|\mathbf{n} \cdot \nabla\theta)} = \frac{\int d\theta \partial F/\partial\theta}{\int d\theta/(|u|\mathbf{n} \cdot \nabla\theta)} \tag{6.16}$$

The **bounce condition** is:

$$f_+(\theta = \pm\theta_b, \lambda, \omega) = f_-(\theta = \pm\theta_b, \lambda, \omega) \tag{6.17}$$

so the average is:

$$\left\langle u\nabla F \right\rangle_o = 0 \tag{6.18}$$

6.9 Magnetic Field Strength in Tokamaks

$$\nabla \times B = \mu_0 \left(J + \epsilon_0 \frac{\partial E}{\partial t} \right) \tag{6.19}$$

with $\partial E/\partial t \approx 0$, we have:

$$\oint_S B dl = \mu_0 J \tag{6.20}$$

which leads to

$$B = \frac{\mu_0 J}{2\pi r} \tag{6.21}$$

Here r is the distance from the toroidal center of the machine to the position which the calculation is performed.
For the magnetic field in the center of the plasma(geometry center), $r = R$, where R is the major radius, we have $B_0 = \mu_0 J/2\pi R$.
For any position r, here r is the poloidal local radius related to the magnetic axis, we have:

$$B = \frac{\mu_0 J}{2\pi \left|\vec{r} + \vec{R}\right|} \tag{6.22}$$

So we have:

$$\frac{B}{B_0} = \frac{r}{\left|\vec{r} + \vec{R}\right|} \tag{6.23}$$

where $\left|\vec{r} + \vec{R}\right| = \sqrt{(r^2 + R^2 + 2rR\cos\theta)}$. Define $\epsilon = r/R$ So we could get:

$$f(\epsilon) = \frac{1}{\sqrt{1 + \epsilon^2 + 2\epsilon\cos\theta}} \tag{6.24}$$

And one could perform Taylor expansion to the 1st order at $\epsilon = 0$:

$$\begin{aligned} f(\epsilon) = \sum_{n=0}^{\infty} \frac{f(0)^{(n)}}{n!}(\epsilon - 0)^n &= f(0) + f(0)' \cdot \epsilon \\ &= 1 - \left[\frac{1}{2}\left(\epsilon^2 + 1 + 2\epsilon\cos\theta\right)^{-3/2}\left(2\epsilon + 2\cos\theta\right)\right]_{\epsilon=0} \cdot \epsilon \\ &= 1 - \epsilon \cdot \cos\theta \end{aligned} \tag{6.25}$$

So the magnetic field strength $|\boldsymbol{B}| = B_0(1 - \epsilon\cos\theta)$

6.10 Non-Ambipolar FLux and Toroidal Viscosity

Moment Approach

In this part, Hamada coordinate [64] (V, θ, ζ) is adopted with V the volume enclosed inside the magnetic surfaces, θ the poloidal angle and ζ the toroidal angle. The

magnetic field can be represented as

$$\boldsymbol{B} = \psi' \nabla V \times \nabla\theta - \chi' \nabla V \times \nabla\zeta \tag{6.26}$$

Where χ is the poloidal flux and ψ is the toroidal flux. The prime denotes d/dV. The Jacobian is:

$$\sqrt{g} = (\nabla V \times \nabla\theta \cdot \nabla\zeta) = 1 \tag{6.27}$$

The particle flux is $\Gamma = n\mathbf{v}$ and its flux surface averaged in the direction of $\nabla\chi$ is:

$$\Gamma^{\chi} = \left\langle n\mathbf{v} \cdot \nabla\chi \right\rangle \tag{6.28}$$

The momentum equation is:

$$nm\frac{\partial \mathbf{v}}{\partial t} = ne\left(\mathbf{E} + \frac{1}{c}\mathbf{v} \times \mathbf{B}\right) - \nabla p - \nabla \cdot \overleftrightarrow{\pi} \tag{6.29}$$

Where $\overleftrightarrow{\pi}$ is the plasma viscosity. Taking the $\mathbf{B} \times \nabla\chi$ component of the steady-state momentum equation and using With $(\mathbf{B} \times \nabla\chi)/B^2 = (\mathbf{B}_t \cdot \mathbf{B})\,\mathbf{B}/B^2 - \mathbf{B}_t$, $\mathbf{E} \times \mathbf{B} \cdot \nabla\chi = \mathbf{E} \cdot \mathbf{B} \times \nabla\chi$ and $I_c = \mathbf{B}_t \cdot \mathbf{B}$:, we have:

$$\Gamma^{\chi} = \langle n\mathbf{v} \cdot \nabla\chi \rangle = \left\langle nc\frac{\mathbf{E} \times \mathbf{B} \cdot \nabla\chi}{B^2} \right\rangle + \left\langle \frac{c}{eB^2}\mathbf{B} \times \nabla\chi \cdot \left(\nabla p - \nabla \cdot \overleftrightarrow{\pi}\right) \right\rangle \tag{6.30}$$

Using a vector identity:

$$\mathbf{B}_t = \frac{(\mathbf{B}_t \cdot \mathbf{B})\,\mathbf{B}}{B^2} - \frac{\mathbf{B} \times \nabla\chi}{B^2} \tag{6.31}$$

We could obtain:

$$\begin{aligned}
\Gamma^{\chi} &= \left\langle nc\frac{\mathbf{EB} \cdot \nabla\chi}{B^2} \right\rangle + \left\langle \frac{c}{eB^2}\mathbf{B} \times \nabla\chi \cdot \left(\mathbf{F}_1 - \nabla p - \nabla \cdot \overleftrightarrow{\pi}\right) \right\rangle \\
&= \left\langle \mathbf{E} \cdot \left[\frac{\mathbf{B}_t \cdot \mathbf{B}}{B^2} - \mathbf{B}_t\right] \right\rangle + \left\langle \frac{c}{e}\left[\frac{(\mathbf{B}_t \cdot \mathbf{B})\,\mathbf{B}}{B^2} - \mathbf{B}_t\right] \cdot \left(\mathbf{F}_1 - \nabla p - \nabla\overleftrightarrow{\pi}\right) \right\rangle \\
= \left\langle nc\mathbf{E} \cdot \mathbf{B}\frac{I_c}{B^2} \right\rangle &- \langle nc\mathbf{E} \cdot \mathbf{B}_t \rangle + \frac{c}{e}\left\langle \frac{\mathbf{B} \cdot \mathbf{F}_1 I_c}{B^2} \right\rangle - \frac{c}{e}\left\langle \frac{\mathbf{B} \cdot \nabla p I_c}{B^2} \right\rangle - \frac{c}{e}\left\langle \frac{\mathbf{B} \cdot \nabla \cdot \overleftrightarrow{\pi} I_c}{B^2} \right\rangle \\
&- \frac{c}{e}\langle \mathbf{F}_1 \cdot \mathbf{B}_t \rangle + \frac{c}{e}\langle \mathbf{B}_t \cdot \nabla p \rangle + \frac{c}{e}\left\langle \mathbf{B}_t \cdot \nabla \cdot \overleftrightarrow{\pi} \right\rangle
\end{aligned} \tag{6.32}$$

The non-axisymmetric flux is

$$\Gamma^{NA} = \frac{e}{c}\left(\langle \mathbf{B}_t \cdot \nabla p\rangle + \left\langle \mathbf{B}_t \cdot \nabla \cdot \overleftrightarrow{\pi} \right\rangle\right) \tag{6.33}$$

In Hamada coordinates, $\langle \mathbf{B}_t \cdot \nabla p\rangle = 0$ for any non-axisymmetric torus and only $\left\langle \mathbf{B}_t \cdot \nabla \cdot \overleftrightarrow{\pi} \right\rangle$ contributes to non-axisymmetric partical flux Γ^{NA}.
The Pfirsch-Schluter flux

$$\Gamma^{PS} \tag{6.34}$$

The banana-plateau flux

$$\Gamma^{BP} = -\frac{c}{e}\left\langle \frac{\mathbf{B}\cdot\nabla\cdot\overleftrightarrow{\pi} I_c}{B^2} \right\rangle \tag{6.35}$$

The classical flux

$$\Gamma^{CL} \tag{6.36}$$

The residual $\mathbf{E}\times\mathbf{B}$ flux

$$\Gamma^{E} = nc\,\langle \mathbf{E}\cdot\mathbf{B}\rangle \frac{\langle I_c\rangle}{\langle B^2\rangle}\left(1 - \frac{\langle I_c\rangle}{\langle B^2\rangle}\frac{\langle B^2\rangle}{\langle I_c\rangle}\frac{V'}{4\pi^2 q}\right) \tag{6.37}$$

The flux associated with the moving velocity of the toroidal magnetic flux surface

$$\Gamma^{g} = nc\,\langle \mathbf{E}\cdot\mathbf{B}\rangle \left(\frac{V'}{4\pi^2 q} - \langle \mathbf{E}\cdot\mathbf{B}_t\rangle\right) \tag{6.38}$$

Note that the Γ^E, Γ^g are usually ignored and the Γ^{PS} is not in the banana regime. Also the Γ^{BP} is the parallel viscous force part and goes to zero after solving the bounced average of the kinetic equation.

Kinetic approach

The definition for the neoclassical particle flux is:

$$\Gamma^{\chi} = \left\langle \int d\mathbf{v} f \mathbf{v}_d \cdot \nabla\chi \right\rangle + \left\langle nc\frac{\mathbf{E}^{(A)}\times\mathbf{B}}{B^2} \right\rangle \tag{6.39}$$

with $\boldsymbol{v}_d = -v_\parallel \boldsymbol{b}\times\nabla(v_\parallel/\Omega)$ [65], the $\nabla\chi$ direction component is thus: $\mathbf{v}_d\cdot\nabla\chi = (v_\parallel/B)\nabla\cdot\left[\left((v_\parallel/\Omega)\right)\mathbf{B}\times\nabla\chi\right]$, we have:

$$\Gamma^{\chi} = \left\langle \int d\mathbf{v} f \mathbf{v}_\perp\cdot\nabla\chi \right\rangle = \left\langle \int d\mathbf{v} f \frac{v_\parallel}{B}\nabla\cdot\left[B^2\left(\frac{v_\parallel}{\Omega}\right)\left(\frac{\mathbf{B}\times\nabla\chi}{B^2}\right)\right] \right\rangle \tag{6.40}$$

Using a vector identity:

$$\mathbf{B}_t = \frac{(\mathbf{B}_t \cdot \mathbf{B})\,\mathbf{B}}{B^2} - \frac{\mathbf{B} \times \nabla\chi}{B^2} \tag{6.41}$$

$$\begin{aligned}\Gamma^{\chi} = &-\left\langle \int d\mathbf{v} f \left(\frac{v_\parallel}{B}\right) \nabla \cdot \left(\frac{v_\parallel B^2 \mathbf{B}_t}{\Omega}\right)\right\rangle + \left\langle \int d\mathbf{v} f \left(\frac{v_\parallel}{B}\right) \nabla \cdot \left[\left(\frac{v_\parallel B^2 \mathbf{B}_t}{\Omega}\right)\left(\frac{I_c}{B^2} - \frac{\langle I_c\rangle}{\langle B^2\rangle}\right)\right]\right\rangle \\ &+ \left\langle \int d\mathbf{v} f \left(\frac{v_\parallel}{B}\right) \nabla \cdot \left[\left(\frac{v_\parallel B^2 \mathbf{B}_t}{\Omega}\right)\frac{\langle I_c\rangle}{\langle B^2\rangle}\right]\right\rangle + \left\langle nc\frac{\mathbf{E}^{(A)} \times \mathbf{B}}{B^2}\right\rangle\end{aligned} \tag{6.42}$$

The non-axisymmetric flux Γ^{NA} is

$$\Gamma^{NA} = -\left\langle \int d\mathbf{v} f \left(\frac{v_\parallel}{B}\right) \nabla \cdot \left(\frac{v_\parallel B^2 \mathbf{B}_t}{\Omega}\right)\right\rangle \tag{6.43}$$

This is equivalent to Equation 6.33 from the momentum approach, which indicates the non-axisymmetric flux is due to the toroidal viscosity.

Part VI

References

Bibliography

[1] Joseph Donald Huba. Nrl: Plasma formulary. Technical report, DTIC Document, 2004.

[2] J Brian Taylor. Relaxation of toroidal plasma and generation of reverse magnetic fields. *Physical Review Letters*, 33(19):1139, 1974.

[3] DF Escande, R Paccagnella, S Cappello, C Marchetto, and F D'Angelo. Chaos healing by separatrix disappearance and quasisingle helicity states of the reversed field pinch. *Physical review letters*, 85(15):3169, 2000.

[4] Paolo Franz, Lionello Marrelli, Andrea Murari, Gianluca Spizzo, and Piero Martin. Soft x ray tomographic imaging in the rfx reversed field pinch. *Nuclear fusion*, 41(6):695, 2001.

[5] A Alfier and R Pasqualotto. New thomson scattering diagnostic on rfx-mod. *Review of scientific instruments*, 78(1):013505, 2007.

[6] P Innocente and S Martini. A two color multichord infrared interferometer for rfx. *Review of scientific instruments*, 63(10):4996–4998, 1992.

[7] P Innocente, S Martini, A Canton, and L Tasinato. Upgrade of the rfx co2 interferometer using in-vessel optics for extended edge resolution. *Review of scientific instruments*, 68(1):694–697, 1997.

[8] L Carraro, E Casarotto, R Pasqualotto, ME Puiatti, F Sattin, P Scarin, and M Valisa. Impurity influx studies in the rfx reversed field pinch. *Journal of nuclear materials*, 220:646–649, 1995.

[9] Andrea Murari, Paolo Franz, Luca Zabeo, Rosario Bartiromo, Lorella Carraro, Gianni Gadani, Lionello Marrelli, Piero Martin, Roberto Pasqualotto, and Marco Valisa. An optimized multifoil soft x-ray spectrometer for the determination of the electron temperature with high time resolution. *Review of scientific instruments*, 70(1):581–585, 1999.

[10] G Serianni, T Bolzonella, R Cavazzana, G Marchiori, N Pomaro, L Lotto, M Monari, and C Taliercio. Development, tests, and data acquisition of the integrated system of internal sensors for rfx. *Review of scientific instruments*, 75(10):4338–4340, 2004.

[11] E De la Luna, J Sánchez, V Tribaldos, and T Estrada. Multichannel electron cyclotron emission radiometry in tj-ii stellarator. *Review of Scientific Instruments*, 72(1):379–382, 2001.

[12] Horacio Lamela, Pablo Acedo, James Irby, et al. Laser interferometric experiments for the tj-ii stellarator electron-density measurements. *Review of Scientific Instruments*, 72(1):96–102, 2001.

[13] T Estrada, J Sánchez, B Van Milligen, L Cupido, A Silva, ME Manso, and V Zhuravlev. Density profile measurements by am reflectometry in tj-ii. *Plasma physics and controlled fusion*, 43(11):1535, 2001.

[14] L Cupido, J Sánchez, and T Estrada. Frequency hopping millimeter wave reflectometer. *Review of scientific instruments*, 75(10):3865–3867, 2004.

[15] T Happel, T Estrada, E Blanco, V Tribaldos, A Cappa, and A Bustos. Doppler reflectometer system in the stellarator tj-ii. *Review of Scientific Instruments*, 80(7):073502, 2009.

[16] IS Bondarenko, AA Chmuga, NB Dreval, SM Khrebtov, AD Komarov, AS Kozachok, LI Krupnik, P Coelho, M Cunha, B Gonçalves, et al. Installation of an advanced heavy ion beam diagnostic on the tj-ii stellarator. *Review of Scientific Instruments*, 72(1):583–585, 2001.

[17] MA Pedrosa, A López-Sánchez, C Hidalgo, A Montoro, A Gabriel, J Encabo, J De La Gama, LM Martınez, E Sánchez, R Pérez, et al. Fast movable remotely controlled langmuir probe system. *Review of scientific instruments*, 70(1):415–418, 1999.

[18] CJ Barth, FJ Pijper, HJ vd Meiden, J Herranz, and I Pastor. High-resolution multiposition thomson scattering for the tj-ii stellarator. *Review of scientific instruments*, 70(1):763–767, 1999.

[19] Thomas James Morrow Boyd and Jeffrey John Sanderson. *The physics of plasmas*. Cambridge University Press, 2003.

[20] AB Rechester and MN Rosenbluth. Electron heat transport in a tokamak with destroyed magnetic surfaces. *Physical Review Letters*, 40(1):38, 1978.

[21] Lyman Spitzer Jr. The stellarator concept. *Physics of Fluids (1958-1988)*, 1(4):253–264, 1958.

[22] P Sonato, G Chitarin, P Zaccaria, F Gnesotto, S Ortolani, A Buffa, M Bagatin, WR Baker, S Dal Bello, P Fiorentin, et al. Machine modification for active mhd co ntrol in rfx. *Fusion engineering and design*, 66:161–168, 2003.

[23] Carlos Alejaldre, Jose Javier Alonso Gozalo, Jose Botija Perez, Francisco Castejón Magaña, Jose Ramon Cepero Diaz, Jose Guasp Perez, A Lopez-Fraguas, Luis García, Vladimir I Krivenski, R Martin, et al. TJ-II project: a flexible heliac stellarator. *Fusion Science and Technology*, 17(1):131–139, 1990.

[24] KC Shaing, K Ida, and SA Sabbagh. Neoclassical plasma viscosity and transport processes in non-axisymmetric tori. *Nuclear Fusion*, 55(12):125001, 2015.

[25] D. López-Bruna, M.A. Ochando, A. López-Fraguas, F. Medina, and E. Ascasbar. Relationship between mhd events, magnetic resonances and transport barriers in TJ-II plasmas. *Nuclear Fusion*, 53(7):073051, 2013.

[26] D López-Bruna, M A Pedrosa, M A Ochando, T Estrada, B Ph van Milligen, A López-Fraguas, J A Romero, D Baio, F Medina, C Hidalgo, E Ascasbar, I Pastor, C Rodrguez, D Tafalla, and the TJ-II Team. Magnetic resonances and electric fields in the TJ-II heliac. *Plasma Physics and Controlled Fusion*, 53(12):124022, 2011.

[27] S Cappello and DF Escande. Bifurcation in viscoresistive mhd: The hartmann number and the reversed field pinch. *Physical review letters*, 85(18):3838, 2000.

[28] John M Finn, Rick Nebel, and Charles Bathke. Single and multiple helicity ohmic states in reversed-field pinches. *Physics of Fluids B: Plasma Physics (1989-1993)*, 4(5):1262–1279, 1992.

[29] P Martin, L Marrelli, G Spizzo, P Franz, P Piovesan, I Predebon, T Bolzonella, S Cappello, A Cravotta, DF Escande, et al. Overview of quasi-single helicity experiments in reversed field pinches. *Nuclear fusion*, 43(12):1855, 2003.

[30] DF Escande, P Martin, S Ortolani, A Buffa, P Franz, L Marrelli, E Martines, G Spizzo, S Cappello, A Murari, et al. Quasi-single-helicity reversed-field-pinch plasmas. *Physical review letters*, 85(8):1662, 2000.

[31] Rita Lorenzini, E Martines, P Piovesan, D Terranova, P Zanca, M Zuin, A Alfier, D Bonfiglio, F Bonomo, A Canton, et al. Self-organized helical equilibria as a new paradigm for ohmically heated fusion plasmas. *Nature Physics*, 5(8):570–574, 2009.

[32] R Lorenzini, M Agostini, A Alfier, V Antoni, L Apolloni, F Auriemma, O Barana, M Baruzzo, P Bettini, D Bonfiglio, et al. Improvement of the magnetic configuration in the reversed field pinch through successive bifurcationsa). *Physics of Plasmas (1994-present)*, 16(5):056109, 2009.

[33] Emilio Martines, Rita Lorenzini, Barbara Momo, David Terranova, Paolo Zanca, Alberto Alfier, Federica Bonomo, Alessandra Canton, Alessandro Fassina, Paolo Franz, et al. Equilibrium reconstruction for single helical axis reversed field pinch plasmas. *Plasma Physics and Controlled Fusion*, 53(3):035015, 2011.

[34] R Lorenzini, A Alfier, F Auriemma, A Fassina, P Franz, P Innocente, D López-Bruna, E Martines, B Momo, G Pereverzev, et al. On the energy transport in internal transport barriers of rfp plasmas. *Nuclear Fusion*, 52(6):062004, 2012.

[35] Gregorij V Pereverzev and PN Yushmanov. Astra. automated system for transport analysis in a tokamak. 2002.

[36] P Franz, M Gobbin, L Marrelli, A Ruzzon, F Bonomo, A Fassina, E Martines, and G Spizzo. Experimental investigation of electron temperature dynamics of helical states in the rfx-mod reversed field pinch. *Nuclear Fusion*, 53(5):053011, 2013.

[37] R. Lorenzini, F. Auriemma, A. Fassina, E. Martines, D. Terranova, and F. Sattin. Internal transport barrier broadening through subdominant mode stabilization in reversed field pinch plasmas. *Phys. Rev. Lett.*, 116:185002, May 2016.

[38] F Auriemma, R Lorenzini, M Agostini, L Carraro, G De Masi, A Fassina, M Gobbin, E Martines, P Innocente, P Scarin, et al. Characterization of particle confinement properties in rfx-mod at a high plasma current. *Nuclear Fusion*, 55(4):043010, 2015.

[39] D Terranova, F Auriemma, A Canton, L Carraro, R Lorenzini, and P Innocente. Experimental particle transport studies by pellet injection in helical equilibria. *Nuclear Fusion*, 50(3):035006, 2010.

[40] R Fitzpatrick. Interaction of tearing modes with external structures in cylindrical geometry (plasma). *Nuclear Fusion*, 33(7):1049, 1993.

[41] AJ Cole, CC Hegna, and JD Callen. Neoclassical toroidal viscosity and error-field penetration in tokamaksa). *Physics of Plasmas (1994-present)*, 15(5):056102, 2008.

[42] HP Furth and MN Rosenbluth. Low-frequency plasma loss mechanisms in mhd-stabilized toruses. In *Plasma Physics and Controlled Nuclear Fusion Research. Proceedings of the Third International Conference on Plasma Physics and Controlled Nuclear Fusion Research. Vol. I*, 1969.

[43] A. A. Galeev, R. Z. Sagdeev, H. P. Furth, and M. N. Rosenbluth. Plasma diffusion in a toroidal stellarator. *Phys. Rev. Lett.*, 22:511–514, Mar 1969.

[44] Ker-Chung Shaing. Symmetry-breaking induced transport in the vicinity of a magnetic island. *Physical review letters*, 87(24):245003, 2001.

[45] E Joffrin, CD Challis, GD Conway, X Garbet, A Gude, NC Hawkes, TC Hender, DF Howell, GTA Huysmans, E Lazzaro, et al. Internal transport barrier triggering by rational magnetic flux surfaces in tokamaks. *Nuclear fusion*, 43(10):1167, 2003.

[46] ME Austin, KH Burrell, RE Waltz, KW Gentle, P Gohil, CM Greenfield, RJ Groebner, WW Heidbrink, Y Luo, JE Kinsey, et al. Core barrier formation near integer q surfaces in diii-da). *Physics of Plasmas (1994-present)*, 13(8):082502, 2006.

[47] T Estrada, L Krupnik, N Dreval, A Melnikov, SM Khrebtov, C Hidalgo, B van Milligen, F Castejón, E Ascasíbar, L Eliseev, et al. Electron internal transport barrier formation and dynamics in the plasma core of the TJ-II stellarator. *Plasma physics and controlled fusion*, 46(1):277, 2003.

[48] F Castejón, D López-Bruna, T Estrada, E Ascasíbar, B Zurro, and A Baciero. Influence of low-order rational magnetic surfaces on heat transport in tj-ii heliac ecrh plasmas. *Nuclear Fusion*, 44(5):593, 2004.

[49] M Hirsch, J Baldzuhn, C Beidler, R Brakel, R Burhenn, A Dinklage, H Ehmler, M Endler, V Erckmann, Y Feng, et al. Major results from the stellarator wendelstein 7-as. *Plasma Physics and Controlled Fusion*, 50(5):053001, 2008.

[50] F Sano, T Mizuuchi, K Kondo, K Nagasaki, H Okada, S Kobayashi, K Hanatani, Y Nakamura, S Yamamoto, Y Torii, et al. H-mode confinement of heliotron j. *Nuclear fusion*, 45(12):1557, 2005.

[51] T Estrada, T Happel, L Eliseev, E Blanco, L Cupido, JM Fontdecaba, C Hidalgo, L Krupnik, M Liniers, ME Manso, et al. Sheared flows and transition to improved confinement regime in the tj-ii stellarator. *Plasma Physics and Controlled Fusion*, 51(12):124015, 2009.

[52] T Estrada, C Hidalgo, T Happel, and PH Diamond. Spatiotemporal structure of the interaction between turbulence and flows at the lh transition in a toroidal plasma. *Physical review letters*, 107(24):245004, 2011.

[53] K Ida, N Ohyabu, T Morisaki, Y Nagayama, S Inagaki, K Itoh, Y Liang, K Narihara, A Yu Kostrioukov, BJ Peterson, et al. Observation of plasma flow at the magnetic island in the large helical device. *Physical review letters*, 88(1):015002, 2001.

[54] C Hidalgo, MA Pedrosa, E Sánchez, R Balbín, A López-Fraguas, B Van Milligen, C Silva, H Fernandes, CAF Varandas, C Riccardi, et al. Generation of sheared poloidal flows via reynolds stress and transport barrier physics. *Plasma Physics and Controlled Fusion*, 42(5A):A153, 2000.

[55] L Garcia, BA Carreras, VE Lynch, MA Pedrosa, and C Hidalgo. Sheared flow amplification by vacuum magnetic islands in stellarator plasmas. *Physics of Plasmas (1994-present)*, 8(9):4111–4119, 2001.

[56] HE Mynick. Transport optimization in stellaratorsa). *Physics of Plasmas (1994-present)*, 13(5):058102, 2006.

[57] Kenro Miyamoto. Plasma physics for nuclear fusion. *Cambridge, Mass., MIT Press, 1980. 625 p. Translation*, 1980.

[58] K. C. Shaing. Radial electric field and plasma confinement in the vicinity of a magnetic island. *Physics of Plasmas*, 9(8):3470–3475, 2002.

[59] K. C. Shaing, M. S. Chu, C. T. Hsu, S. A. Sabbagh, Jae Chun Seol, and Y. Sun. Theory for island induced neoclassical toroidal plasma viscosity in tokamaks. *Nuclear Fusion*, 51(12):124033, 2011.

[60] V. Tribaldos. Monte Carlo estimation of neoclassical transport for the TJ-II stellarator. *Physics of Plasmas*, 8(4):1229–1239, 2001.

[61] DE Hastings, WA Houlberg, and Ker-Chung Shaing. The ambipolar electric field in stellarators. *Nuclear Fusion*, 25(4):445, 1985.

[62] LM Kovrizhnykh. Modeling of transport processes in stellarators. *Plasma Physics Reports*, 32(12):988–995, 2006.

[63] CD Beidler. Neoclassical transport properties of hsr. *IPP-Report*, 2(331):194, 1996.

[64] Shigeo Hamada. Hydromagnetic equilibria and their proper coordinates. *Nuclear Fusion*, 2(1-2):23, 1962.

[65] FL Hinton and RD Hazeltine. Theory of plasma transport in toroidal confinement systems. *Reviews of Modern Physics*, 48(2):239, 1976.

List of Figures